

FINAL REPORT

Advanced UXO Detection and Discrimination Using Magnetic
Data Based on Extended Euler Deconvolution and Shape
Identification Through Multipole Moments

SERDP Project MR-1638

APRIL 2011

Richard Krahenbuhl
Yaoguo Li
Misac Nabighian
Kris Davis
Center of Gravity, Electrical & Magnetic Studies
Department of Geophysics
Colorado School of Mines

Steve Billings
Sky Research, Inc

This document has been cleared for public release



Report Documentation Page			Form Approved OMB No. 0704-0188					
<p>Public reporting burden for the collection of information is estimated to average 1 hour per response, including the time for reviewing instructions, searching existing data sources, gathering and maintaining the data needed, and completing and reviewing the collection of information. Send comments regarding this burden estimate or any other aspect of this collection of information, including suggestions for reducing this burden, to Washington Headquarters Services, Directorate for Information Operations and Reports, 1215 Jefferson Davis Highway, Suite 1204, Arlington VA 22202-4302. Respondents should be aware that notwithstanding any other provision of law, no person shall be subject to a penalty for failing to comply with a collection of information if it does not display a currently valid OMB control number.</p>								
1. REPORT DATE APR 2011	2. REPORT TYPE N/A	3. DATES COVERED -						
4. TITLE AND SUBTITLE Advanced UXO Detection and Discrimination Using Magnetic Data Based on Extended Euler Deconvolution and Shape Identification Through Multipole Moments			5a. CONTRACT NUMBER					
			5b. GRANT NUMBER					
			5c. PROGRAM ELEMENT NUMBER					
6. AUTHOR(S)			5d. PROJECT NUMBER					
			5e. TASK NUMBER					
			5f. WORK UNIT NUMBER					
7. PERFORMING ORGANIZATION NAME(S) AND ADDRESS(ES) Center of Gravity, Electrical & Magnetic Studies Department of Geophysics Colorado School of Mines			8. PERFORMING ORGANIZATION REPORT NUMBER					
9. SPONSORING/MONITORING AGENCY NAME(S) AND ADDRESS(ES)			10. SPONSOR/MONITOR'S ACRONYM(S)					
			11. SPONSOR/MONITOR'S REPORT NUMBER(S)					
12. DISTRIBUTION/AVAILABILITY STATEMENT Approved for public release, distribution unlimited								
13. SUPPLEMENTARY NOTES The original document contains color images.								
14. ABSTRACT								
15. SUBJECT TERMS								
16. SECURITY CLASSIFICATION OF: <table border="1" style="width: 100%; border-collapse: collapse;"> <tr> <td style="padding: 2px;">a. REPORT unclassified</td> <td style="padding: 2px;">b. ABSTRACT unclassified</td> <td style="padding: 2px;">c. THIS PAGE unclassified</td> </tr> </table>			a. REPORT unclassified	b. ABSTRACT unclassified	c. THIS PAGE unclassified	17. LIMITATION OF ABSTRACT SAR	18. NUMBER OF PAGES 117	19a. NAME OF RESPONSIBLE PERSON
a. REPORT unclassified	b. ABSTRACT unclassified	c. THIS PAGE unclassified						

Executive Summary

This is the final report for SERDP project MR-1638 and it covers the research results accomplished throughout the project's life. The basic premise of the project is the development of a comprehensive approach for detecting UXO-like targets in the presence of geologic noise, and discrimination between UXO and non-UXO through indirect shape information contained within the magnetic higher-order moments.

The first principal task of the project was the continued development and testing of a new method for UXO anomaly detection using a Hilbert transform-based extended Euler deconvolution. During initial development of the algorithm through SERDP project MM-1414, positive results in magnetic environments demonstrated the feasibility of the technique when pre-processing is applied to the field data to manage the geologic response. Current developments through MR-1638 include modification of the algorithm to include higher-quality magnetic gradient data, and development of a post-processing statistical technique for reducing the number of false picks associated with high-frequency noise and geologic interference. This phase of research has confirmed our belief that the thresholding of targets selected as potential UXO by extended Euler deconvolution needs to move beyond the limited information contained in the phase. Secondary processing of identified target anomalies have demonstrated that amplitude information is an essential component for successfully reducing many of the false anomalies associated with geologic noise.

The second major task of this project focused on the difficulty of discriminating UXO from non-UXO items with real data when sensor data are strongly contaminated with geological and cultural noise. Successful detection of UXO in these magnetic environments requires detecting all dipole-like magnetic anomalies and identifying and discarding the geologic anomalies that drastically increase the number of false targets. This component of the project therefore had a major emphasis on developing or modifying robust processing algorithms, not common to UXO remediation efforts, for

separating strong magnetic interference and enhancing the response of desired targets. The results for these techniques applied to Camp Sibert and San Luis Obispo magnetic data demonstrated that we can significantly improve data quality and enhance UXO/scrap targets at sites exhibiting strong magnetic interference from soils, geology, underground-structures (bunkers), and sensor noise.

The final major project task takes discrimination between UXO and non-UXO beyond the current dipole-based approaches by utilizing the higher order magnetic moments that encode shape information about buried targets. Throughout this project, we have developed several robust inversion algorithms tailored to the complex nature of the solution space and applied the techniques to both realistic synthetic scrap/UXO models, as well as highest quality data from real targets. Results have indicated that recovery of higher-order magnetic moments containing target shape information is theoretically possible with appropriate inversion algorithms and high-quality data. However, these parameters are likely unrecoverable from real data over UXO/scrap targets, even with high-quality dense data, for practical discrimination based on the total-field magnetic response.

Table of Contents

1. Introduction	7
1.1. Background	7
1.2. Research approach	7
1.3. Summary of Accomplishment	9
2. Automatic Anomaly Detection Using Extended Euler Deconvolution	12
2.1. Background	12
2.2. Introduction	12
2.3. Theory and Algorithm	13
2.3.1. Extended Euler Deconvolution	13
2.3.2. Automatic Anomaly Detection	15
2.3.3. Numerical Procedure	17
2.4. Synthetic Example	18
2.5. Summary	21
3. Effects of Low-Pass Filtering on Structural Index	23
3.1. Background	23
3.2. Introduction	23
3.3. Theory and Algorithm	24
3.4. Numerical Example	27
3.5. Summary	30
4. Extending Euler Detection Algorithm to Gradient Data	31
4.1. Introduction	31
4.2. Background	31
4.3. Synthetic Example	32
4.4. Summary	36
5. Reducing False Detections due to Data Noise and Magnetic Geology	37
5.1. Introduction	37
5.2. Identifying and removing false detections using amplitude analysis	40
5.4. Field Examples	44

5.4.1. Camp Sibert	44
5.4.2. Montana	48
5.5. An alternative approach to the choice of amplitude threshold.....	52
5.6. Summary.....	54
6. Separation of Strongly Interfering Geology	56
6.1. Introduction.....	56
6.2. Separation of interfering geology, enhancing UXO response.....	58
6.2.1. Iterative Wiener	58
6.2.2. Wavelet Transform	63
6.2.3. Linear Feature Analysis & Removal.....	66
6.2.4. Regional/Residual Separation, with Total Gradient enhancement	69
6.2.4.1. Camp Sibert, AL	71
6.2.4.2. San Luis Obispo, CA	72
6.3. Summary.....	76
7. Application of automated SI detection.....	78
7.1. Background	78
7.2. Introduction.....	78
7.3. Detection results.....	79
7.3.1. Camp Sibert, AL	79
7.3.2. San Luis Obispo, CA	82
7.4. Summary.....	85
8. Recovery of multipole magnetic moments for discrimination.....	86
8.1. Background	86
8.2. Introduction.....	86
8.3. Multipole magnetic moments.....	87
8.4. Inversion for multipole moments	89
8.4.1. Model parameters.....	90
8.4.2. Developed inversion algorithms	92
8.5. Results for Simulated UXO / Scrap.....	94
8.6. Results for Real UXO / Scrap	96
8.6.1. Data Collection Platforms.....	97

8.6.2. Static Measurements	101
8.5.3. Dynamic Measurements.....	103
8.6.4. Inversion/Discrimination Results from Real Magnetic Data.....	105
8.7. Summary.....	109
9. Discussion.....	111
9.1. Automated Anomaly Detection by Extended Euler Deconvolution	111
9.2. Separation of Interfering Geology, Enhancing UXO Response	111
9.3. Recovering higher-order moments for magnetic discrimination	112
10. Acknowledgements	114
11. References.....	115

1. Introduction

1.1. Background

SERDP Project MM-1638 sought to address one of the Department of Defense's (DoD) most pressing environmental problems; that is, the efficient and reliable identification of unexploded ordnance (UXO) without the need to excavate large numbers of non-UXO. The task of discriminating UXO from non-UXO items is more difficult when sensor data are contaminated with geological and routine acquisition noise. In regions of strong magnetic geology, for example, magnetic sensors detect anomalies that are geologic, as well as metallic, in origin. Successful detection of UXO in these environments requires detecting all dipole-like magnetic anomalies and identifying and discarding geologic anomalies, as well as targets resulting from high frequency acquisition errors during field activities. Beyond detection, the next level of difficulty lies in the ability to discriminate between UXO and non-UXO items of similar genesis, such as scrap metal. This project also sought to develop a technique that moves beyond the current dipole-based approaches by utilizing the higher-order magnetic moments that encode direct shape information about buried targets. For magnetic methods to advance to the level of TEM for practical discrimination of UXO/scrap based on shape, recovery of the higher-order magnetic moments from the data would be required.

1.2. Research approach

SERD Project MM-1414 demonstrated promising results in identifying target location and depth estimation of magnetic dipoles using a Hilbert transform-based extended Euler deconvolution for UXO detection. The basic method estimates horizontal location, depth, and more importantly, the general configuration of the magnetic source that produces the total-field anomaly. The difficulty of the approach, as with most detection tools, is that the performance of extended Euler deconvolution is dependant on the signal-

to-noise ratio. This is because the basis for the method is calculating the decay rate of the observed field, and if significant noise is present, the results will degrade. To improve the method, the current project aimed to further improve the Euler deconvolution based method and develop an integrated detection approach by incorporating a set of pre-processing procedures to account for and remove magnetic anomalies associated with geologic structures – a common sources of false positives in both standard and extended Euler methods – and a post-processing procedure to further identify additional compact anomalies of geologic origin or associated with acquisition noise.

In addition to further developing an advanced detection method for dipole-like anomalies (i.e., potential UXO targets), this project likewise sought to develop a new generation of magnetic discrimination methodologies by moving beyond the current dipole-based approach and utilizing the quadrupole, which describe the asymmetry properties of the magnetization distribution within buried metallic objects. While the dipole moment summarizes the total intensity of the magnetization within an object, it carries no direct shape information. This lack of information about size, orientation, and asymmetry of the body has hampered a more successful discrimination effort by magnetic method. As a result, current dipole-based discrimination methods (Billings, 2004) rely upon the direction of magnetization that might be altered by physical processes such as shock demagnetization and remanent magnetization. Up until this project, there had been little work in the literature that makes direct use of the geometry of buried metallic objects. Part of the reason for this state of affairs is the belief that only the dipole moment can be recovered from field data, whereas the discrimination based on shape, similar to TEM method, requires higher-order moments for magnetics. The acquisition of high-quality data and development of robust inversions through this collaborative project could therefore make it feasible to recover higher-order moments, and raise the possibility of their use for shape reconstruction as a means for UXO discrimination.

Traditionally, detection and discrimination approaches are developed with the goal of limiting the respective targets to only hazardous unexploded ordnance. Rather than

following such an approach, SERDP project MR-1638 sought to develop a comprehensive method to:

- 1st: Separate and enhance the response of potential UXO and scrap items from any magnetic dataset, regardless of the level of background/geologic interference.
- 2nd: Automatically identify all potential UXO-like targets in the presence of geologic anomalies and acquisition noise that greatly increase the number of false targets.
- 3rd: Directly distinguish between UXO and non-UXO by defining the asymmetry properties of these potential targets through higher-order moments.

In this Final Report for SERDP Project MR-1638, we present results accomplished throughout the project that focus on these practical issues, including the latest development in data processing/filtering, detection, and discrimination for magnetics.

1.3. Summary of Accomplishment

The research throughout this project progressed satisfactorily and we have accomplished the major tasks outlined in the project execution plan. The first major achievement was completing the further development of the automatic anomaly detection algorithm based on extended Euler deconvolution, which consists of the basic algorithm, pre-processing method, expansion to gradient data, and post-processing amplitude analysis for reducing false detections.

The second major achievement was creating an initial suite of powerful processing algorithms uncommon to UXO remediation efforts. These algorithms have been partly modified from developments in the exploration community, such as mining and petroleum applications, and adapted for the UXO magnetic problem. We have made significant strides into separating the response of difficult interfering geology while preserving the response of potential UXO/scrap in difficult datasets such as San Luis

Obispo. There are several subsequent methodologies in use by the UXO community for detecting potential UXO in magnetic data – the most common being through Geosoft – and all of these techniques (regardless of preference) can benefit from the developments of MR-1638 for pre-processing difficult magnetic datasets.

The final major accomplishment was the development of a series of robust optimization algorithms designed to invert for the multi-pole magnetic moments over UXO and scrap. The goal was to recover the higher-order moments in realistic 3D modeling simulations and high-quality field data. Within the suite of minimization algorithms for this problem, we have identified a recursive implementation of Quenched Simulated Annealing (QSA) performs well at recovering these parameters. From these valuable magnetic moments, we can then calculate a measure of target asymmetry. The method has performed well on simulated UXO and scrap, and we have therefore identified a working technique to measure shape differences between UXO and scrap based on magnetic multipole moments. The difficulty of the method in practice, however, lies in moving beyond theory and into recovery of multipole moments from real data. We have applied the developments to high-quality densely spaced real data over various UXO and scrap targets. Results indicate that even the most robust inversion technologies may not be able to recover the higher-order magnetic moments for practical discrimination based on magnetics.

This annual report is organized to present these research results by chapter in the following order.

Chapter 2 of this report provides the necessary background information on developments to our automated anomaly detection algorithm which utilizes the Hilbert transform based extended Euler deconvolution. Chapter 3 presents developments over the past year into understanding the effects of pre-processing algorithms on recovered structural index values in relation to SI-based detection algorithms. Chapter 4 describes the expansion of the detection algorithm to magnetic gradient data, and demonstrates the potential improvement in detection results through numerical simulations. In Chapter 5, we

develop a complementary set of processing procedures, such as amplitude analysis applied directly to extended Euler detection results, and it is observed to significantly reduce the number of false targets associated with geologic responses and data noise. Chapter 6 brings together a collection of robust pre-processing algorithms for removing the response of interfering magnetic background to enhance the response of compact targets such as UXO and scrap. The algorithms are not industry standard techniques, and we apply them to difficult magnetic data collected from South-West Camp Sibert and San Luis Obispo sites. In Chapter 7, we demonstrate application of developed filtering algorithms, in combination with extended Euler deconvolution automated detection method to field data sets, thus moving this component of the project from simulation to practical application. In Chapter 8, we present our research, developments and applications of discrimination based on recovery of multi-pole magnetic moments.

2. Automatic Anomaly Detection Using Extended Euler Deconvolution

2.1. Background

Two main goals of the SERDP project MM-1638 were to apply the automated approach for UXO detection based on the extended Euler deconvolution to environments with strong magnetic geology, and to complete the development of necessary pre- and post-processing steps for recognizing false alarm due to geology. The concept of the method for detecting compact dipole-like sources was presented by Davis *et al.* (2005) and in SERDP MM-1414 (2007). The technique demonstrated significant promise. That project also demonstrated the need for a set of practical pre- and post-processing procedures to manage the response of magnetic geology and acquisition noise, which either generated numerous false UXO targets or masked the true UXO entirely.

In this chapter, we first provide the requisite background information on extended Euler deconvolution. This technique is the backbone of the method for detecting potential UXO targets in magnetic environments based on the dipole response of these compact metallic sources. We likewise present an updated set of procedures for automating the technique for practical application to UXO remediation problems, and illustrate them with examples. In later chapters, we extend the automated detection approach to magnetic gradient data and illustrate complementary processing procedures developed to reduce the number of false anomalies associated with geologic and acquisition noise.

2.2. Introduction

Magnetometry has emerged as one of the most efficient and cost-effective methods for detecting and discriminating unexploded ordnance (UXO) targets. Recent work by Billings *et al.* (2002) has demonstrated that low false-alarm rates and a high degree of

detection can be achieved through the inversion of static magnetic data. Successful application to large areas of such inversion-based discrimination algorithms depends on the ability to automatically detect targets by picking the anomalies that are caused by UXO-like objects. The commonly used method for anomaly picking has predominantly been the thresholding of total gradient data (often mistakenly referred to as the 3D analytical signal). This method has drawbacks because of the interfering effects of background geology and other noise in data sets. A different approach was proposed by Billings and Herrmann (2003), based on a continuous wavelet transform using natural wavelets.

We have developed an alternative method for automatic anomaly detection using the Hilbert transform-based extended Euler deconvolution technique (Nabighian and Hansen, 2001). The method estimates both location and, more importantly, the type of magnetic source that produced the anomaly. Any anomaly whose source appears to be dipolar is considered a potential UXO target based on the assumption that the majority of UXO act as magnetic dipoles. In this chapter, we first describe extended Euler deconvolution and then explain the methodology of how we use it as a tool for automatic anomaly detection. After giving the numerical procedure, we illustrate our method using a synthetic dataset.

2.3. Theory and Algorithm

2.3.1. Extended Euler Deconvolution

Euler deconvolution was originally developed in exploration geophysics to rapidly estimate the location and depth to magnetic or gravity sources. It is based on the fact that the potential field produced by many simple sources obeys Euler's homogeneity equation. If a given component of the magnetic anomalous field $\Delta T(x, y, z)$ satisfies:

$$\Delta T(tx, ty, tz) = t^n \Delta T(x, y, z) \quad (2.1)$$

where n is the degree of homogeneity, then by differentiating Eq. (2.1) with respect to t it can be shown that

$$x \frac{\partial \Delta T}{\partial x} + y \frac{\partial \Delta T}{\partial y} + z \frac{\partial \Delta T}{\partial z} = n \Delta T \quad (2.2)$$

where x , y and z are the field coordinates and the source is assumed to be at the origin. Equation (2.2) is known as Euler's homogeneity equation (Hood, 1965) or simply Euler's equation. The degree of homogeneity is source dependent and characterizes how fast the field decreases as a function of distance to the source. For example, the total-field anomaly produced by a dipolar source decreases as inverse distance cubed and the corresponding degree of homogeneity is $n = -3$; a cylinder has $n = -2$, and a dike has $n = -1$. The same holds true for gradient anomalies, with the degree of homogeneity for a dipolar source as $n = -4$; a cylinder, $n = -3$; and a dike, $n = -2$.

Equation (2.2) can be used to estimate the source depth from magnetic data in 3D, which gives rise to the method of Euler deconvolution (e.g. Reid *et al.*, 1990). Since the potential field decreases inversely proportional to the distance raised to some power, the degree of homogeneity is non-positive. The negative of the degree of homogeneity is defined as the structural index (SI) and will be denoted as N . Assuming that the field due to a compact source located at (x_o, y_o, z_o) is superimposed on a background field, we rewrite Eq. (2.2) as:

$$\sum_{x_i}^{x,y,z} (x_i - x_{oi}) \frac{\partial \Delta T}{\partial x_i} = -N \Delta T + \alpha \quad (2.3)$$

where x_i represents the three orthogonal directions x , y , and z , and α represents a constant background value which is strongly coupled with the structural index. Equation (2.3) contains five unknowns: x_o , y_o , z_o , α , and N . Due to the strong coupling between the variables α and N , it is customary to assume an *a priori* value for N and solve for the

remaining four unknowns. The x , y , and z derivatives can be calculated using various algorithms depending on the distribution of original data. Applying Eq. (2.3) to a number of neighboring data points, we obtain a system of equations that can be solved in a least squares sense for the source location (x_o, y_o, z_o) and the background level α . The algorithm is usually applied to points within a window of a specified size. The *a priori* choice of structural index has been the topic of much discussion in the literature since it is somewhat arbitrary and the obtained solutions depend strongly on its choice.

Recently, Nabighian and Hansen (2001) extended the work by Mushayandebvu *et al.* (1999) and showed that the same Euler equation also holds true for the two components of the 3D Hilbert transforms of the field:

$$\begin{aligned} \sum_{x_i}^{x,y,z} (x_i - x_{oi}) \frac{\partial H_x[\Delta T]}{\partial x_i} &= -NH_x[\Delta T] \\ \sum_{x_i}^{x,y,z} (x_i - x_{oi}) \frac{\partial H_y[\Delta T]}{\partial x_i} &= -NH_y[\Delta T] \end{aligned} \quad (2.4)$$

where $H_x[\Delta T]$ and $H_y[\Delta T]$ denote respectively the x - and y -component of the 3D Hilbert transform (Nabighian, 1984) applied to the field, ΔT . In contrast with Eq. (2.3), Eq. (2.4) does not require a background term since the Hilbert transform of a constant is equal to zero. The absence of a background term allows now for the direct evaluation of the structural index N , and this leads to a more stable and versatile method of depth estimation and source location. Thus we have an effective means to estimate not only the source location and depth but also its structural index.

2.3.2. Automatic Anomaly Detection

The ability to estimate the structural index, rather than specifying it in advance, means that we can distinguish between different source types during the depth estimation process. This enables us to identify UXO responses among the interfering anomalies of

geologic origin. The majority of UXO items are predominantly dipolar sources. The corresponding total-field magnetic anomaly ΔT is given by

$$\Delta T(\mathbf{r}) = \frac{\mu_o}{4\pi} \mathbf{m} \cdot \nabla \nabla \frac{1}{|\mathbf{r}_o - \mathbf{r}|} \cdot \hat{\mathbf{B}}_o \quad (2.5)$$

where \mathbf{m} is the dipole moment, $\hat{\mathbf{B}}_o$ is a unit vector along the direction of ambient magnetic field, and \mathbf{r}_o and \mathbf{r} are respectively the location of the dipole and observation point. It follows that the structural index of a dipolar field is 3.

The majority of geologic features tend to have some elongation and their magnetic anomalies would have a structural index less than that of a dipolar feature. Based on this observation, we have developed a method for automatically picking UXO anomalies using calculated structural indices. The central premise of the proposed method is that any compact source identified by extended Euler deconvolution as having a structural index close to 3 for total-field, or 4 for gradient data, can be considered a potential UXO target and merits further investigation.

Equation (2.4) is applied throughout the entire data set within sliding windows. Each window yields a valid solution if there is a significant magnetic anomaly within that window. The reliability of a solution is often affected by the choice of window size, since a small window may not capture the anomaly pattern necessary for the calculation, and too large a window may introduce interference from adjacent anomalies. In general, one would use a larger window size for deeper sources and a smaller window size for shallower sources. For our application, we have chosen to use multiple window sizes to allow for the variable depths and sizes of UXO targets in an area.

The method first performs a sequence of Hilbert transform-based Euler deconvolution using different window sizes on the data set and obtains estimates of source locations and structural indices. It then examines the variation of structural index with window size and identifies the Euler solutions that yield structural index values close to the target

structural index. Any anomalies with a structural index close to the specified target structural index, within a user specified tolerance, would indicate a potential UXO target. Specifying a tolerance is necessary because of the influence on the calculated structural index by noise in the data and by all previous processing steps. The threshold should be above 2 for total-field data and above 3 for gradient data. The ideal structural index from a cylinder would be at these values and thus anything above it could be a potential dipole anomaly. The noise in a data set can corrupt the signal that the extended Euler deconvolution searches for and thus the accuracies of locations, depths, and structural index will decrease with the noise level. As these values will be affected by the noise in the data set, only cleaner data will be close to the theoretical structure index values. The results will in general be more accurate for gradient data as the noise level is often significantly lower than in total-field data.

2.3.3. Numerical Procedure

Assuming a gridded magnetic data set ΔT , the detection method begins by computing the two horizontal derivatives, $\frac{\partial \Delta T}{\partial x}$ and $\frac{\partial \Delta T}{\partial y}$, using stabilized numerical differentiation based on least-squares fitting of a parabola over five data points (Lanczos, 1988). The vertical derivative $\frac{\partial \Delta T}{\partial z}$ is then computed in the Fourier domain through the use of 3D Hilbert transform relations (Nabighian, 1984):

$$\Delta \tilde{T}_z = \tilde{H}_x \Delta \tilde{T}_x + \tilde{H}_y \Delta \tilde{T}_y \quad (2.7)$$

$$= -\frac{i\omega_x}{\sqrt{\omega_x^2 + \omega_y^2}} \Delta \tilde{T}_x - \frac{i\omega_y}{\sqrt{\omega_x^2 + \omega_y^2}} \Delta \tilde{T}_y \quad (2.8)$$

where ω_x and ω_y are the respective wavenumbers of 2D Fourier transform in the x - and y -direction and $\Delta \tilde{T}_x$, $\Delta \tilde{T}_y$, $\Delta \tilde{T}_z$ are the respective Fourier transforms of the x -, y - and z -derivatives of the magnetic anomaly. The two components of 3D Hilbert transform of the

original magnetic anomaly and its three spatial derivatives allow us to obtain the eight quantities related to the magnetic anomaly required in Eq. (2.4). The derivatives of each Hilbert transform component in Eq. (2.4) are then obtained by applying Hilbert transform to each corresponding derivative of the original anomaly.

Using the eight previously calculated quantities, Eq. (2.4) can now be solved in each window using least squares. As mentioned previously, a range of different window sizes is used. This step yields both the source location estimates (x_o , y_o , z_o) and the structural index N for that source. From the set of windows centered at the same location, we find the one solution whose structural index N is closest to 3 for total-field data or 4 for gradient data. This solution is taken as the best solution associated with the set of windows centered at a common point. If a solution exists and the structural index is greater than a threshold value, we assume that the algorithm has detected a possible UXO-like anomaly. The corresponding location provides a first order estimate for the dipole position. Performing this procedure on a data set produces a map of detected anomalies and their source locations. The horizontal locations can be used subsequently to help extract individual anomalies for determining source parameters through dipole inversion or other discrimination techniques.

2.4. Synthetic Example

To illustrate the method, we apply it to a synthetic data set. The synthetic data were generated from 20 dipoles with random locations, orientations, depths, and dipole moments (Figure 2.1). The depths range from 0.3 m to 0.8 m, with dipole inclinations ranging between -90° and 90° , declination between -180° and 180° , and dipole moments varying between 0.1 and 0.5 Am². The ambient magnetic field is assumed to have an inclination of 65° and declination of 25° . These 20 dipole sources were used to produce the total-field anomaly. Although the example is simplistic and has no noise component, it is an excellent example to illustrate the theoretical aspects of the detection algorithm.

We first apply our detection algorithm to the total-field anomaly over 12 window sizes varying between 3 to 25 grid points in each direction. Corresponding to each magnetic anomaly, a large number of Euler solutions were generated from windows that capture a reasonable part of the anomaly. The solutions in such a group differ only slightly from each other. Assuming all solutions within 0.5 m radius come from the same target, we clustered the solutions after thresholding the structural index for the entire data set and obtained 20 distinct detected anomalies. All detected anomalies have structural index values greater than 2.5. Of these 20 solutions, 19 coincide with true anomalies in the data set, while one is located between two adjacent anomalies. Thus, we have correctly detected 19 out of 20 anomalies, missed one anomaly, and have produced a single false alarm. The result is shown in Figure (2.1) where we post the detection result over the contours of the magnetic anomaly. We also compare the x - y locations and depths from the Euler solutions with the true values in Figure (2.2). The maximum difference in the x - y plane was 12 cm radially. The maximum difference between the true and calculated depths was 4 cm. The results have yielded a first order approximation to dipole locations in three dimensions.

We note that the missed anomaly in this example was a weak positive anomaly juxtaposed between a weak and strong negative anomaly. This seemed to have confused the detection algorithm because the interference by the two adjacent anomalies caused the calculated decay rate to be much smaller. The false anomaly occurred between two closely spaced anomalies. This solution was produced from a large window size, causing the algorithm to have difficulties recognizing the presence of two neighboring anomalies since the Euler solution assumes only one source per window. Larger window sizes are still necessary, however, to observe larger anomalies.

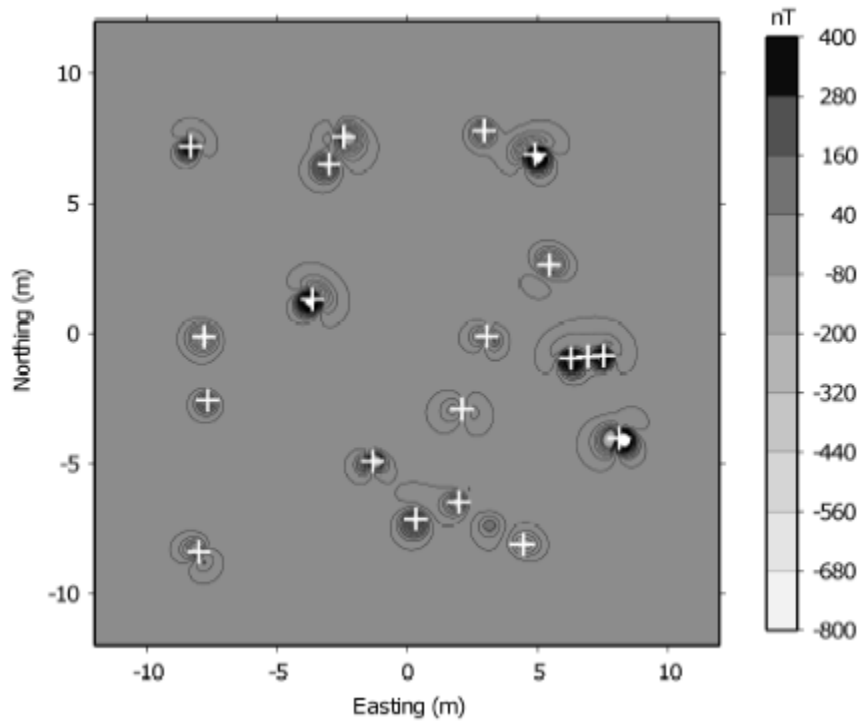


Figure 2.1: The total-field response for 20 randomly oriented dipoles. The + indicates where extended Euler deconvolution picked potential UXO anomalies. One detection was a false positive and the algorithm missed one dipole feature.

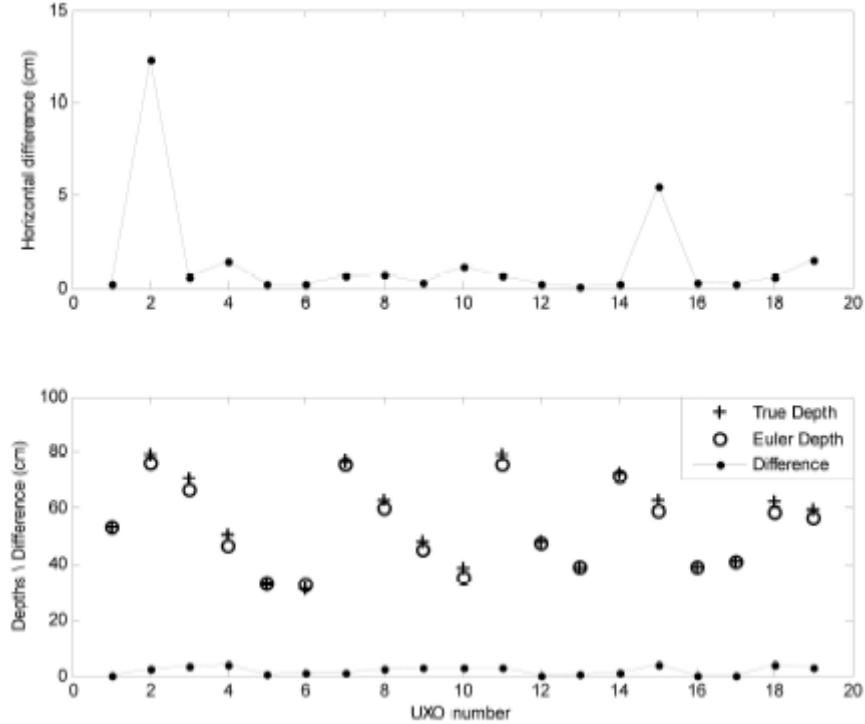


Figure 2.2: Comparison between true and estimated dipole locations. The upper panel shows the horizontal distance between the true and predicted dipoles. The lower panel shows the true and predicted depths and the difference between the two. The vertical axes in both panels are in units of cm. Only the solutions that corresponded to true targets were used in the comparison.

2.5. Summary

In this chapter, we presented the basic algorithm developed for automatically detecting UXO anomalies by utilizing extended Euler deconvolution based on 3D Hilbert transforms. The central premises of the algorithm are twofold. First, extended Euler deconvolution of magnetic data can yield a reliable estimate of an anomaly's structural index and location; and secondly, any magnetic anomaly whose structural index is close to that of a dipole (i.e., 3 for total-field data and 4 for gradient data) is a compact source and constitutes a possible UXO anomaly requiring further analysis. We have successfully demonstrated the algorithm's performance using synthetic total-field data without noise. Results have shown that the majority of buried UXO targets can be detected.

The first component of the algorithm performs extended Euler deconvolutions with a range of window sizes and solves for the source location and structural index. All results above the user-specified threshold of the structural index are collected as viable solutions for UXO detection. It is important that the user select a threshold to capture all the dipole features within the data set. In general, several solutions will be present around each dipole feature, so they are clustered into a mean solution within a given radius. It is noteworthy that this step assumes a single magnetic anomaly within each window. Thus, multiple UXO targets within the window area will adversely affect calculations.

The estimated horizontal and vertical locations of the detected anomalies in the synthetic examples agree well with the true locations. The estimated dipole locations, therefore, provide a good first estimate for subsequent quantitative analyses. For example, these locations can then be used as an initial guess of the dipole location in an inversion for discrimination.

It is important to note that our algorithm is not a discrimination technique, but rather a tool for automatically choosing potential UXO anomalies based on the assumption that a UXO anomaly has a dipolar shape. The anomalies require further investigation after detection.

Based on the theoretical argument, we expect the detection algorithm to work with any type of magnetic data as long as we can characterize the decay rate in the form of the structural index (SI). We investigate this aspect in the next chapters while still maintaining the idealized scenario of accurate data. Following that, we will examine the performance of method in the presence of geologic and data acquisition noise and develop effective strategies to recognize false detections produced by such noise.

3. Effects of Low-Pass Filtering on Structural Index

3.1. Background

The concept of the method for detecting compact dipole-like sources was presented by Davis *et al.* (2005), extended throughout this project, and presented in the previous chapter. We demonstrated that the completed methodology has significant promise as an automated first-round detection tool for identifying dipole-type sources for later discrimination algorithms. In this chapter we present theoretical understanding and a numerical example to address the question of how filtering magnetic data collected for UXO application affects the SI, which extended Euler method recovers (along with position) as a means of identifying dipole sources.

3.2. Introduction

Potential-field data used in final interpretation are often a smoothed version of the true field. For example, measured data can undergo several steps of processing that are equivalent implicitly to a low-pass filtering. Oftentimes, for very noisy data, some interpreters explicitly use a low pass filter to clean the data before applying various techniques (e.g. extended Euler deconvolution) to determine location, depth and structural index (SI) for the various targets in the area of interest. There is an ongoing discussion in the potential- field community about the effect of low-pass filtering on the structural index values for various targets. In this project, we show that low-pass filtering will decrease the determined SI to a value lower than the one predicted theoretically. The result has direct implications to the application of Euler deconvolution in depth, including the choice of SI for standard Euler method and the interpretation of SI estimated from extended Euler deconvolution.

3.3. Theory and Algorithm

Oftentimes, for very noisy data, some researchers use a low pass filter to clean the data before applying various techniques (e.g. extended Euler deconvolution) to determine location, depth and structural index (SI) for the various targets in the area of interest. There is an ongoing dispute in the UXO community about the effect of low pass filtering on the determination of the structural index values for various targets. In this short note we show that the effect of low-pass filtering will decrease the determined SI to a value lower than the one predicted theoretically. To this end we use the analytic expression for the potential of a vertical magnetic dipole which has a known structural index value equal to 2. After applying a bell-shaped low pass filter to this data in frequency domain we evaluate the Euler equation directly over the source. We then show that the determined SI will decrease proportional with the increased degree of low-pass filtering applied to the data.

For simplicity, we begin with the potential of a vertical magnetic dipole, which has an SI of 2 prior to filtering. We assume observation locations on the x - y plane at $z = 0$ and a vertical magnetic dipole source located at $(0,0,z)$. The magnetic potential, V , is given by

$$V = \frac{\mu_0}{4\pi} m_z \frac{z}{(x^2 + y^2 + z^2)^{3/2}}, \quad (3.1)$$

where m_z is the vertical component of the magnetic dipole moment. We examine a low-pass filter based on the radial wavenumber in the Fourier domain. The 2D Fourier transform of equation (3.1), \tilde{V} , can easily be derived as:

$$\tilde{V} = \frac{\mu_0}{8\pi^2} m_z e^{-\left(z\sqrt{\omega_x^2 + \omega_y^2}\right)}, \quad (3.2)$$

where ω_x and ω_y are wavenumbers in the x - and y -directions, respectively (Blakely, 1996). We apply a simple low-pass filter with the transfer function, F_l :

$$F_l = \frac{1}{1 + \omega_r \alpha} , \quad (3.3)$$

where $\omega_r = \sqrt{\omega_x^2 + \omega_y^2}$ is the radial wavenumber and the constant α controls the cutoff wavenumber of the filter. A greater α means a lower cutoff wavenumber. The corresponding low-pass filtered field is given by the following inverse Fourier transform,

$$V_l = \frac{\mu_o}{8\pi^2} m_z \int \int_{-\infty}^{\infty} e^{-z\omega_r} e^{i(x\omega_x + y\omega_y)} \frac{1}{1 + \omega_r \alpha} d\omega_x d\omega_y . \quad (3.4)$$

This integral is even in ω_x and ω_y , so it can be rewritten as

$$V_l = \frac{\mu_o}{2\pi^2} m_z \int \int_0^{\infty} \frac{e^{-z\omega_r}}{1 + \omega_r \alpha} \cos(x\omega_x) \cos(y\omega_y) d\omega_x d\omega_y . \quad (3.5)$$

In order to be able to carry out the above integration, we use Laplace's transform to obtain

$$\frac{1}{1 + \omega_r \alpha} = \int_0^{\infty} e^{-t(1 + \alpha\omega_r)} dt . \quad (3.6)$$

Substituting equation 3.6 in equation 3.5, we obtain:

$$V_l = \frac{\mu_o}{2\pi^2} m_z \int_0^{\infty} e^{-t} dt \int \int_0^{\infty} e^{-z\omega_r} e^{-\alpha\omega_r} \cos(x\omega_x) \cos(y\omega_y) d\omega_x d\omega_y , \quad (3.7)$$

which can now be evaluated. We first evaluate the integral with respect to ω_x by using the identity 3.914 in Gradshteyn and Ryzhik (1965) to obtain

$$\int_0^\infty e^{(-z+\alpha t)\omega_x} \cos(x\omega_x) d\omega_x = \frac{\omega_y(z+\alpha t)}{\sqrt{x^2 + (z+\alpha t)^2}} K_1\left[\omega_y \sqrt{x^2(z+\alpha t)^2}\right]. \quad (3.8)$$

With Eq. 3.8, then Eq 3.7 becomes

$$V_l = \frac{2}{\pi} m_z \int_0^\infty e^{-t} \frac{z+\alpha t}{\sqrt{x^2 + (z+\alpha t)^2}} dt \int_0^\infty \omega_y \cos(y\omega_y) K_1\left[\omega_y \sqrt{x^2(z+\alpha t)^2}\right] d\omega_y. \quad (3.9)$$

Using the identity 6.699 from Gradshteyn and Ryzhik (1965), the integral above with respect to ω_y can be evaluated as

$$\frac{\pi}{2} \frac{\sqrt{x^2 + (z+\alpha t)^2}}{(x^2 + y^2 + (z+\alpha t)^2)^{3/2}}. \quad (3.10)$$

The final solution for a low-pass filtered potential of a vertical magnetic dipole becomes

$$V_l = \frac{\mu_o}{4\pi} m_z \int_0^\infty e^{-t} \frac{z+\alpha t}{[x^2 + y^2 + (z+\alpha t)^2]^{3/2}} dt. \quad (3.11)$$

It is important to note that when $\alpha = 0$ (no filter applied), the above equation reduces to the original potential in equation 3.1.

Next we examine the structural index of equation 3.11 at the optimal location, i.e. directly above the dipole at the origin, given by

$$V_l(0,0,0) = \frac{\mu_o}{4\pi} m_z \int_0^\infty \frac{e^{-t} dt}{(z+\alpha t)^2}. \quad (3.12)$$

At the origin, $x = 0$, $y = 0$, $\partial V_l / \partial x = \partial V_l / \partial y = 0$ and the standard Euler equation simplifies to

$$z \frac{\partial V_l}{\partial z} = NV_l , \quad (3.13)$$

Which can be evaluated to finally obtain

$$N = 2z \frac{\int_0^\infty \frac{e^{-t} dt}{\left(1 + \alpha \frac{t}{z}\right)^3}}{\int_0^\infty \frac{e^{-t} dt}{\left(1 + \alpha \frac{t}{z}\right)^2}} , \quad (3.14)$$

and since

$$1 + \alpha \frac{t}{z} \geq 1 , \quad (3.15)$$

the numerator will always be smaller or equal to the denominator for any value of α . Hence, $N \leq 2$ for any value of α and, furthermore, the greater α is, the smaller N becomes.

3.4. Numerical Example

For a demonstration, we apply the standard Euler equation as well as extended Euler deconvolution to the low-pass filtered potential in expression 3.11. The dipole is at a depth of 0.5 m with corresponding filter lengths being $\alpha = 0, 1, 5, 20$, and 100. The shape of the low-pass filter for these various values of α is shown in Figure 3.1(a). Profiles of the corresponding analytic solution of SI are shown in 3.1(b). The SI located directly above the source decreases as α increases. The SI values towards the edges of the anomaly map can be greater than 2. These values begin at 2.5 m away from the source in each direction, which is a distance of five times the depth to the source. The Euler solutions in these regions are usually discarded in practice by the commonly used

requirement that the valid solutions be within certain distance from the center of the data window (Silva and Barbosa, 2003). We also observe that the curves shift to lower SI values as more of the anomaly is filtered out.

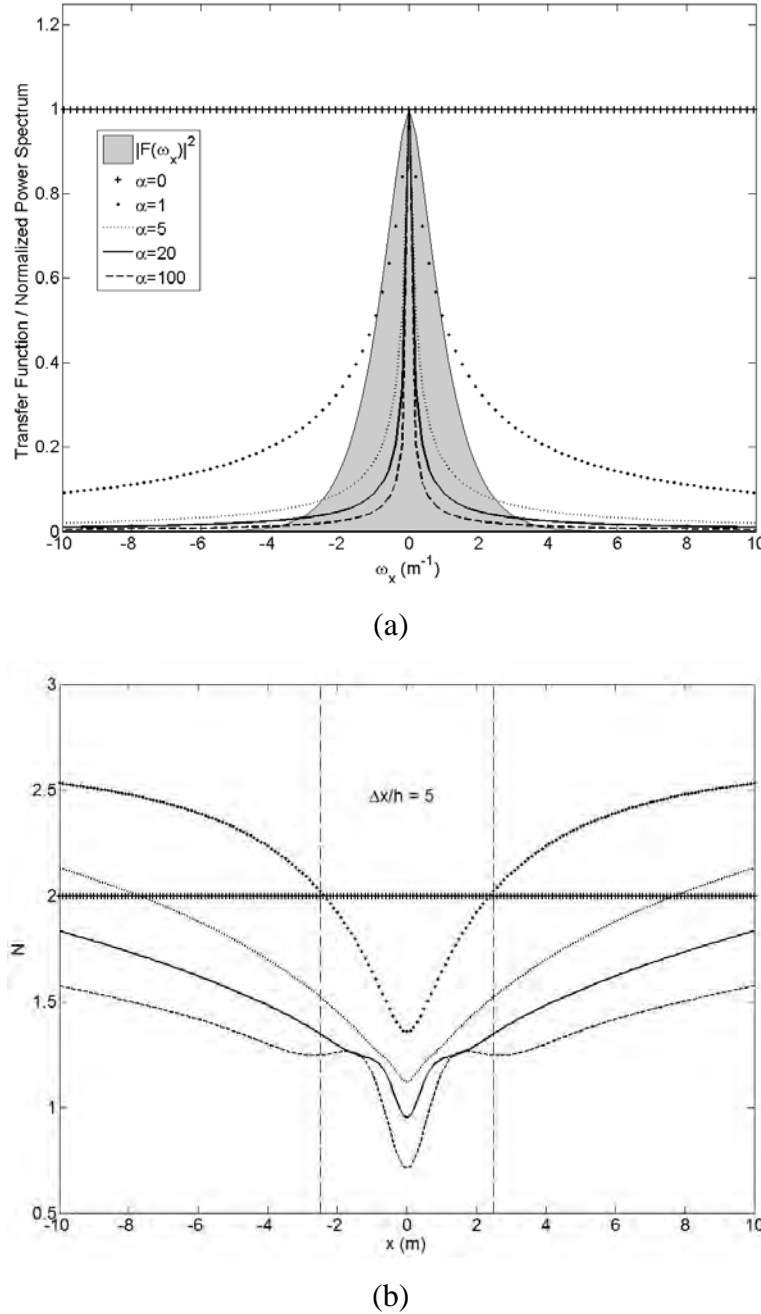


Figure 3.1: Profiles of the transfer functions used (a) and their respective profiles of structural indexes (b). As the low-pass filters increase, the structural index N decreases and is below the optimal SI above the source location.

We then perform extended Euler deconvolution numerically on the filtered data as well. The analytic solution was calculated at 0.1 m gridded increment along the x - y plane at $z=0$. The curve that shows the structural index of the anomaly based on filter lengths is displayed in Figure 3.2 for $\alpha = 0, 1, \dots, 39, 40$. The depth increases as a function of low-pass filtering as one would expect due to the decrease in higher frequency content. Though the SI does not decrease monotonically, it does not increase to or above the expected SI of an unfiltered field.

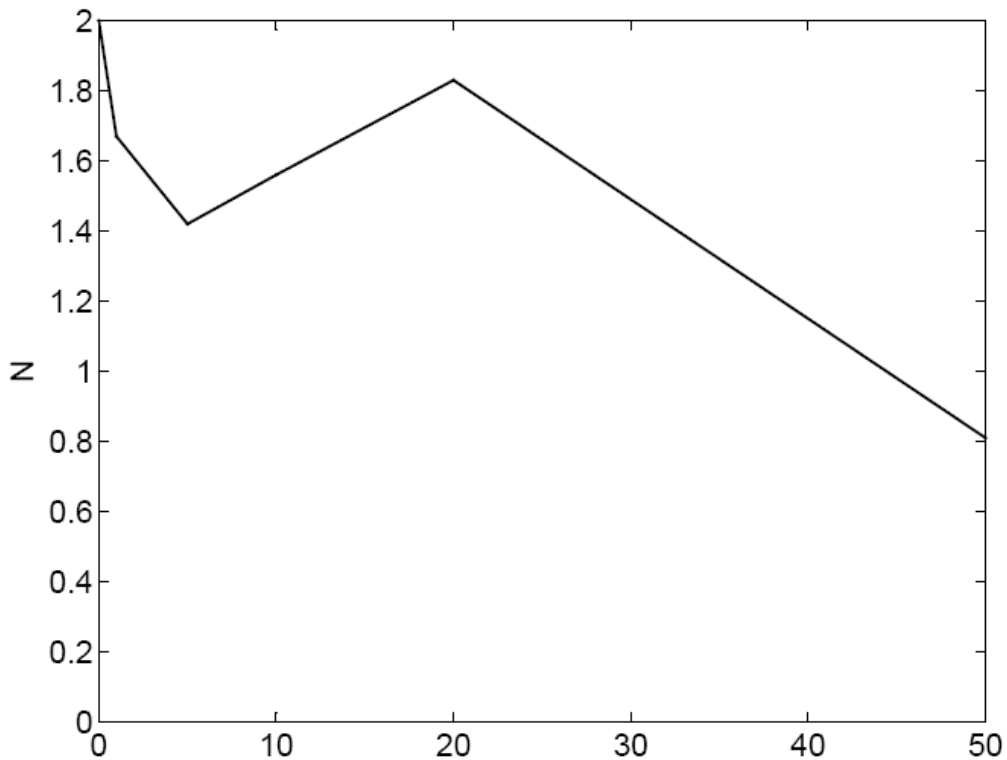


Figure 3.2: The corresponding SI solved numerically with extended Euler deconvolution versus α . Though the SI does not decrease monotonically, the overall trend is decreasing and only the non-filtered data reaches $N = 2.0$.

3.5. Summary

We note that the above evaluation pertains to a general low-pass filter. Upward continuation is often used as a low-pass filter and it deserves a special discussion in this context. This is a special filter since it preserves physics and therefore a dipolar field remains dipolar after upward continuation and its SI does not change. However, for a source distributed within a finite region in the subsurface, as is the case in UXO applications, its field can be expressed as a multipole expansion. Any low pass filter will preferentially attenuate the effect of higher-order multipoles and lead to a decreased SI towards the SI of the lower order multipole. Thus we can conclude that applying a low-pass filter to data will decrease the SI for valid Euler and extended Euler solutions.

4. Extending Euler Detection Algorithm to Gradient Data

4.1. Introduction

The early component of MR-1638 focused on detection of UXO in magnetic environments, and as such, we discuss here the modifications to the algorithms presented in the preceding chapters for the incorporation of magnetic gradient data. With this extension to gradient data, we developed a thorough understanding as part of this project. Results indicated that gradient data may prove more reliable for detecting UXO-like sources while reducing false positives.

4.2. Background

In theory, any of the methods developed throughout this project can be modified to work with total-field as well as gradient magnetic data. This includes both the automated extended Euler deconvolution which seeks the dipolar response of UXO, and the discrimination techniques later on which seek to reveal the shape information contained within the higher-order moments. The benefits of using gradient data are higher signal-to-noise ratio that can lead to a more accurate estimation of structural index for the first, and improved likelihood of recovering the requisite higher order moments for the latter.

We now turn our attention to automated detection of UXO through extended Euler deconvolution in magnetic gradient data. The extended Euler deconvolution outlined in Chapter 2 estimates horizontal location, depth, and more importantly, the type of the magnetic source – geology versus anthropogenic based on the decay of the observed response – that produces the magnetic anomaly. The magnetic field produced by a dipole-like source, such as UXO and other buried metallic objects, varies with inverse

distance cubed, and therefore has a structural index (SI) of 3. Any anomaly whose source appears to be dipolar with SI of 3 is therefore considered a potential UXO target based on the assumption that the majority of UXO and small metallic objects act primarily as magnetic dipoles.

The same theory we developed for total-field magnetic data extends directly to magnetic gradient data. For the gradient of the total field $\frac{\partial \Delta T}{\partial x_i}$, in the x_i direction, the dipolar anomaly is given by

$$\frac{\partial \Delta T}{\partial x_i}(\mathbf{r}) = \frac{\mu_o}{4\pi} \mathbf{m} \cdot \nabla \nabla \frac{[x_i(\mathbf{r}_o) - x_i(\mathbf{r})]}{|\mathbf{r}_o - \mathbf{r}|^2} \cdot \hat{\mathbf{B}}_o \quad (4.1)$$

where \mathbf{m} , $\hat{\mathbf{B}}_o$, \mathbf{r}_o , and \mathbf{r} are same as in Eq (2.5). The extra derivative introduced in Eq (4.1) implies that the structural index of the gradient of a dipolar field is 4. While we developed our detection technique using total field magnetic data ΔT in the preceding chapter, to work with gradient data $\frac{\partial \Delta T}{\partial x_i}$, we can simply exchange ΔT with $\frac{\partial \Delta T}{\partial x_i}$ in eq.(2.4), and change the corresponding SI to 4.

4.3. Synthetic Example

We now turn to the gradient of the synthetic data from the previous chapter to examine how the results would differ between total-field and gradient response of buried UXO. The vertical gradient of the same data set is used and extended Euler deconvolution applied (Figure 4.1). The data are simulated on a regular grid with an interval of 0.1 m in both easting and northing direction. The two magnetic sensors measuring the vertical gradient of assumed be separated by 0.4 m. The data are then gridded to a uniform grid of 0.1 m. The results of performing Euler detection are similar to those from the total-field anomaly. Euler deconvolution successfully detected 19 targets and no false positives. The

one missed anomaly is the same weak anomaly that was juxtaposed between two strong anomalies. In contrast to the results from total-field data, the false anomaly is no longer present. This is primarily due to the increased higher wavenumber content in the gradient data, which manifests as the sharper anomalies.

Figure 4.2 shows the comparison between true anomaly source parameters with those estimated during the automated detection using extended Euler deconvolution. These results are comparable with the result from total-field data. The error in the estimated depths is on the same level, but the error in the horizontal positions of the detected anomalies are slightly lower. This similarity in performance is expected since we are using accurate data with good spatial coverage.

The same results were also achieved with the horizontal gradient (Figure 4.3). We have simulated the horizontal gradient in north-south direction on the same data grid with 0.1 m interval in both horizontal directions. The baseline between the two sensors is 0.2 m. Using an SI threshold of 3.5, the automated algorithm detected 19 targets. There were no false positives and the only target missed was the same target as missed by the total-field data with a weak magnetic positive between weak and strong magnetic negatives. The errors in the estimated source locations (Figure 4.4) are slightly greater than that from the vertical gradient data.

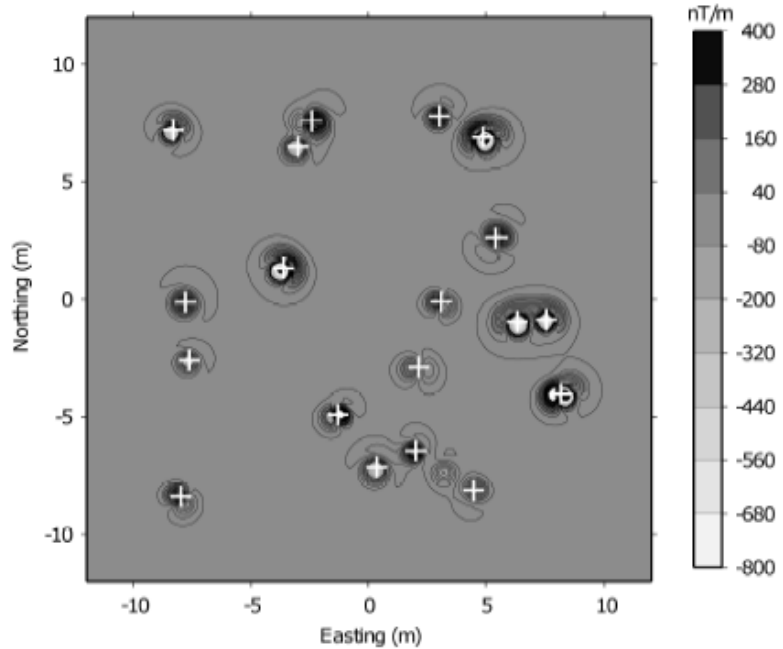


Figure 4.1: The vertical gradient response of the same 20 randomly oriented dipoles as in Figure 2.1. The + indicates picked potential UXO anomalies. The extended Euler deconvolution correctly picked 19 anomalies and missed one.

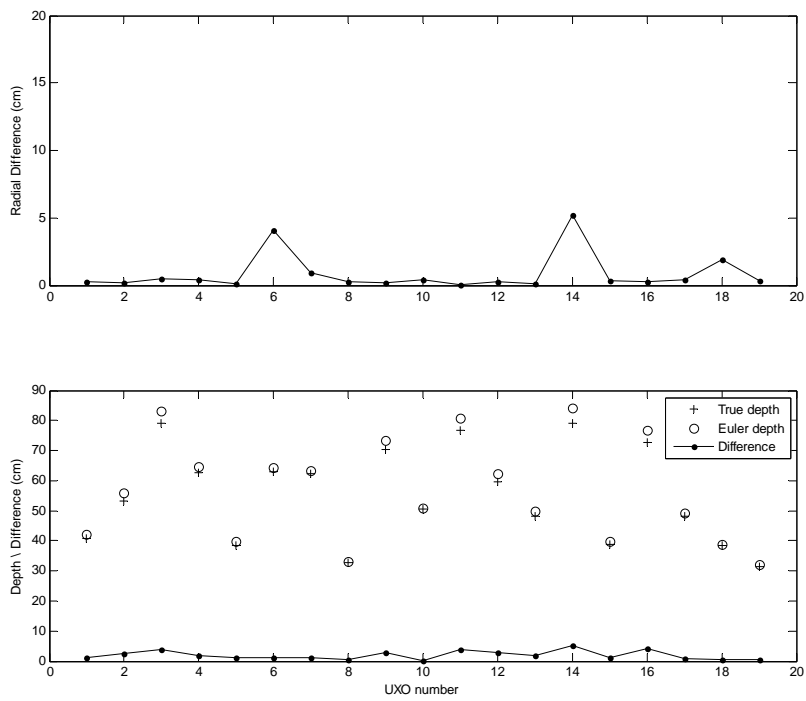


Figure 4.2: Comparison of true anomaly source parameters with those estimated during the automated detection using extended Euler deconvolution on the vertical gradient data.

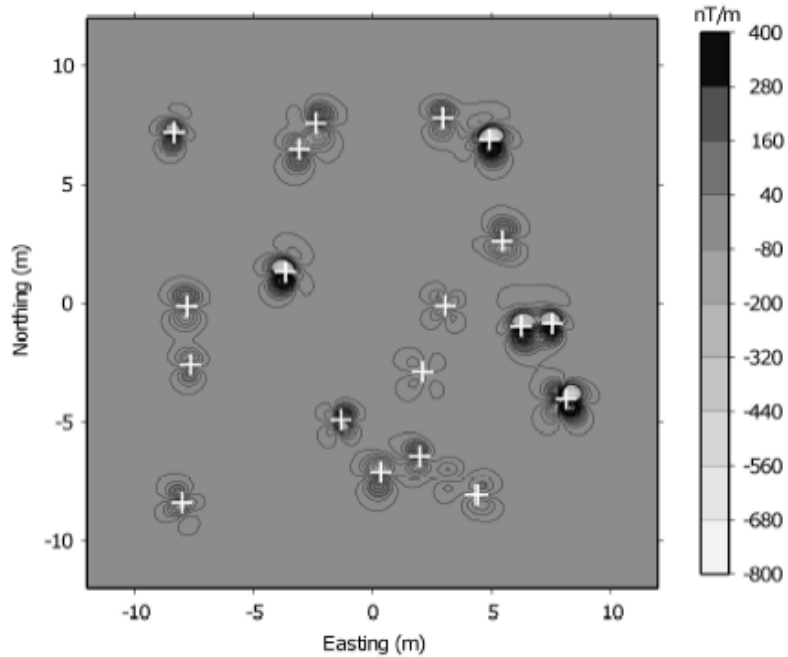


Figure 4.3: The horizontal (North-South) gradient response of the 20 random dipoles and the Euler detection result. The + indicates picked potential UXO anomalies. Similar to the results from the vertical gradient, the extended Euler deconvolution correctly picked 19 anomalies and missed one.

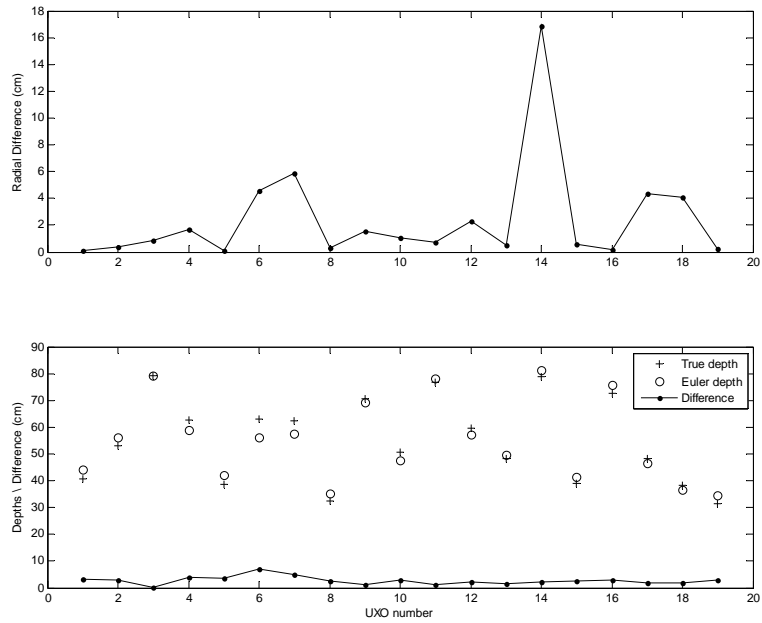


Figure 4.4: Comparison of true anomaly source parameters with those estimated during the automated detection using extended Euler deconvolution on the horizontal gradient data.

The synthetic data sets have demonstrated the concept of extended Euler deconvolution and the automatic picking of UXO-like anomalies applied to magnetic gradient data. Though there was no noise present, the algorithm missed an anomaly because of the overlapping signals from multiple surrounding anomalies and only had one false alarm. The missed anomaly in all three data sets illustrates one potential weakness of the algorithm in that the extended Euler method may have difficulties when multiple anomalies are close together. The picks it did make, however, had high structural indices and the calculated 3D locations of the dipoles were quite accurate. The nature of the algorithm allows for the automatic picking of dipole-like anomalies for large data sets with minimal human interaction. This, in turn, will significantly reduce processing time in the detection stage and allow one to expend more time on discrimination.

4.4. Summary

The end goal of this component of the project was to maximize the probability of detection of munitions and minimize the false alarm rate by development of an improved automated technique for detection of magnetic anomalies associated solely with buried UXO and non-hazardous metal items. With the development and testing throughout this project, simulations hint that gradient data may prove the appropriate data type for best achieving this goal. In addition, the application of the integrated approach to gradient data may enable improved detection of potential UXO targets for subsequent quantitative interpretations based on the higher-order moments.

5. Reducing False Detections due to Data Noise and Magnetic Geology

5.1. Introduction

The results in the synthetic examples from the first chapters amply illustrated the concept of Euler deconvolution-based detection algorithm and its efficacy for identifying potential UXO related magnetic anomalies in total-field and gradient magnetic data. In practical applications, however, noise will strongly influence the performance of any detection algorithm and lead to false alarms. Thus, a practically applicable algorithm must be able to deal with noise effectively and reliably. Data noise in UXO magnetic data can be introduced during the acquisition stage or come from geology. While established quality control and assurance procedures may significantly limit the acquisition error and its adverse effect on the automated detection method, geologic noise will always be present. When the wavelengths of geologic noise are comparable with those of UXO anomalies, it poses a severe challenge. We examine the issue here and develop a statistical method for reducing false alarms based on amplitude analysis.

To illustrate the adverse effect of noise on automated detection, return to the total field data shown in Figure 2.1 (repeated in Figure 5.1). We use a set of spatially correlated noise obtained by applying a low-pass filter to a set of uncorrelated Gaussian numbers generated over the data grid. The original random numbers have a standard deviation of 2 nT. The low-pass filter is a 4th order Butterworth filter with a cutoff wavelength of 12.5 m. The use of such a noise model is meant to simulate the realistic noise contaminating UXO magnetic data, which are often Gaussian but correlated spatially. The noisy data are shown in Figure 5.1 with a histogram equalized color scale.

Using the same detection parameters as in chapter 2, the automated detection algorithm has produced a larger number of false detections (Figure 5.2). Clearly, the presence of

high frequency noise has had an adverse effect of the detection capability of the algorithm. The reason is that many of the features in the data produced by high-frequency noise have the same scale lengths as the UXO anomalies. Theoretically, the cause of these false alarms lies in the fact that the extended Euler deconvolution solves for the source location and structural indices based on the decay of the field within the window regardless of amplitude. The rate of field decay is quantified through the shape of magnetic anomaly alone. Spatial variations in data due to the presence of noise can appear partially dipolar and yield high structural indices, which lead to false alarms. This is compounded by the need for a lower SI threshold since the field data usually have undergone several processing steps such as gridding and filtering that tend to reduce the SI of an anomaly from its theoretical value. Further processing is required to winnow these false alarms.

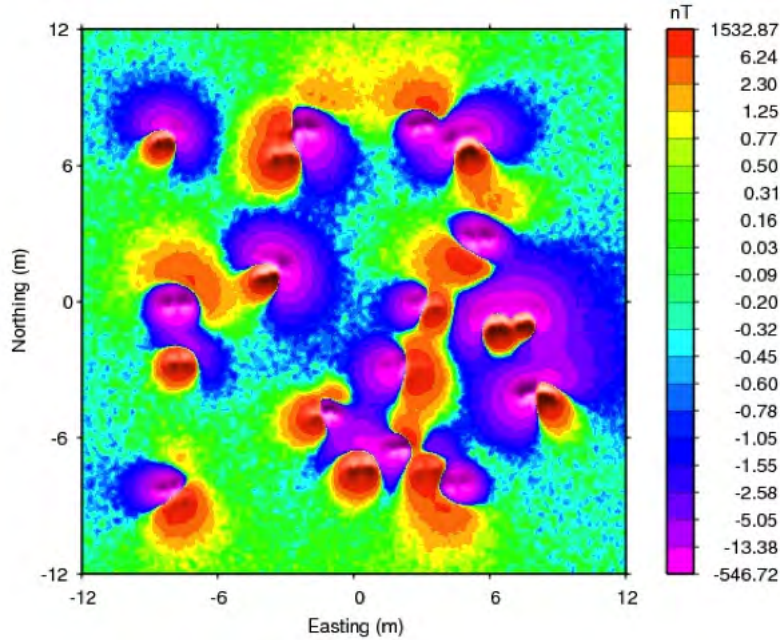


Figure 5.1: Synthetic total-field data contaminated by correlated Gaussian noise. The noise is obtained by applying a low-pass filter with a cutoff wavelength of 12.5 m.

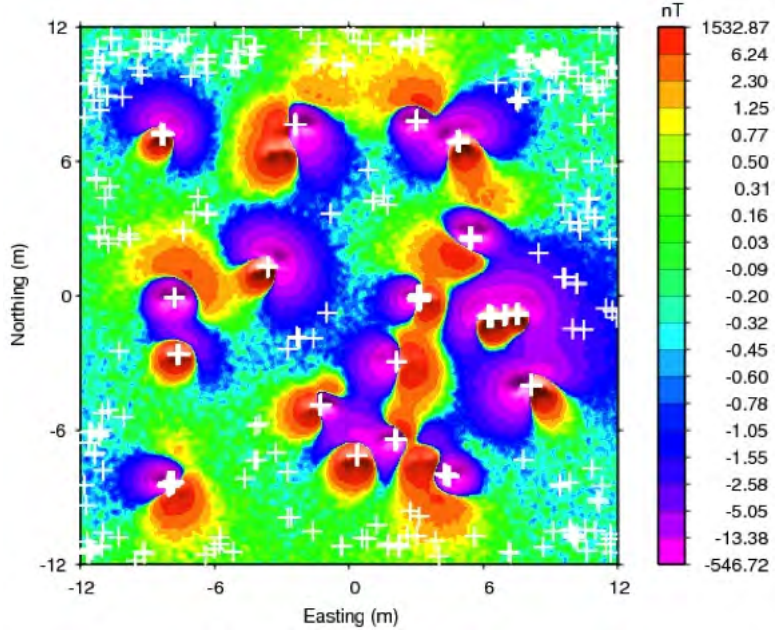


Figure 5.2: Detection results of noisy synthetic total-field data in Figure 5.1. There are a large number of false detections.

Therefore, post-processing of the automated detection result is required to recognize these false detections. We address this issue by developing an amplitude analysis approach based on statistics of the detection results. The method significantly reduces the number of false detections by statistically identifying weak anomalies in associated amplitude data and discarding solutions that appear to be valid based on phase information but belong to false solution due to noise in the data. We first develop the method by examining the synthetic total-field anomaly in Figure 5.1, and associated detection results (Figure 5.2). We then demonstrate improved detection results for magnetic data associated with two difficult field datasets from ESTCP Project MM-0533 and SERDP Project MM-1414. These two data were selected because the geologic and acquisition noises generate an unacceptable number of false anomalies in the first, and masks the UXO entirely in the later.

5.2. Identifying and removing false detections using amplitude analysis

We now proceed to develop the statistical method to identify and remove false detections from automated Euler detection algorithms. To achieve this, we turn to the complementary information that was neglected in the Euler deconvolution: the amplitudes of magnetic anomalies. We have observed that the strengths of magnetic anomalies are in general weaker for surface clutter and small-scale geologic features. This reflects the fact that modern magnetic data are generally of high quality and false anomalies due to survey errors cannot be too large in amplitude. Furthermore, these features are usually small in physical size or weak in magnetization. It follows that knowledge of the source strength will provide additional information for us to distinguish between strongly magnetic UXOs and other sources. Strictly speaking, one may desire to carry out parametric inversion to recover source strengths, i.e., dipole moments, of all anomalies detected in the first stage. However, that would be an expensive proposition not justified for anomaly detection. We choose to rely on the amplitude data computed from the total-field data as a proxy to the source strength.

We define the amplitude, A , as the magnitude of the anomalous field vector, \vec{B}_a

$$A = |\vec{B}_a| = \sqrt{B_{ax}^2 + B_{ay}^2 + B_{az}^2}, \quad (5.1)$$

where B_{ax} , B_{ay} , and B_{az} are respectively the three components of the anomalous field \vec{B}_a .

The measured total-field anomaly is the projection of \vec{B}_a onto the inducing field direction. The amplitude data is an approximate envelope of total-field anomaly over all possible magnetization directions (Nabighian, 1972; Shearer, 2005) and the peak is centered nearly directly above the corresponding source in 3D. Furthermore, the amplitude peak value is proportional to source strength and inversely proportional to the depth raised to the power of structural index, N . Consequently, we can obtain a relative measure of the source strengths by simply examining the peak amplitude of each anomaly detected by Euler deconvolution. Thus, we define the relative source strength as

$$|\mathbf{m}| \propto h^N A(x_o, y_o) \quad (5.2)$$

where $|\mathbf{m}|$ is the magnitude of the dipole moment, h is the depth of the dipole, and $A(x_o, y_o)$ is the magnetic amplitude data at the location (x_o, y_o) of the detected anomaly. Scaling the amplitude data by the rate of decay using the structural index, which is equal to 3 for total-field data, is equivalent to removing the decay of the field with distance. A similar approach has also been used by Sinex *et al.* (2005) to evaluate strengths of different field components in UXO discrimination. For each anomaly, we choose to use the mean depth of the clustered Euler solutions. We can use either the theoretical value of 3 or the SI calculated by extended Euler deconvolution; numerical tests have indicated that the final detection results do not differ significantly.

Generating these relative source strengths is straightforward and computationally inexpensive. It requires three linear transforms of the total-field anomaly to obtain the three orthogonal components in Eq. (5.1). This step is accomplished in wavenumber domain (Pedersen, 1978). Scaling the amplitude data at each detected anomaly location according to Eq. (5.2) then yields relative source strengths for all dipole anomalies from the Euler picks.

It is observed that the anomalies predominately have rather weak sources that are nearly zero and only a few anomalies are strong and deviate from the majority. Closer inspection of the location of these anomalies show that the strong sources are indeed generally associated with the UXO anomalies identifiable by visual inspection and the weaker ones are scattered in the portion of the data map where the signal-to-noise ratio (SNR) is low. The relative source strengths of the Euler solutions shown in Figure 5.2 are summarized in Figure 5.3, which displays the histogram of the logarithm of the source strengths.

The source strengths have a bimodal distribution. The first mode is related to small-amplitude features due to noise in the data, whereas the second mode is related to the

actual dipole anomalies and “spray” from Euler detection, which are the false solutions produced by partially captured anomalies in the moving window. The presence of the sprays necessitated the need for clustering the solutions in the preceding two chapters. Overall, the false detections in Euler solutions are associated with either noise in the data or resulted from the spray effect of Euler deconvolution. Both groups have weaker relative source strengths.

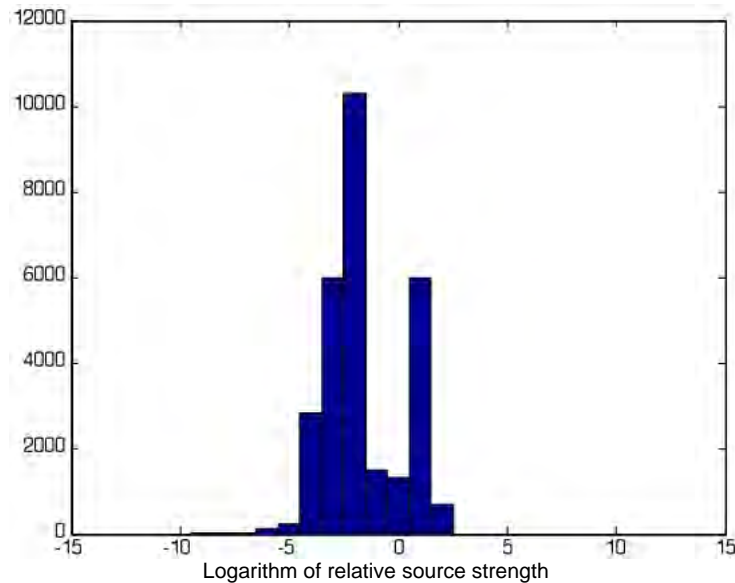


Figure 5.3: Statistical distribution of the logarithm of the relative source strengths of anomalies detected in the synthetic noisy data shown in Figure 5.1. The source strengths are clearly bimodal. The first mode is related to small-amplitude features due to noise in the data, whereas the second mode is related to the actual dipole anomalies and associated spray from Euler detection.

The problem of distinguishing between UXO anomalies and false alarms now becomes one of deciding a threshold level of source strengths. This can be accomplished in two ways. The first must use prior information about the type of UXO present at a site, and our understanding of actual magnetic source strengths of UXO items can be used to decide on a threshold. Alternatively, we can extract the threshold directly from the statistics of the relative source strength. We examine the latter here.

Given the origin of the Euler solutions whose relative source strengths belong to the first group in Figure 5.3, we can confidently discard them as false alarms. The more challenging part is how to choose a threshold for the second group. Based on the fact that there are many more Euler solutions that are spray than actual solutions that correspond to real sources, a reasonable threshold would be the mean plus one standard deviation. Applying this criterion and discarding Euler solutions below the threshold in Figure 5.2, we winnow most of the original solutions and only 21 solutions remain as potential UXO anomalies (Figure 5.4). This is a huge reduction. Of the 21 remaining anomalies, 17 are actual UXO anomalies and 4 are false alarms. We have missed three UXOs. This is a reasonable result given that the original synthetic data set was generated to be a challenging one. The random dipole strengths simulate the presence of different types of UXOs and the close proximity of several anomalies simulates clustering.

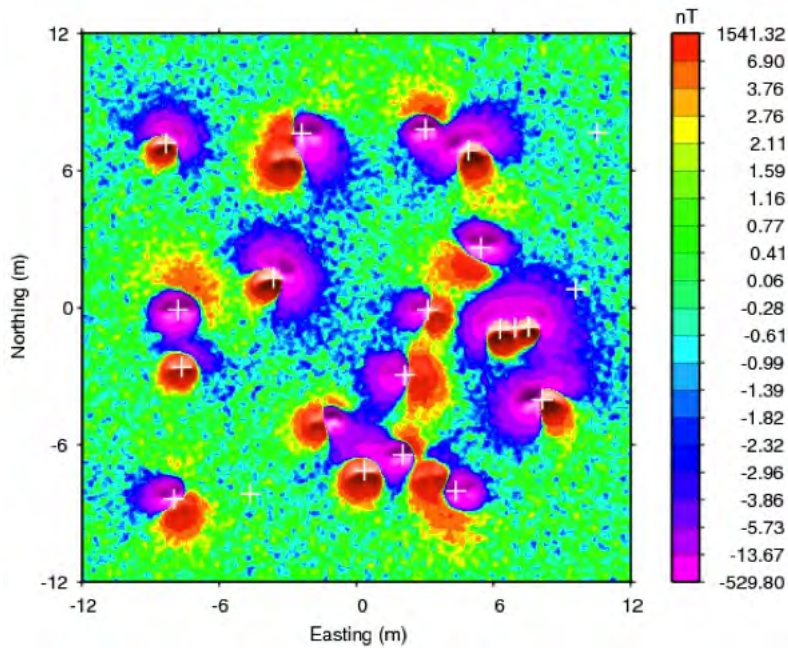


Figure 5.4: The final detection results after applying the threshold based on amplitude analysis. The majority of the false detections are removed and a total of 21 remaining anomalies are a reasonable set to be analyzed in the discrimination stage.

5.4. Field Examples

We next apply the amplitude analysis to two field examples. The first is a subset of total-field data acquired at the former Camp Sibert, Alabama. The second data set was acquired in Helena Montana as part of SERDP project MM -1414. The former Camp Sibert data set has small scale noise that is common to UXO magnetic data, whereas the Montana data exemplifies strong geologic responses that mask UXO anomalies.

5.4.1. Camp Sibert

A subset of total-field magnetic data from Camp Sibert in Gadsden, Alabama (Figure 5.5) is used to test the algorithm. The data set was acquired as a part of Environmental Security Technology Certification Program (ESTCP) Project MM-0533 (2007). There are clear magnetic anomalies produced by UXO items and surface clutter as well as by geologic features that are comparable in scale length and shape. This data set typifies geologic noise in UXO magnetic data and the associated difficulties in detection and discrimination. It is instructive to examine the data image in Figure 5.5 and envision the difficulties of picking potential anomalies by eyesight or thresholding total gradients. The number of probable anomalies and the influence of geologic noise would likely defeat such an effort. The difficulty is illustrated by the large number of anomalies picked by the simple application of the Euler detection algorithm. When applying our automated detection algorithm in its simple form, we first chose a threshold of $N > 2.2$ for SI. The resultant anomalies are shown in the top panel of Figure 5.6. Clustering the solutions within a 1 m radius yields 161 anomalies in the 30 m by 30 m area (bottom panel of Figure 5.6). Only a few of these anomalies are clearly UXO related. Although the majority of the remaining anomalies are dipolar in shape (and have high structural indices), they are manifestations of the noise within the data set.

Clearly, the noise in the data has adversely affected the automated detection algorithm in a similar manner as in the simulated synthetic data. The majority of the detections based on the simple application of Euler detection are due to noise in the data. Applying the

amplitude analysis to the unclustered solution in Figure 5.6 (top panel), the histogram distribution of the relative source strengths are shown in Figure 5.7. Once again, we observe a bimodal distribution on a logarithmic scale. The first group is related to the high-frequency noise in the data, and the second group is related to the actual UXO anomalies. The characteristics of this distribution are very similar to that in the case of synthetic data. Again we observe that a majority of the detected anomalies have very small amplitude. They are produced by the noise in the data.

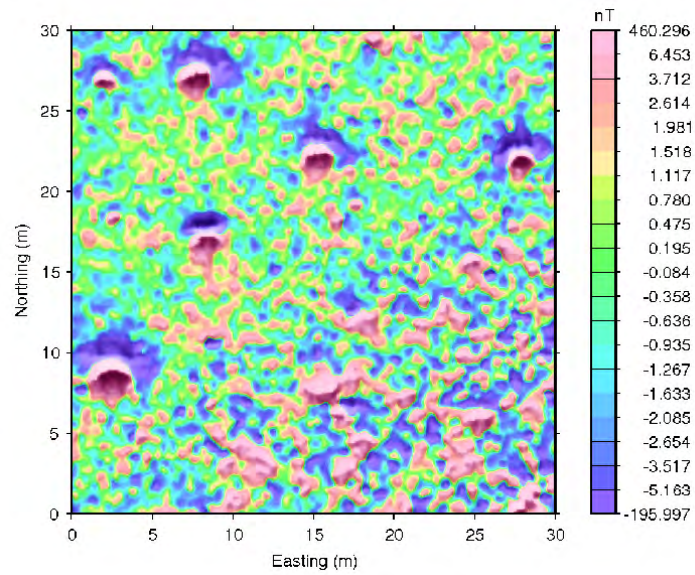


Figure 5.5: Total-field magnetic data from the Former Camp Sibert, Alabama. Several UXO anomalies are clearly present, but there are also many small-scale features with wavelengths comparable to UXO anomalies.

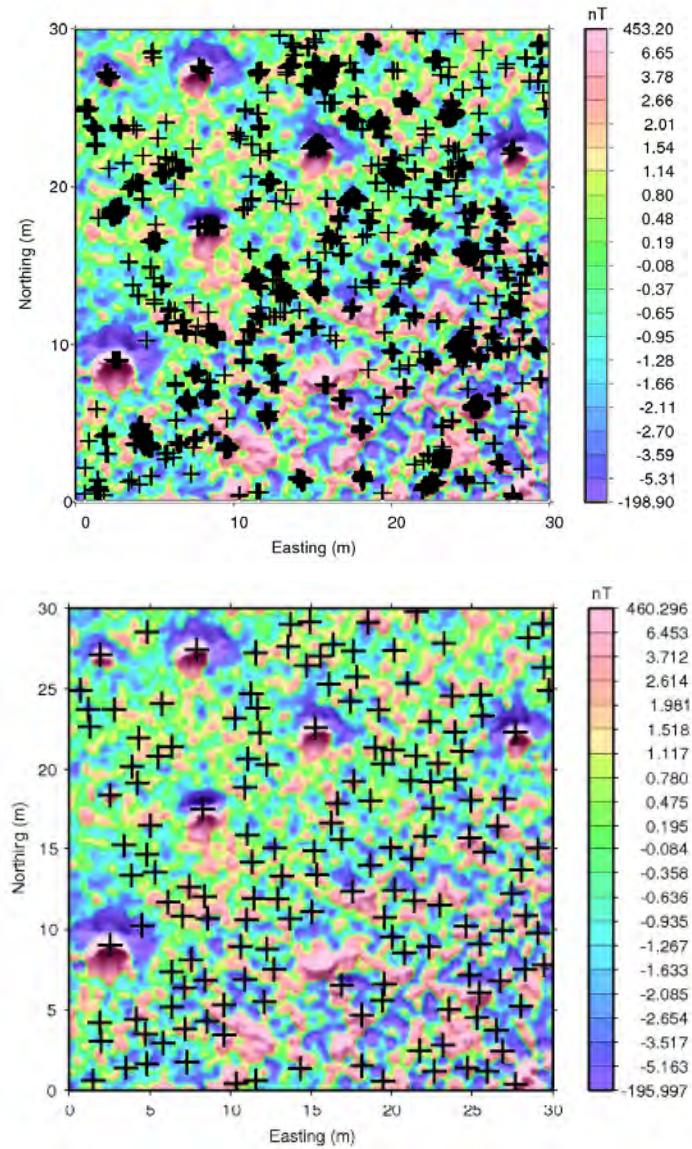


Figure 5.6: Initial Euler detection for a subset of field data from Camp Sibert. The color image with the corresponding color bar shows the total-field anomaly over a 30 m by 30 m area. Superimposed on the data image are the ‘+’ marks indicating the anomalies detected with a SI threshold of 2.2. The top panel shows all the solutions with an SI above the threshold. The bottom panel shows the result of clustering using a cluster radius of 1 m. The algorithm picked a total of 161 anomalies. All the UXO anomalies were correctly identified but there were a large number of false alarms clearly associated with background noise.

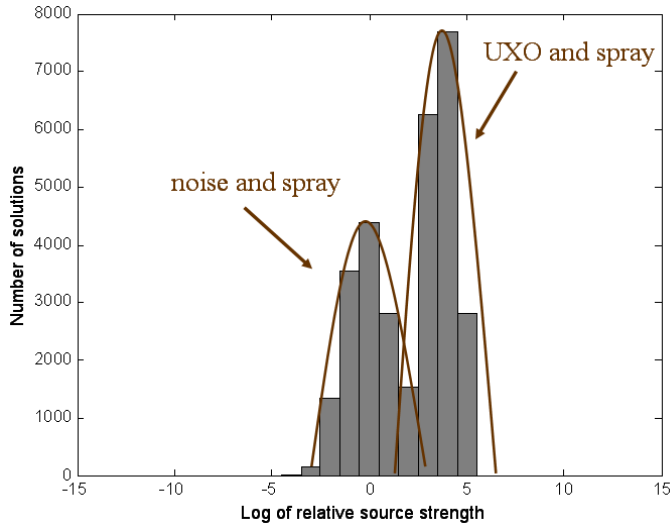


Figure 5.7: Distribution of the logarithm of the relative source strengths of anomalies detected in the former Camp Sibert data shown in Figure 5.6. The source strengths are bimodal. The first mode is related to small-amplitude features due to noise in the data, whereas the second mode is related to the dipole anomalies and associated spray from Euler detection.

Using a threshold again equal to the mean plus one standard deviation in the second group, we discard the Euler solutions below this threshold. These solutions lie within the noise and in most cases would not be considered UXO. This process winnows most of the Euler picks and identifies 16 remaining ones as having significant strengths. To further confirm the validity of the criterion, we have examined the anomaly depths estimated by the Euler deconvolution. All 16 remaining anomalies are located below the ground surface. It is re-assuring to note that all the discarded anomalies lie near the ground surface or appear as above it. Therefore, a simple threshold based on the condition that the source depth must be greater than the observation height above the ground would have winnowed some false alarms. However, amplitude analysis is still needed to remove those false alarms appearing to be just below the ground surface and have low relative source strengths.

The final 16 potential UXO anomalies chosen through amplitude analysis following the extended Euler deconvolution are shown in Figure 5.8. All could be interpreted as

potential UXO anomalies because of the dipole nature of each shape. Dig results (prior to this work) from the same area targeted 10 anomalies, 4 of which were actually UXO and 6 others scrap metal (Figure 5.8). Euler solutions existed for 8 anomalies from the dig results, meaning only half dipole anomalies chosen by the algorithm were not of interest in discrimination techniques. The results did not miss any UXO and the average of the structural indices for the UXO anomalies was 2.6. Thus, the automated detection algorithm with the added amplitude analysis has worked well in this case.

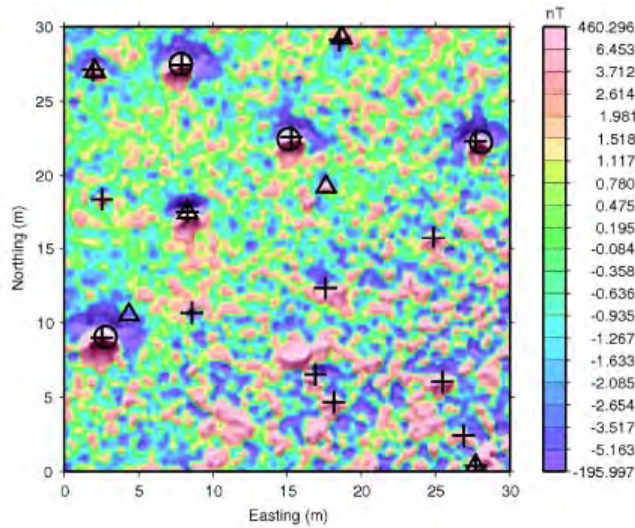


Figure 5.8: The final 16 Euler solutions (+) obtained through source-strength analysis, cleared UXOs (O) and cleared non-UXO (Δ) anomalies. The two non-UXO items cleared from discrimination methods were initially picked by the algorithm, but then discarded during the amplitude analysis.

5.4.2. Montana

The second data set for testing our detection algorithm was acquired for SERDP project MM- 1414. The data set is located at the Chevalier Ranch in Helena, Montana. The geology of the area is characterized by a system of mafic dykes with strong magnetic signals intruding into a relatively non-magnetic host. The responses from these magnetic dykes can mask the UXO entirely and render detection algorithms ineffective. We use a

subset consisting of three UXO anomalies superimposed on a strong geologic feature in the current test.

Figure 5.9 display the total-field magnetic data from Helena, MT. There are three emplaced UXOs whose magnetic anomalies are allocated along the peak of the geologic anomaly. However, straight forward application of the Euler detection algorithm missed all three and only detected an anomaly in the southwest corner of the map. The intended targets are the three located on the peak of a geologic anomaly. Clearly the geology is severely hindering the automated detection. Therefore, it is necessary to carry out pre-processing to remove the geology before attempting UXO anomalies. The processing will invariably introduce noise and it will in turn affect the Euler based detection. This is likely to be a common scenario when strongly magnetic geology is present. We therefore examine it here.

The separation of UXO anomaly and geologic responses is an on-going research topic. Two methods based on wavelet filtering and iterative Wiener filtering respectively were developed in SERDP project MM-1414 (2007). It continues to be a research direction in the current project. The applicable method for the separation will be data set dependent. For the data set shown in Figure 5.9, we have found that wavelet filtering has performed well. In this approach, we rely on the location adaptive property of wavelet filtering to separate the geology and UXO response. The assumption is that UXO anomalies are represented by wavelet coefficients on finer scales localized in spatial position while the geologic responses are concentrated more on coarser scales and spread broadly over spatial location. We used the symmlet family of wavelet with seven vanishing moments to carry out the separation. The resulting residual data are shown as the color contour in Figure 5.10. It is clear that the wavelet filtering has performed reasonably well in removing the majority of the geologic responses. However, the residual also contains high-frequency artifacts from the wavelet filtering process.

Direct application of Euler detection with SI threshold and clustering produced the detection results shown in Figure 5.10 (indicated by pluses). The algorithm has

successfully detected the three intended targets, but there are many false detections due to the noise and high-frequency residual. Thus the outcome of the Euler detection is similar to the example from Camp Sibert. Amplitude analysis is again required to winnow the false detections.

We apply the amplitude analysis to the Euler solution after thresholding and before clustering. The resulting histogram is shown in Figure 5.11. The relative source strengths again have a bimodal distribution on a logarithmic scale. The first peak is due to both the noise in the original data and the high-frequency residual from the separation. Thus, the behavior of Euler detection on the pre-processed data is similar to that when it is applied to data that contain only high-frequency noise and small scale geology.

Using a threshold that is equal to the mean plus one standard deviation of the second peak in Figure 5.11, we retain four anomalies as the final detection (Figure 5.12). Of these, one is the anomaly located near the southwest corner, and three are the intended targets. Thus, the application of Euler detection with amplitude analysis has worked well on the pre-processed data that removed the long wavelength geology.

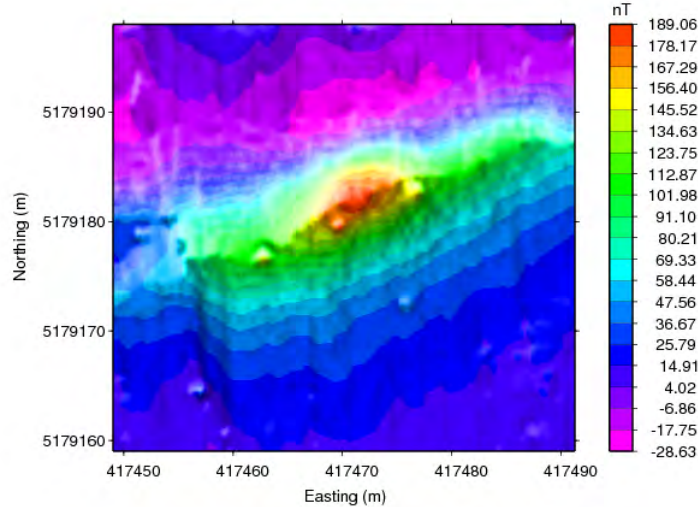


Figure 5.9: Total-field anomaly data from Chevalier Ranch, Montana. There are three emplaced UXOs on top of a magnetic dyke. The magnetic response produced by the dyke has completely masked the UXO responses.

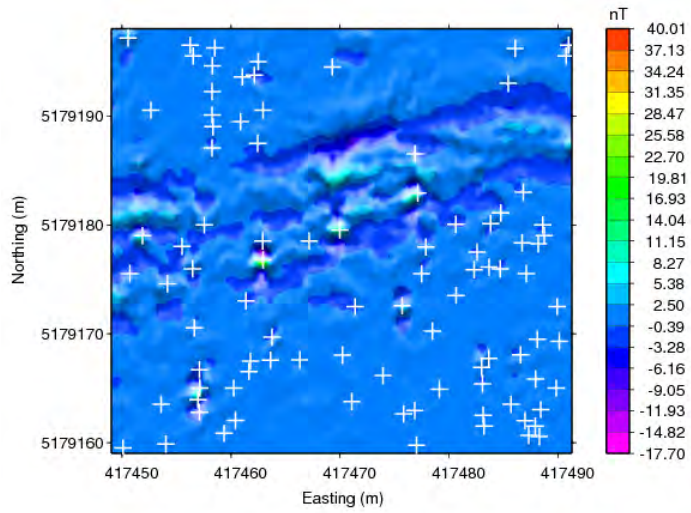


Figure 5.10: Clustered solution after a threshold of 2.2 and clustering.

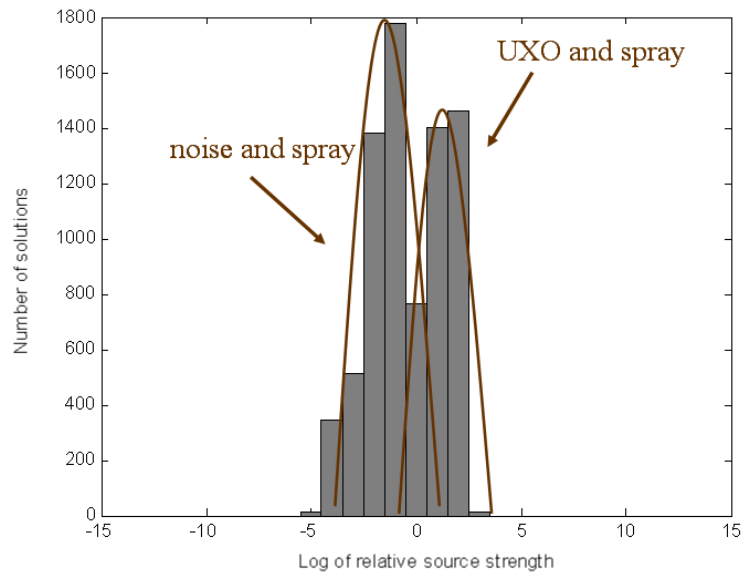


Figure 5.11: Distribution of the logarithm of the relative source strengths of anomalies detected in the wavelet-filtered Montana data shown in Figure 5.10. The source strengths are bimodal. The first mode is related to small-amplitude features due to noise in the data, whereas the second mode is related to the dipole anomalies and associated spray from Euler detection.

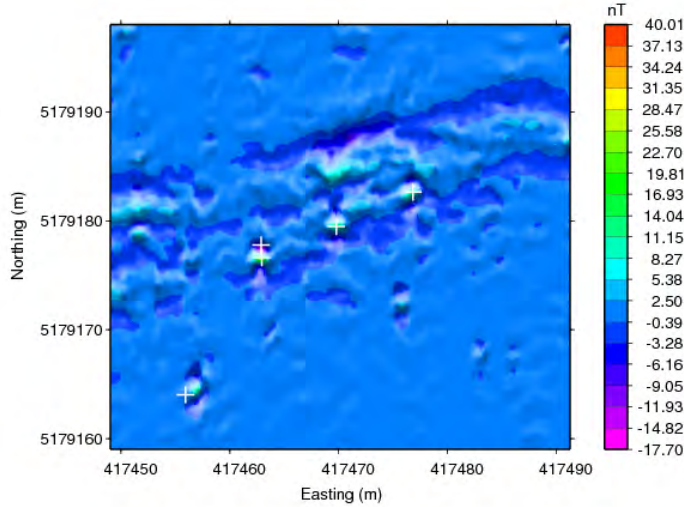


Figure 5.12: Final detection result obtained from the wavelet filtered data after the amplitude analysis is applied.

5.5. An alternative approach to the choice of amplitude threshold

The statistical approach to selecting a threshold level for winnowing false detections is general and is applicable to data sets consisting of varying noise characteristics and UXO types. Therefore, it is the preferred approach in general. However, when a single type of UXOs is present and the noise characteristics are significantly different from the UXO anomalies, an alternative and more straightforward approach may be used. In this approach, we work with the clustered solution and find the threshold by directly detecting a break point between the UXOs and noise-generated anomalies. We describe it in this section using the example of former Camp Sibert data (Figure 5.6).

Plotting the relative source strengths of clustered solution in ascending order shows two characteristic segments with a sharp change in between. The first segment contains all the weak anomalies due to noise and is nearly flat. The second segment contains a small number of anomalies and exhibits a nearly vertical rise, indicating highly variable and strong sources. The anomalies in this group are potential UXOs. Therefore, the problem

of separating the two groups becomes one of detecting a break point between the two, which must be near the corner of the source-strength plot (Figure 5.13).

We have examined two criteria for detecting the break. The first is the rate of increase in sorted source strength as a function of the index calculated over a running window; and the second is the standard deviation of source strength over the same window. Figure 5.14 shows the rate of increase and standard deviation calculated using a 3-point and 5-point window, respectively. We pick the break point to be the one just prior to the noticeable increase in either the rate of increase or standard deviation. Both criteria seem to perform well in detecting the break point. The result of this analysis is shown in detail by the inset in Figure 5.14. This break point is consistent with the threshold determined statistically using the histogram, and the resulting detected potential UXO anomalies are those shown in Figure 5.8.

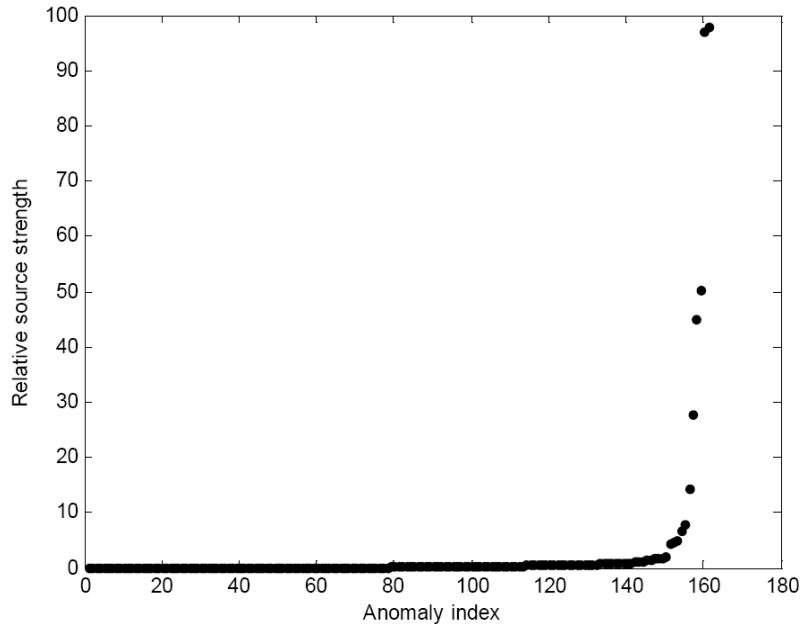


Figure 5.13: Sorted relative source strengths of all anomalies detected in Figure 5.6. The vertical axis shows the source strength and the horizontal axis is the anomaly index.

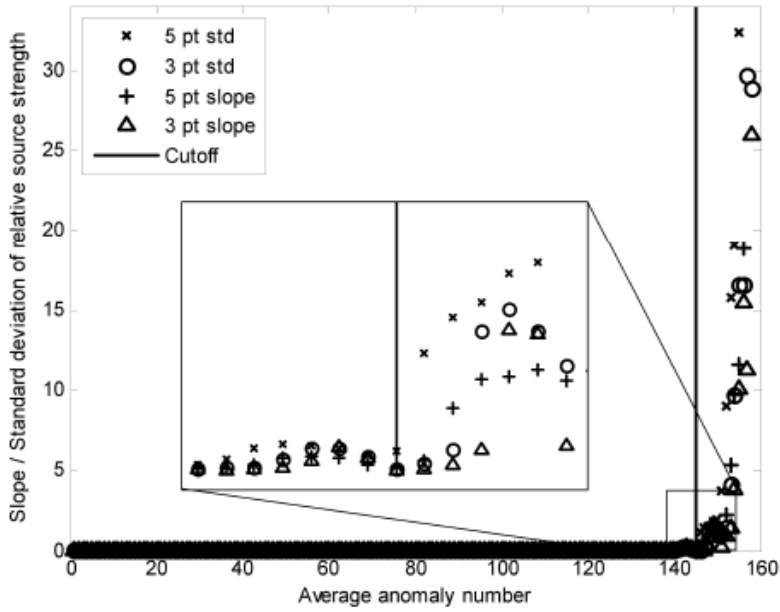


Figure 5.14: Rates of increase and standard deviations of sources strengths calculated within 3-point and 5-point windows, respectively. These curves all show a clear break point between the anomalies within the noise level and those standing out. The cutoff level is chosen to be the first large rate of strength increase or standard deviation. The inset zooms in around the point chosen.

5.6. Summary

The presence of background geologic anomalies and acquisition noise will influence the extended Euler solutions as expected. The criterion of looking for high structural indices can potentially lead to a large number of false alarms associated with background noise, as exemplified by the field data examples. To counteract this, we have developed an amplitude analysis technique that distinguishes between strong UXO anomalies and those caused by data and geologic noise and thereby reduces false alarms. The amplitude analysis uses the magnetic amplitude data scaled by the Euler depth and recovered structural index (SI) as the proxy to the actual source strength and only retains as the final detected anomalies the solutions whose source strengths are above a threshold. Two methods can be used to determine the threshold. The first examines the distribution of the logarithm of the relative source strengths of all anomalies with a high structural index

(without any clustering), and use the mean plus one standard deviation of the mode with higher strength as the threshold. The second approach works with clustered solution and determines a break point between the solution group related to noise and the group related to UXO. The first is a general method and the second appears to apply when the strength of noise is well below the strength of UXO anomalies. Application to two field data sets has demonstrated the effectiveness of the detection methods in noisy environments.

6. Separation of Strongly Interfering Geology

In this chapter, we demonstrate through field examples a summary of our accumulated tools for enhancing UXO targets in magnetic data by separating strongly interfering geology while preserving response of UXO-like sources.

6.1. Introduction

In most UXO data interpretations – both for magnetics and electromagnetics – the dominant state of practice is to interpret directly from a smoothed version of the true field. For example, the measured data can undergo several steps of processing that are equivalent implicitly to a low-pass filtering as a means of ‘filtering out’ the geologic component. While the approach is sometimes beneficial to the goal of enhancing UXO response, it can often lead to the undesired consequence of distorting the dipolar response of UXO. This becomes a hindrance to subsequent detection and discrimination algorithms which seek potential UXO through the dipole nature of their fields. The method is likewise not appropriate when a directional component of the environmental response has similar length scale as potential UXO.

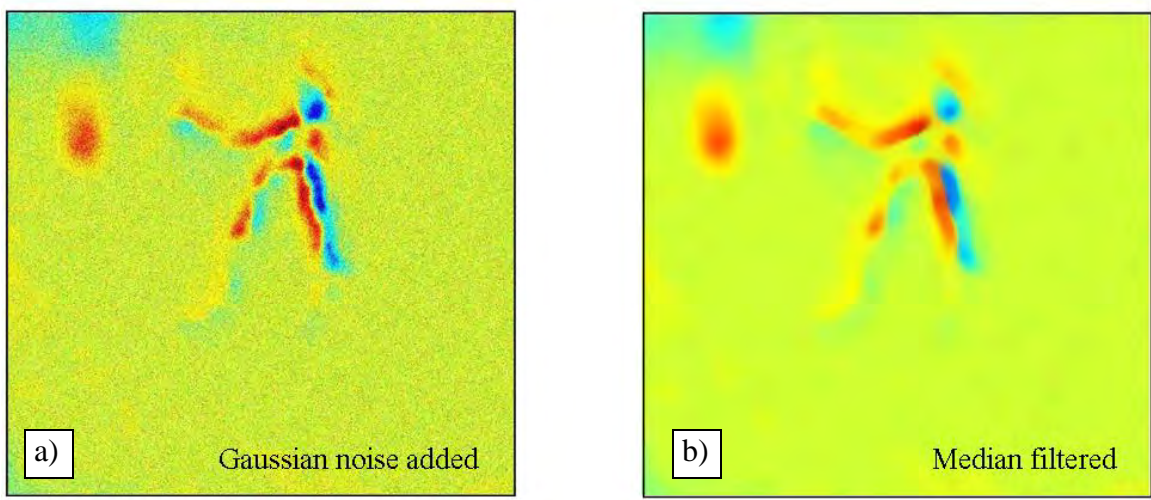


Figure 6.1: Demonstration of median filter for processing magnetic UXO data with strongly interfering geology. Data are leveraged from SERDP Project MM-1414 and collected in Helena Valley, MT. Buried within the interfering geologic background are three UXO. Panel (a) illustrates magnetic data with noise. Panel (b) shows processed data after applying a median filter. The data are a smoothed version of the original, preserving most of the geologic response and doing little to enhance UXO anomalies.

The second common practice is applying a median filter to the data and it is designed to extract isolated small scale UXO anomalies. Unfortunately, such a filter generally only produces a smoother version of the field data, preserving much of the interfering geologic component along with that of UXO. For example, in Figure 6.1 we demonstrate this result with magnetic data collected in Helena Valley, MT. The data are leveraged from SERDP Project MM-1414. Panel (a) is an image of the magnetic data containing the response of three UXOs within a strongly interfering response from environment. The data are further contaminated with Gaussian noise for illustrative purposes. We apply a traditional median filter, and the final result, panel (b) is nothing more than a smoothed version of the original. The geology is not ‘filtered’ from the data and the UXO are obviously not ‘enhanced’ for any subsequent detection and discrimination algorithm. *What is needed is a not a smoothing filter, but a means of separating UXO from interfering geology as a first and necessary step for target enhancement, regardless of one’s preference for subsequent detection method.*

Magnetic method is highly effective at detecting magnetic dipoles – all valid targets for later discrimination analysis. However, part of the difficulty of the method lies in the limited algorithms available to the UXO community to properly separate these compact features from often noisy field sites, while preserving the dipole response itself. In this chapter, we demonstrate a suite of robust methodologies, originating from SERDP Project MM-1414 and culminating with the completion of Task 1 of this project, for effectively separating the response of interfering geology and enhancing UXO component through additional processing if desired. We likewise show that there is no ‘one-for-all’ method to achieve the common goal of enhancing UXO response in magnetic data when moving from site to site. Rather, a collection of techniques must be available, depending on the nature of the geologic response, acquisition noise, heading errors, position accuracy, and UXO type/depth.

6.2. Separation of interfering geology, enhancing UXO response

In this section, we illustrate application of various processing algorithms for separating interfering geology and enhancing UXO response in magnetic data. While the results presented here are a collection of developments originating from SERDP Project MM-1414 and culminating with MR-1638, we bring them together to demonstrate the need for a ‘toolbox’ of processing algorithms in magnetics to achieve the common goal of separating the geologic response in varying magnetic environments, while preserving and/or enhancing UXO response for subsequent detection/discrimination algorithms.

6.2.1. Iterative Wiener

The first method is outlined in great detail in the second chapter of the January 2007 Annual Report for SERDP Project MM-1414, and that background material will not be repeated here. The Wiener filter (Wiener, 1949) is based on the spectral properties of the UXO and soil responses and can be tuned to data from specific sites. Therefore, successful application of the method depends largely on the knowledge of the power spectra of soil magnetism at a site. The result is a powerful processing algorithm tuned to

a specific site and valuable for separating the response of interfering geology and thus enhancing those of UXO. Through field activities such as those of MM-1414, such information is easily attainable, and development of an iterative Wiener filter for static magnetic data has demonstrated promising results. We provide here a brief summary of the approach and demonstrate the technique as one valuable separation algorithm for UXO magnetic problems.

In geologic settings like Chevalier Ranch in Helena Valley, MT, high and variable magnetic susceptibilities may reduce or completely mask the visible identification of buried metallic objects and increase the number of false anomalies that are selected for removal. The Wiener filter assumes that the collected field data is a summation of the desired signal and the background response and that the two components are not correlated. The iterative Wiener filter is a procedure based on the Wiener filter to separate geologic responses from UXO signals. Application of the Wiener filter involves the estimation of a transfer function defined by the ratio of the signal and data power spectra. The method can be further developed as an iterative approach to estimate the transfer function using the power spectra of the data and geologic noise from the measured field data set and limited forward modeling of UXO anomalies.

The iterative process is carried out by first applying the Wiener filter to the original data using an estimation of the background noise. The first iteration of filtered data is then used in the calculation of the transfer function as the data ($P_d(\omega)$) for the second iteration. Each successive application of the Wiener filter to a particular dataset will produce a filtered dataset where the noise has been suppressed slightly. The same background noise power spectrum is used in each calculation of the transfer function. The iterative process is repeated until the variation between successive filtered datasets is less than some prescribed limit. We have found that a 5% limit is adequate for many problems.

The first area, Figure 6.2a, shows an extensive linear monopolar anomaly (>50m strike length, ~100 nT) likely associated with a deeper mafic dyke. This data set is referred to

as the Dyke-site. The second area, Figure 6.2b, shows linear dipolar anomalies which are spatially compact (< 5m strike length, ~100-200nT anomaly) with a character that could be interpreted as a UXO response. This data set is referred to as the Anomaly-site. In both areas, three 76-mm projectiles have been buried.

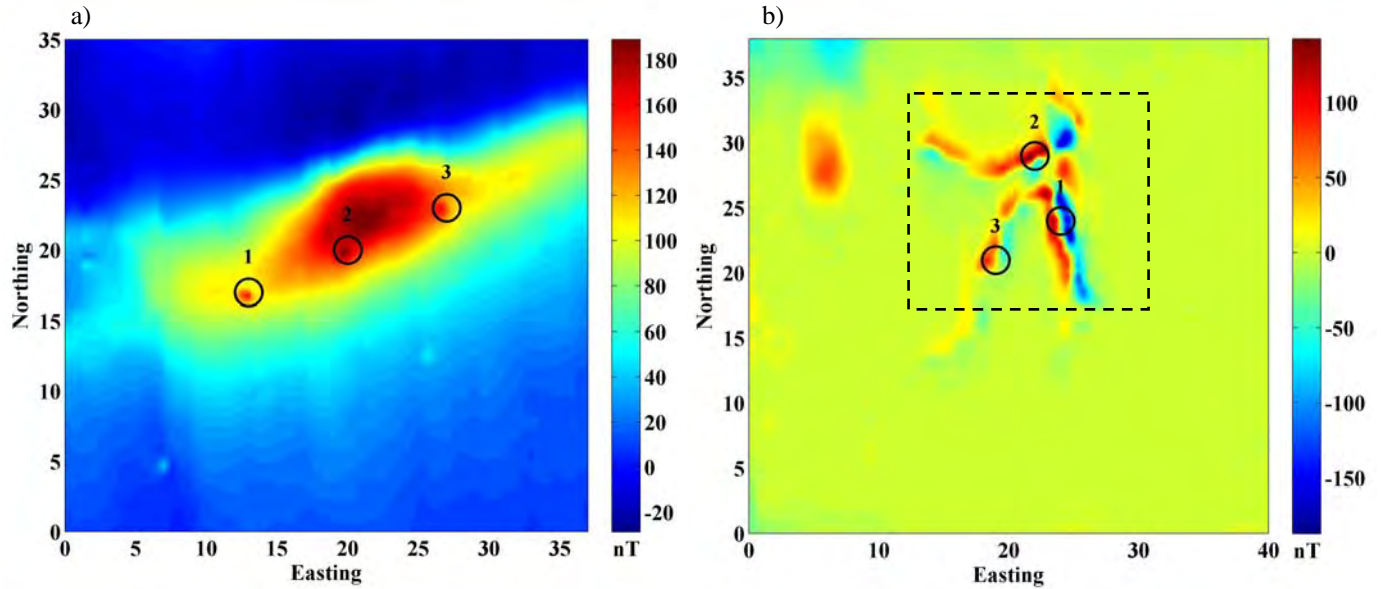


Figure 6.2: a) Magnetic data over the Dyke feature; b) Magnetic data over the Anomaly feature (only the area outlined in black was filtered). The black circles on both figures show the location of the buried ordnance items.

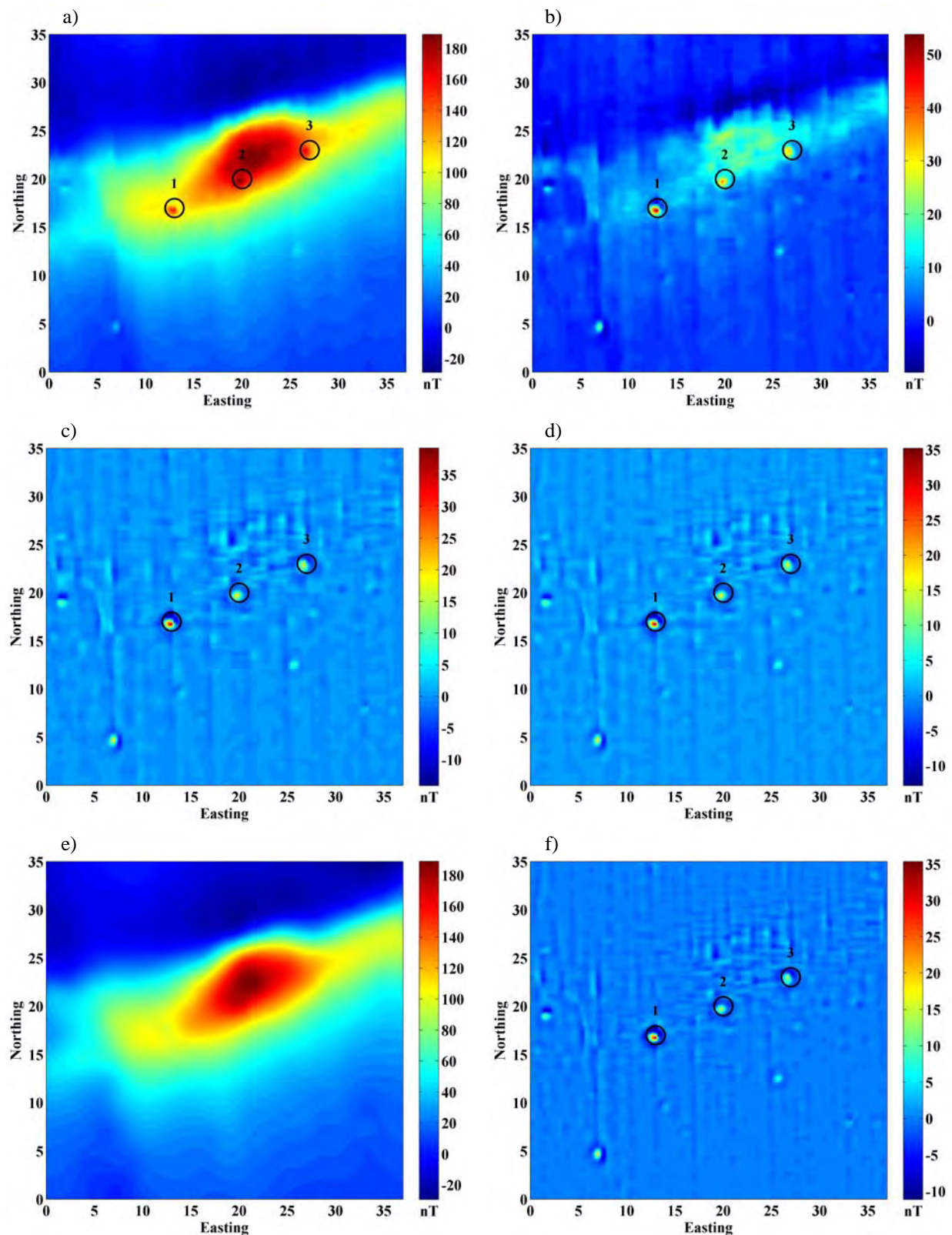


Figure 6.3: Dyke filtered data. a) field data; b, c, and d) 1st, 2nd, and 3rd iteration of the Wiener filter, respectively; e) noise estimation used for Wiener filter using a 2m sub-grid; f) high-pass Butterworth filtered data (2m wavelength cutoff).

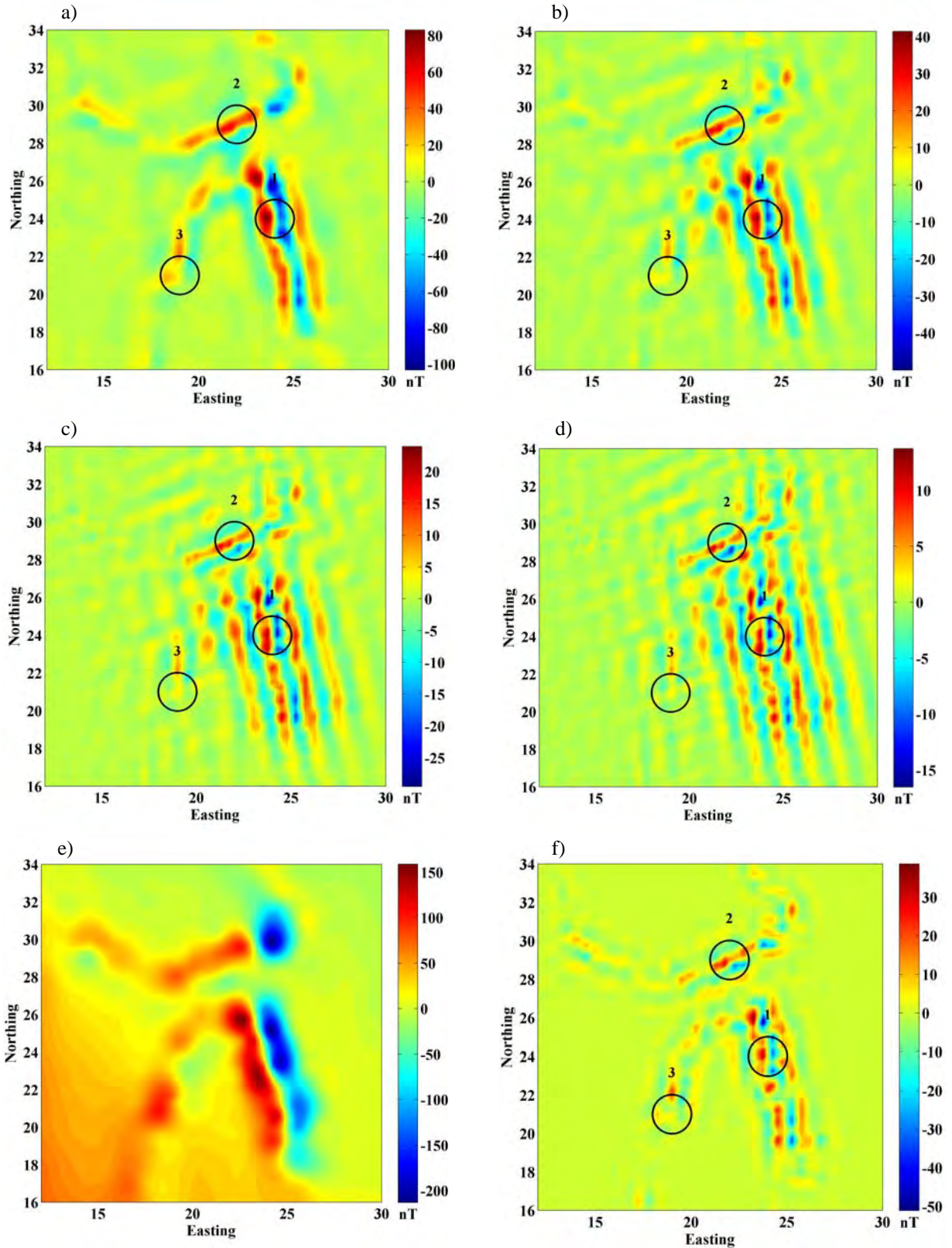


Figure 6.4: Anomaly filtered data. a) field data; b, c, and d) 1st, 2nd, and 3rd iteration of the Wiener filter, respectively; e) noise estimation used for Wiener filter using a 1m sub-grid; f) high-pass Butterworth filtered data (1.25m wavelength cutoff).

The filtered Dyke and Anomaly data are shown in Figures 6.3 and 6.4, respectively. The Wiener and high-pass Butterworth filter perform equally well on the Dyke data. The three buried ordnance items (identified with circles) are easily distinguished in the filtered data (Figure 6.3b – d). The noise estimation was derived using 2 meter sub-grids (Figure 6.3e). The Dyke structure is simple and easily estimated using the sub-grid method. In addition to the three ordnance items, a peak picking algorithm would probably identify three additional anomalies in the filtered data. These anomalies were not investigated during the field operations to determine if they are geologic or metallic in origin.

The Anomaly feature data produces poor results in both the Wiener filter and the high-pass Butterworth filter (Figure 6.4). Neither filter technique is able to recover any useful information from the buried ordnance. Although the background geology is suppressed, so is the signal from the ordnance items. It is important to note that none of the three buried ordnance items are visible in the preprocessed data. The anomalous signal is enveloped by the local geology. This data demonstrates that there is no ‘one for all’ processing algorithm appropriate for enhancing UXO anomalies for all sites.

6.2.2. Wavelet Transform

In parallel to the iterative Wiener filter, we have successfully identified another approach for separating the response of unexploded ordnance in areas of strong magnetic geology. The method is an adaptation of an automated wavelet filtering technique originally developed at Colorado School of Mines for processing gravity gradiometry data in petroleum exploration (Lyrio *et al.*, 2004). While the iterative Wiener filter from the previous section directly separates UXO-like anomalies from geology - by estimating a transfer function using the power spectra of the data and geology - the wavelet-based method identifies UXO-like anomalies by taking a more roundabout approach. First, localized UXO-type anomalies are treated similar to geologic noise, and as such are separated from the magnetic data using a wavelet transform-based denoising approach.

The remaining longer wavelength-component of the magnetic data, assumed to be the response of background geology, is then subtracted from the magnetic dataset. The residual after such a geologic response has been removed is assumed to be the magnetic response of UXO-like targets. Such a preprocessing approach for magnetic data in UXO holds similarities to the regional-residual separation processing techniques of the gravity method in exploration.

The difficulty of the above described approach for separating background from UXO in terrain contaminated with high and variable magnetic geology, is in the frequency content of the data. The magnetic signal of buried UXO and other metallic objects often have frequency content similar to that of the geologic response, such as observed at Chevalier Ranch, MT. Under these conditions, frequency domain filters may not always work well because they tend to remove frequencies globally, causing a generalized smoothing effect that substantially broadens features of interest and decreases their amplitudes. This is one of the main drawbacks of the median filter which is commonly applied to UXO magnetic datasets during preprocessing. Lyrio *et al.* (2004) appropriately describes the differences between these two fundamentally different processing techniques: smoothing versus denoising.

Wavelet transforms have two potential advantages over Fourier transforms for separating the magnetic response of UXO from magnetic soils. The first is multiresolution decomposition, and the second is time/space localization. The wavelet-based approach uses compactly supported orthonormal wavelets and selectively filters out localized high-frequency anomalies, such as those associated with UXO for the proposed approach, while having little effect on other sharp features present in the signal associated with geology. These properties have the potential to allow for a fast and accurate means of separating geology from UXO-like anomalies in magnetic datasets. We illustrate application of the method as a powerful (alternative) tool for separating geology from UXO in magnetic data. Details of the methodology, components, and implementation of wavelet transform-based denoising are provided in Appendix-A of the 2007 Annual Report for SERDP MM1414 and are not repeated here.

The automated wavelet-transform based de-noising method has been applied to the same UXO magnetic datasets from Chevalier Ranch in Helena, MT. At these sites, the magnetic susceptibilities associated with geology are found to either reduce or completely mask the magnetic response of our buried targets. The site we illustrate here for the wavelet filter, referred to as Dyke site, is the same location and magnetic data used for testing the iterative Wiener filter in the previous section (Figure 6.2a).

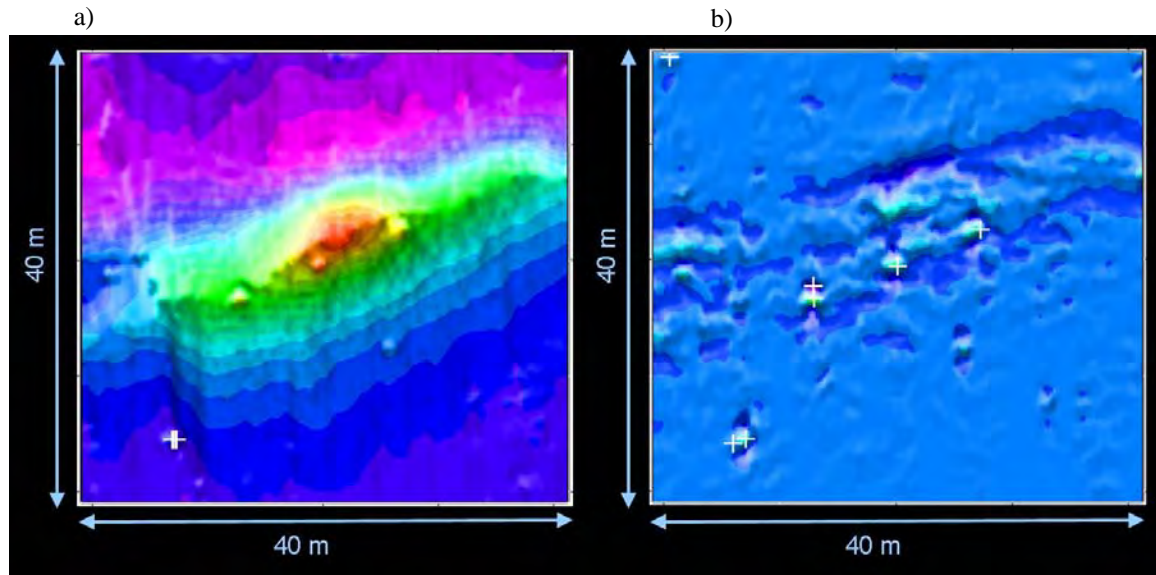


Figure 6.5: Total field magnetic data (a) collected at Dyke site from Chevalier Ranch, MT. Within the data are outlined the locations of the three buried UXO (dark circles) along the south flank of the larger magnetic anomaly associated with the volcanic dyke. The second image (b) is the magnetic data after applying the wavelet filter for separating out the geologic response. UXO responses are clearly visible in the preprocessed magnetic data.

In Figure 6.5(a), the large magnetic anomaly prevalent in the image is the magnetic response of a subsurface volcanic dyke with high magnetic susceptibility. Three 76-mm projectiles were emplaced along the south flank of this geologic anomaly, illustrated by circles in Figure 6.5(a). This site was selected for testing the filtering methods because the response of the magnetic dyke has the undesired effect of obscuring the signal of buried UXO, significantly reducing the dipole response, and hindering current detection

and discrimination techniques. In addition, the difference in frequency content, amplitude, and aspect ratio between the magnetic response of UXO and geology at this site provides useful information about the conditions under which wavelet-based separation will and will not be appropriate. This site is a clear example of the need to separate the response of UXO from geology in strong magnetic environments.

Figure 6.5 illustrates the magnetic data collected over the Dyke (a) before wavelet preprocessing, and (b) after separating the geology using a wavelet filter. The wavelet approach for this site, as described previously, treats the UXO anomalies as the residual after removing the higher wavelength monopolar magnetic structure associated with the volcanic dyke. The wavelet transform approach has successfully separated the large background response from a magnetic intrusive and allowed for subsequent automated detection.

6.2.3. Linear Feature Analysis & Removal

The performance of any detection algorithm is dependent on the signal-to-noise ratio. The basis for most methods is either identifying compact anomalies above a specified amplitude threshold, or calculating the decay rate of the observed field. For either approach, if enough noise is present, the results deteriorate.

In many magnetic datasets for UXO, such as Camp Sibert (Figure 6.6), background interference from geology typically appears as magnetic lineaments. These ridge-like features have distinct differences in character than the more compact UXO and scrap anomalies, and these interfering structures can be identified through linear feature analysis for subsequent separation.

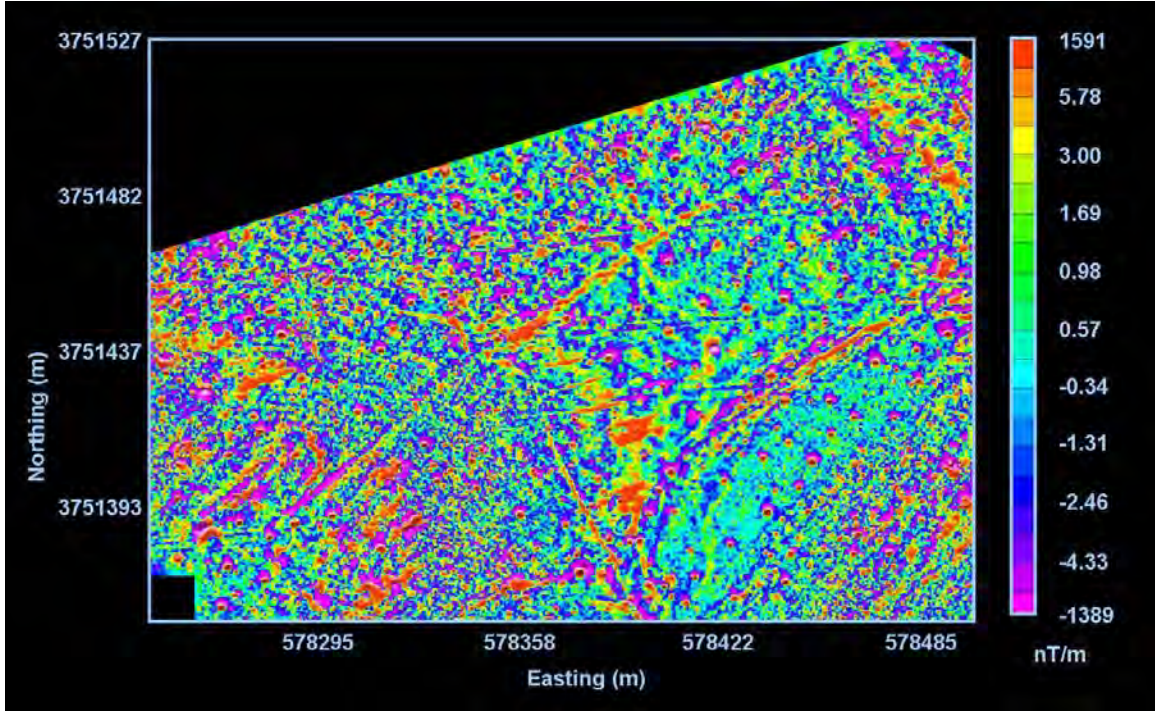


Figure 6.6: Total field magnetic data collected at Camp Sibert, AL. The strongly interfering magnetic background manifests as magnetic ridges in the data. The difference in curvature between these magnetic lineaments and compact UXO provides a foundation for separating the two by linear feature analysis.

Geologic anomalies such as those within Figure 6.6 typically contain larger aspect ratios than isolated or clustered ordnance-type items. We have applied Hansen & deRidder's (2006) technique for analyzing and removing linear features to identify geologic anomalies that typically are elongated and have a larger aspect ratio. The method then seeks to determine the aspect ratio and orientation of ridge-like features in magnetic data by examining the 2D curvature tensor,

$$\underline{\underline{C}} = \begin{pmatrix} c_{xx} & c_{xy} \\ c_{xy} & c_{yy} \end{pmatrix} \quad (6.1)$$

The ratio of eigenvalues of the tensor indicates whether a particular anomaly is round or has a strike direction. The eigenvector of the smaller eigenvalue then identifies the strike direction of geologic anomalies, if any.

Once magnetic ridge orientation is identified through linear feature analysis, we then apply a directional filter, specifically an F-K Filter, to the data. The F-K filter is commonly applied for processing seismic data in geophysical exploration, but it has not been used previously for magnetic interpretation to our knowledge. Its application for data enhancement in UXO magnetic method is a new development through this project.

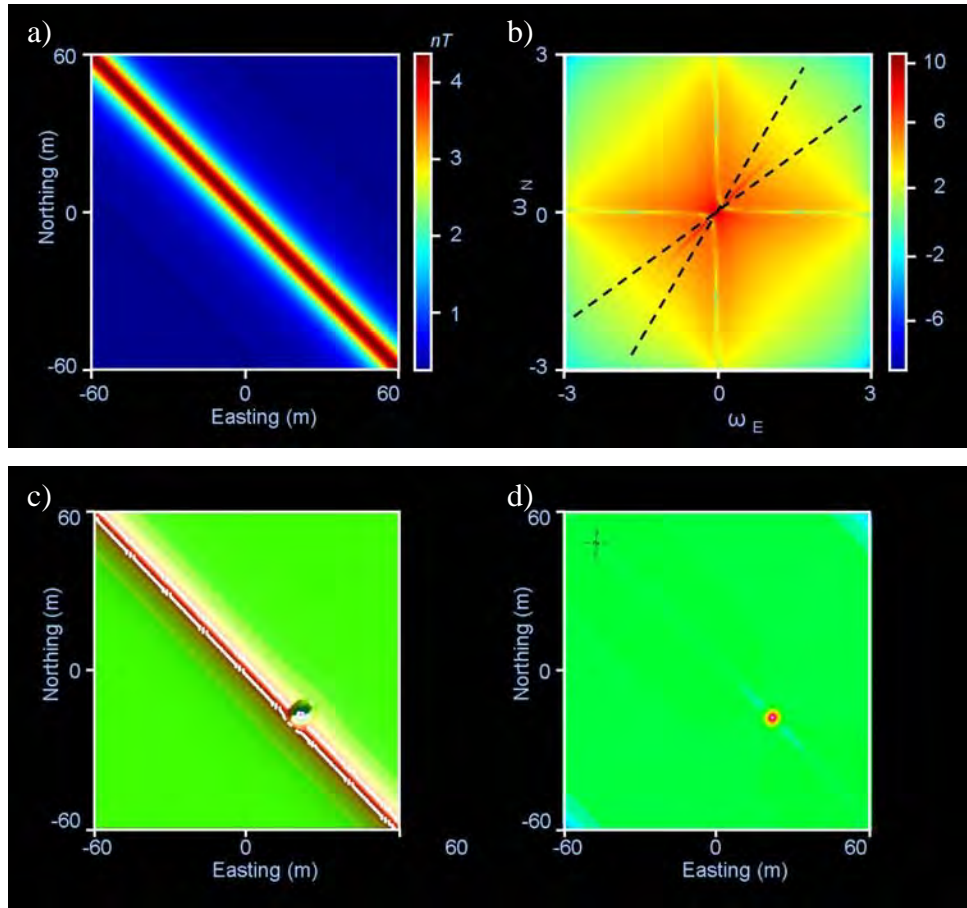


Figure 6.7: Synthetic magnetic data to illustrate application of linear feature analysis with F-K Filter. Panel (a) is a magnetic dyke with its radial power spectra in panel (b). The orientation of the magnetic ridge appears perpendicular in the frequency domain to that of the spatial domain. By tapering this feature in the Fourier to zero with an arctangent function, the magnetic ridge can be cleanly separated from the data. Panel (c) shows the same magnetic dyke with a dipole (UXO) response to be enhanced. The white lines show calculated ridge-orientations from linear feature analysis. Once the magnetic ridge has been separated, the potential UXO in panel d) is clearly enhanced.

Figure 6.7 illustrates the developed methodology, and the overall concept of linear feature analysis with FK filtering of magnetic lineaments. Any magnetic lineaments in space, such as presented in panel (a), will appear with perpendicular orientation in the frequency domain (panel b). To apply an FK Filter to the data, we taper the region in the frequency domain to zero using an arc-tangent function. Panels c) and d) illustrate enhancement of a potential UXO target embedded in a magnetic ridge using this technique. In panel c), the original magnetic data are overlain with white arrows identifying orientation of the magnetic structures using linear feature analysis. The ridge is removed with the described FK filter, and the dipole response in panel d) illustrates a clearly enhanced UXO-like anomaly for subsequent detection/discrimination analysis.

6.2.4. Regional/Residual Separation, with Total Gradient enhancement

The final method we design and implement under this project is a recursive 1D low-pass Butterworth filter of low order along the data collection lines. The method was first implemented as a component of decorrugation filtering for removing data heading errors from line to line. We have observed that the method nicely preserves the response of potential UXO while separating the larger interfering structures due to geology, large sub-surface structures, and heading errors during acquisition.

In addition to separating the potential UXO responses from strongly interfering background, we also demonstrate in this section the application of total-gradients to further enhance the response of targets of interest. We illustrate the effectiveness of these combined methods with two large datasets of current interest to the UXO community – former Camp Sibert, AL, and San Luis Obispo, CA.

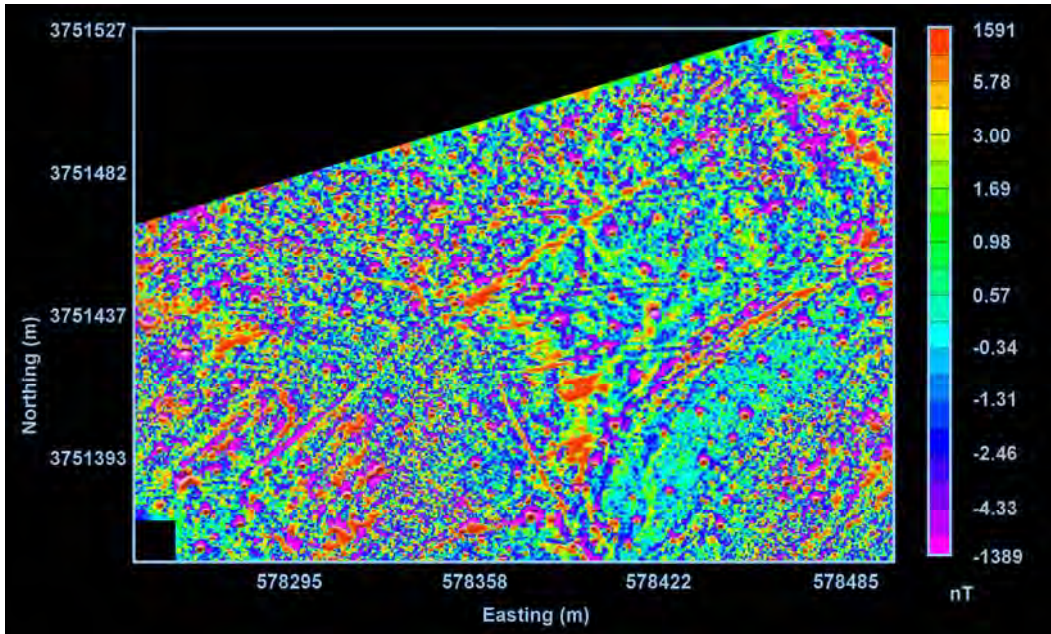


Figure 6.8: Original total-field magnetic data collected at the south-west region of former Camp Sibert, AL, for UXO clearance efforts. The larger compact anomalies around the middle of the data, as well as the elongated magnetic ridges were a source of numerous false targets as identified from the site's dig-list.

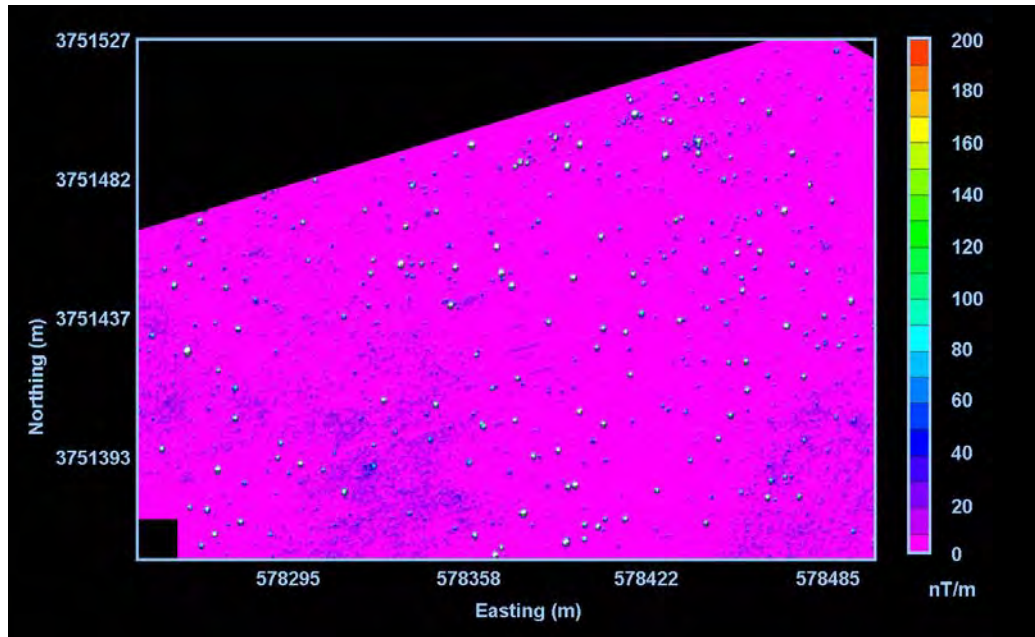


Figure 6.9: Well defined targets of interests within magnetic data from Camp Sibert, AL. The data have undergone separation of the strongly interfering background response, as well as total-gradient calculation to further enhance the potential UXO and scrap targets.

6.2.4.1. Camp Sibert, AL

For the Camp Sibert application, we use the magnetic dataset for the south-west region of the site, shown in Figure 6.8. Within the data, there are two features of interest for separation. First, there are high amplitude, compact anomalies near the central region of the grid. The second features of interest are the elongated magnetic lineaments striking north-east to south-west. Each of these magnetic features is the result of strongly interfering background and each feature generated numerous false picks for the site's dig-list. In Figure 6.9, we demonstrate the ability to successfully remove the interfering background through geologic separation. The potential UXOs are further enhanced for subsequent analyses through total gradient calculation. Each of the ‘dimples’ within the newly processed data represent potential targets of interest that would warrant continued analysis for the remediation efforts at Camp Sibert, AL.

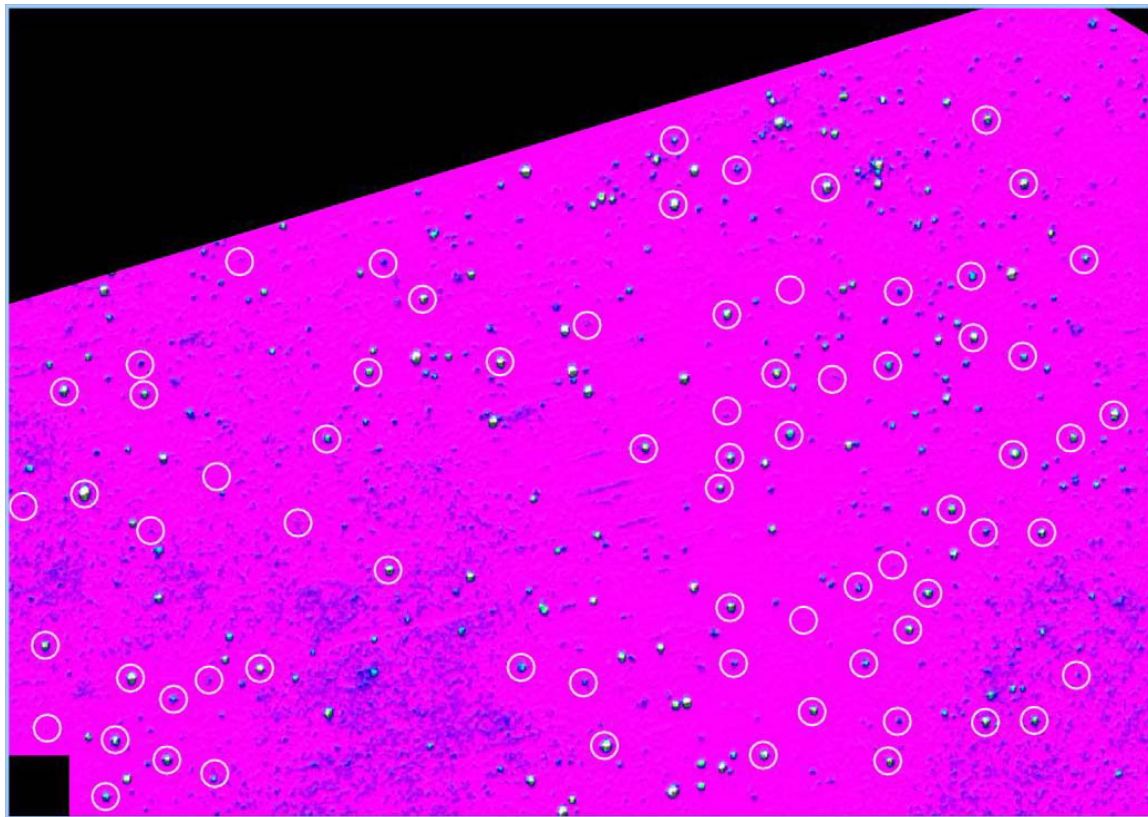


Figure 6.10: Camp Sibert. Locations of actual UXO from dig list in white circles. Geology separation clearly enhanced response of UXO targets (as well as unmarked scrap) for later analysis.

6.2.4.2. San Luis Obispo, CA

The second magnetic data in which we demonstrate geologic separation and UXO enhancement is from San Luis Obispo (SLO), CA. The original data, illustrated in Figure 6.11 (left) are contaminated with strongly interfering geology (compact and regional), underground bunkers, as well as tares in the data along grid ties. Because of the strong level of background interference and small targets of interest, the data at SLO has been widely accepted as unusable for the site's remediation efforts. We demonstrate here that proper separation of all background interference from geology/bunkers/tares, followed by total-gradient calculation for visual enhancement generates high quality data with clearly identifiable targets of interest. The original data at SLO is difficult, but as we will show, early processing and target enhancement algorithms significantly improve detectability at the site.

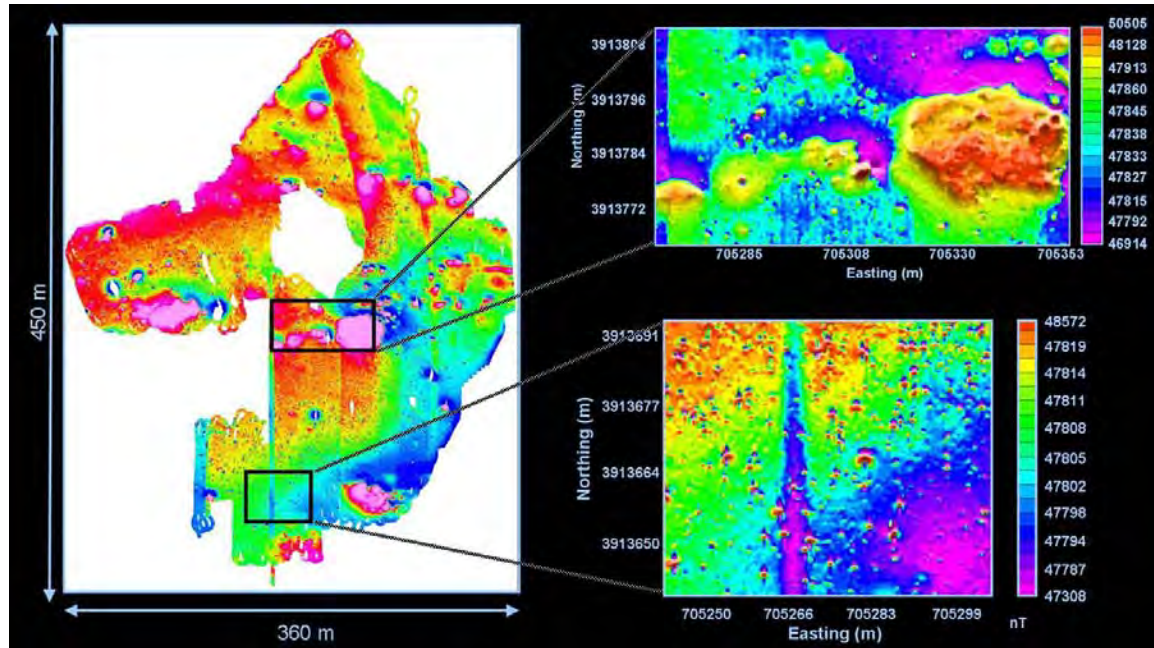


Figure 6.11: San Luis Obispo, CA, total field magnetic data. Two regions are extracted for illustrative purposes. The central data region (upper right panel) contains strong background response from geology, underground bunkers as well as small dipolar responses from UXO and scrap. The lower data region (lower right panel) demonstrates a large regional response from local geology, compact magnetic lineament trending north-south, as well as response of small UXO and scrap.

We focus here on two sub-regions within the SLO magnetic data due to the varying nature of background interference at each. The first is extracted from the central region of the site (upper right panel), and is considered the most difficult region at SLO. The data are highly contaminated with large amplitude, compact anomalies from geology and underground bunkers. The data likewise show a north-trending tare in the data from tying separate data collections together. The anomalies of interest are significantly smaller than the background interference, and previous detection efforts based on this data were unsuccessful. The difficulties of detection at this location are not a limitation of the methods employed, but merely illustrate the need to separate the strongly interfering background prior to detection/discrimination analysis. The second sub-grid (lower-right pane) illustrates a very strong regional anomaly from geology, and a high-amplitude north-south lineament within the center of the data, combined with small amplitude targets of interest. The data have a very different character from the central grid to the north, but the difficulties in detecting small UXO and scrap in such background interference remains the same.

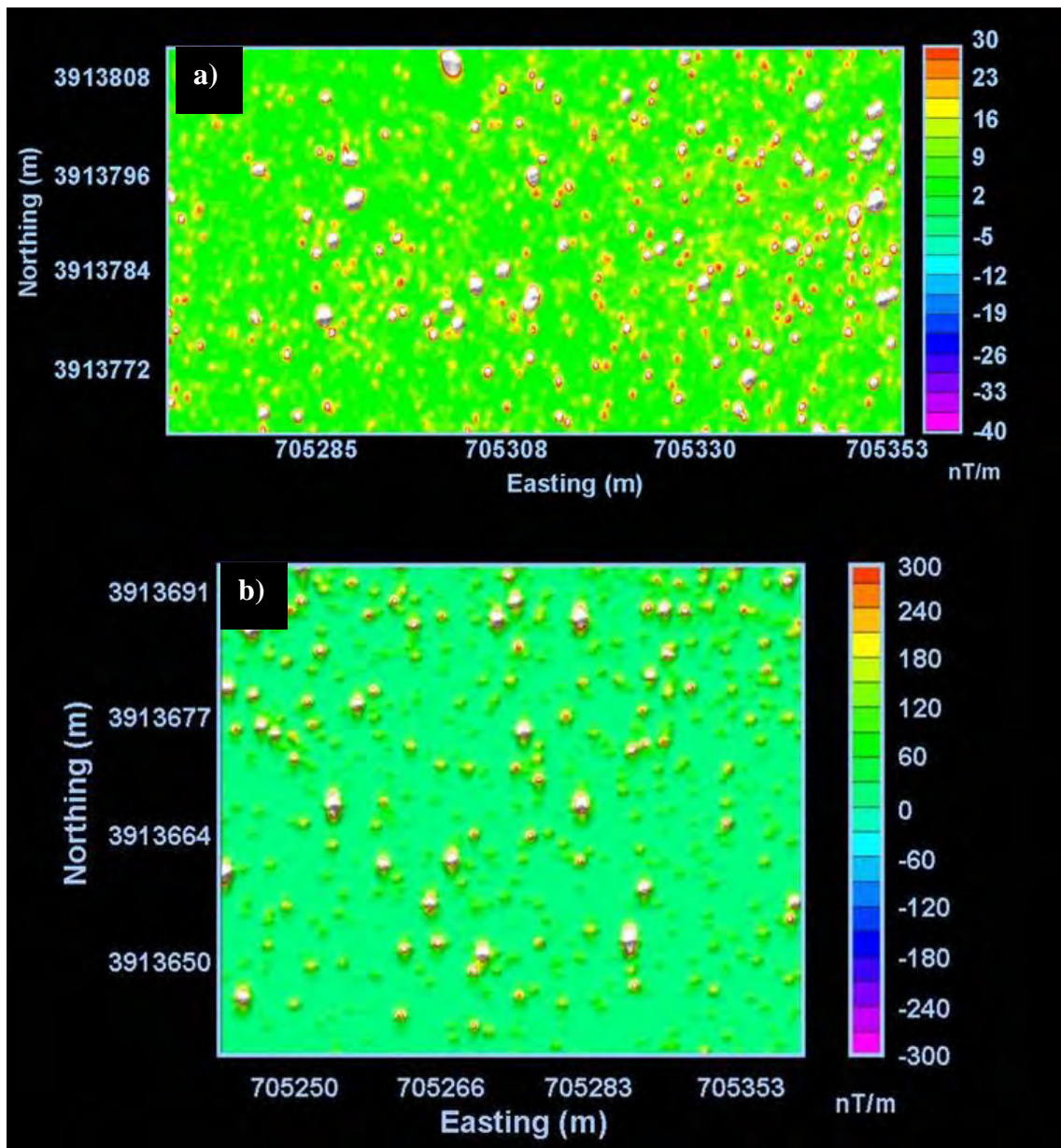


Figure 6.12: San Luis Obispo, CA, magnetic data after separating strongly interfering background and enhancing small isolated targets by total-gradient calculation. Panel a) here is processed from the central SLO dataset presented in the upper right of Figure 6.11. Panel b) here is the enhanced data from the lower region of SLO first presented in the lower right pane of Figure 6.11. Potential UXO and scrap are clearly enhanced in both magnetic data grids for subsequent detection/discrimination applications.

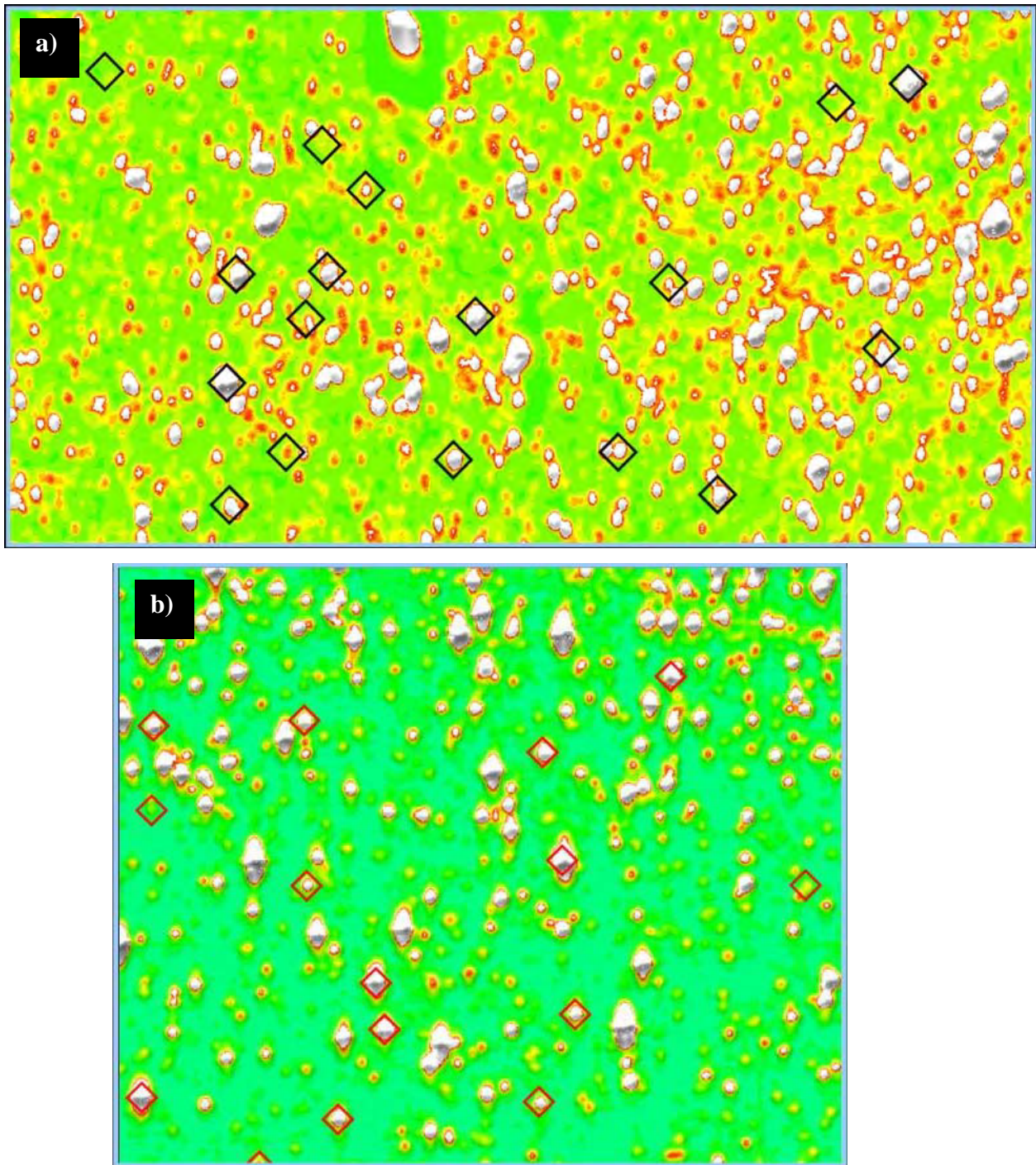


Figure 6.13: San Luis Obispo. Locations of actual UXO from dig list in black and red squares for the center site (a), and lower site (b) of SLO respectively. Geology separation clearly enhanced response of UXO targets (as well as unmarked scrap) for later analysis.

In Figure 6.12, we illustrate results from separating the response of potential UXO from interfering geology/bunkers. The data are further enhanced by total-gradient calculation, and we therefore present well defined, isolated targets of interest for later detection methods. The enhanced data are likewise presented in Figure 6.13 with locations of UXO items from the dig-list identified for reference.

The original magnetic data at SLO are clearly difficult for UXO remediation efforts upon first inspection. However, we have demonstrated here that robust algorithms appropriate for the site's remediation needs can easily manage the interfering background response, and highlight a set of well-defined targets of interest. This is true even within the most difficult magnetic region of SLO (center grid from Figure 6.11).

6.3. Summary

While magnetic method has a long standing history of successful application in UXO remediation efforts, the method routinely demonstrates poor results at sites with strongly interfering magnetic background. Because limited processing algorithms are available to the UXO community through commonly applied interpretation packages, these poor detection results have contributed to reduced application of the method as a whole. The difficulty of working with magnetics for detection in these varying magnetic environments is not a result of data limitations, as most believe, but merely a lack of early stage processing with robust algorithms to separate the background response while preserving those of UXO and scrap.

In this chapter, we have demonstrated that a suite of robust techniques are required for effective remediation efforts with magnetic method when varying magnetic interference is present at a site. We illustrated results from four methods, not commonly applied to UXO magnetic data and only applied to difficult magnetic problems, and each method demonstrates success for enhancing UXO response in difficult magnetic environments. Two of the methods (iterative Wiener filter and discrete wavelet transform) originated from SERDP Project MM-1414, and the remaining (linear feature analysis and recursive

1D decorrutation filter) show likewise valuable through the research for MR-1638. The methods have been successfully applied to enhance the magnetic data from Camp Sibert and San Luis Obispo.

We likewise state that there is no ‘one-for-all’ method to achieve the common goal of enhancing UXO response in magnetic data when moving from site to site. Rather, a collection of techniques must be available, depending on the nature of the geologic response, acquisition noise, heading errors, position accuracy, and UXO type/depth.

7. Application of automated SI detection

7.1. Background

The primary goals for Task 1 of SERDP Project MR-1638 include:

- 1) complete development of automated extended Euler deconvolution as a detection tool for UXO-type sources;
- 2) extend the method to total-field as well as gradient magnetic data;
- 3) complete the development of necessary pre- and post-processing steps associated with extended Euler solutions for recognizing false alarm due to geology;
- 4) understand the effects of filtering magnetic data on recovered Structural Index (SI) values;
- 5) implement or develop processing techniques, as needed, to separate out the response of strongly interfering geology and enhance UXO response; and
- 6) apply the automated approach to data from environments with strong magnetic geology.

The first five items have been addressed in the previous chapters of this document. We present here the results of applying the newly developed detection algorithm to UXO magnetic data (item 6) collected at Camp Sibert, AL, and at San Luis Obispo, CA.

7.2. Introduction

One of the primary goals of MR-1638 is to develop an automated detection algorithm based on structural index (SI), and test the algorithm on real magnetic datasets to validate the methodology. In the previous chapters, we presented detailed information on the detection algorithm, along with necessary pre- and post-processing analysis tools to winnow false targets associated with spray, geology, and acquisition errors. We have successfully applied the new detection technique to two remediation sites of recent

interest: Camp Sibert, AL; and San Luis Obispo, CA. In this chapter, we present results of the detection algorithm for these sites.

7.3. Detection results

Extended Euler deconvolution method has been extended from its application to total-field magnetic data, to magnetic gradient data as well. In the following field applications for Camp Sibert and San Luis Obispo, we illustrate results of the detection technique applied to gradient data calculated from the original total-field data. All detection results are then illustrated, however, with data (as presented in the previous chapter) that have undergone two specific processing steps to provide the cleanest image possible for presenting detection locations, along with UXO and other metal items from the sites' dig lists. The data presented have undergone geologic separation as a necessary first step for both sites. The separated data are then processed a second time through total-gradient calculation to further enhance the isolated anomalies now visible for all potential UXO targets. For better presentation of the enhanced data without the overmarkings of detection solutions, the reader is referred to Chapter 6 of this report.

7.3.1. Camp Sibert, AL

The first site is the south-west grid of the former Camp Sibert in Alabama. The original total field magnetic data provided are illustrated in Figure 7.1. The data are first processed to separate the geologic background known to have generated false picks within the original dig list. In particular, numerous false targets were dug within the three high-amplitude magnetic anomalies near the center of the grid in Figure 7.1, as well as along the north-east to south-west striking magnetic lineaments apparent in the data. Dig results listed no metal items at many of the locations originally picked within these magnetic regimes. For application of extended Euler detection, following geologic separation, we then calculate the vertical gradient (VG) using Hilbert transform and apply the detection method to this VG data.

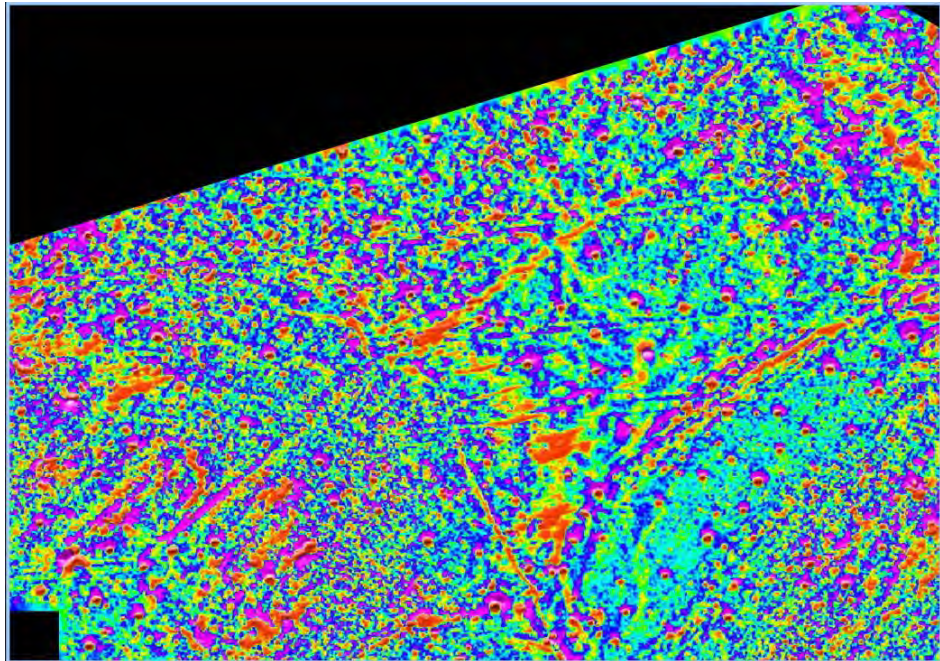


Figure 7.1: Original magnetic data for south-west grid of former Camp Sibert site. The data are processed to separate the strongly interfering magnetic geology, and processed to VG data for application of extended Euler deconvolution detection technique.

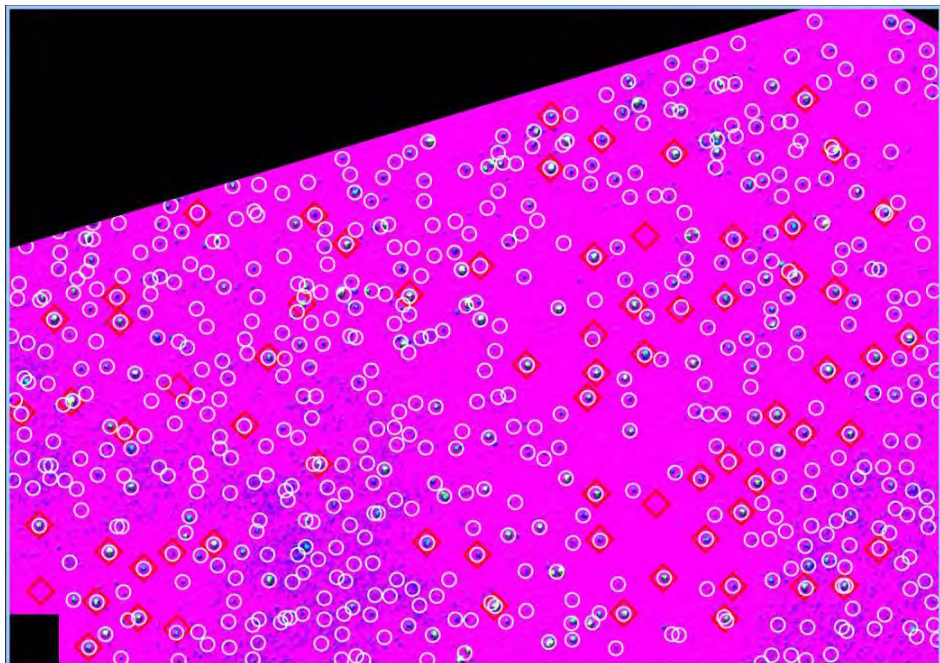


Figure 7.2: Detection results at Camp Sibert. For illustrate purposes, the background data are total-gradient data (TG) following separation of interfering geology. The white circles were selected as potential targets for subsequent analysis based on structural index. The red squares are known UXO from the site's dig list. 68 of the 71 known UXO were identified as targets based on extended Euler deconvolution.

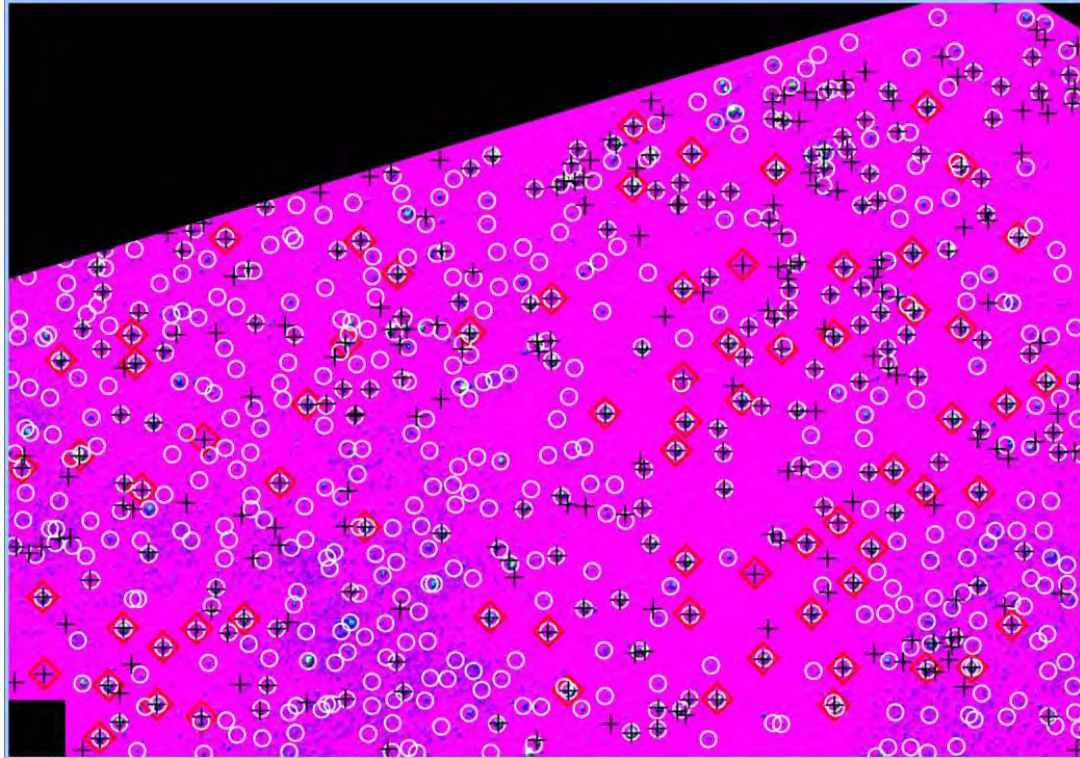


Figure 7.3: Detection results versus all metal targets at Camp Sibert. The white circles were selected as potential targets for subsequent analysis based on structural index. The red squares are known UXO from the site’s dig list. The black plus-marks are metal identified from the dig list. Based on structural index, extended Euler deconvolution identified most of the metal targets, with the remaining picks likely the response of metal targets that were not on the dig list due to small amplitude EM response. Following separation of interfering magnetic background, extended Euler deconvolution has performed well at Camp Sibert.

Detection results for Camp Sibert are illustrated in Figure 7.2. Within the figure, the red squares identify the known locations of UXO for the site’s dig list. There are 71 UXO within this region of Camp Sibert. The white circles in Figure 7.2 mark the locations of potential UXO based on extended Euler deconvolution following clustering and amplitude analysis. The detection algorithm has identified 68 of the 71 UXO at the site in this case. We next illustrate the methods overall performance with metal targets in general. Figure 7.3 identifies the locations of all metal targets buried at the site (UXO in red squares, and scrap with black plus-marks) along with detection results (white circles).

The method has clearly identified the majority of all metallic targets (UXO and scrap) within the south-west grid of Camp Sibert. The remaining targets identified based on structural index are likely metallic sources that behave as magnetic dipoles, but were not placed on the original dig list based on amplitude cutoff within the EM response. Fine-tuning the amplitude threshold for magnetic detection with extended Euler deconvolution could likewise be adjusted based on knowledge of the site combined with predicted ordnance size and maximum depth. Such information was not utilized for the results presented in Figures 7.2 and 7.3 for Camp Sibert.

7.3.2. San Luis Obispo, CA

The second site we apply our SI-based detection algorithm to is San Luis Obispo (SLO) in California. The original data are presented in Figure 7.4. MM-1638 has the specific focus of working with difficult magnetic data; therefore, we illustrate application of extended Euler deconvolution to a region of the SLO data identified with the most difficult background interference. This sub-grid is near the center of the SLO site, and it contains the strongest interfering response with a large areal extent due to an underground bunker, several moderate magnetic hills, as well as a north striking magnetic tare in the data to the west. Due to the small targets of interest at the site, detection at this location of SLO proves difficult without removing the background interference.

The reader is referred to the previous chapter for the cleanest images of the processed data without overlying detection results. Detection results for the sub-grid of SLO are presented here in Figure 7.5. Within the figure, the red squares identify the known locations of UXO for the site's dig list. There are 17 UXO within this region of SLO. The white circles in Figure 7.5 mark the locations of potential UXO based on extended Euler deconvolution following clustering and amplitude analysis. The detection algorithm has identified 14 of the 17 UXO at the site in this case. Figure 7.5 likewise identifies the locations of all metal targets buried at the site (UXO in red squares, and scrap with black plus-marks) along with detection results (white circles). The method has

identified most of the metallic targets (UXO and scrap) in general within this section of SLO.

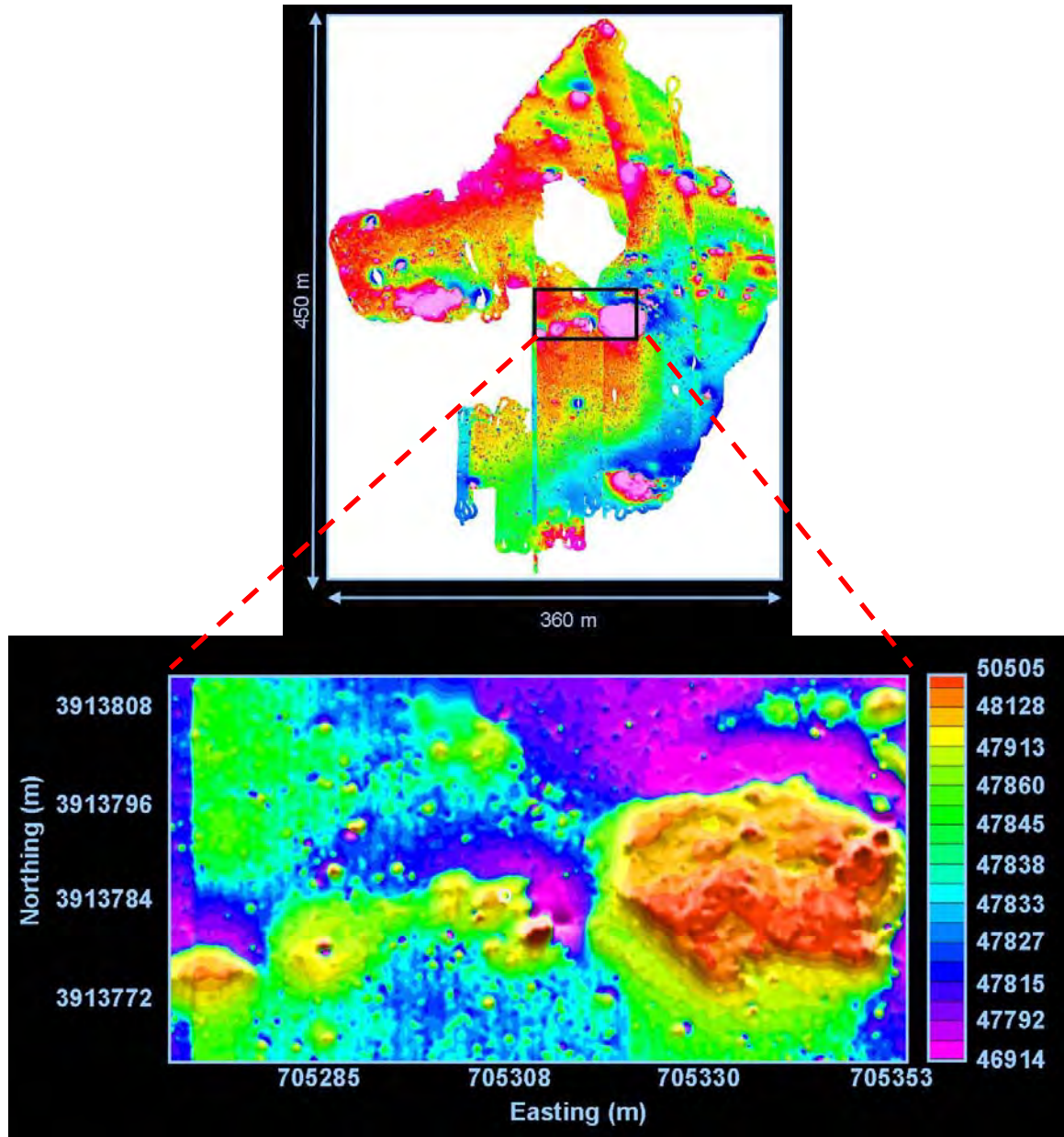


Figure 7.4: San Luis Obispo (SLO), CA. Magnetic data over the entire site, and the sub-grid selected for detection demonstration. The sub-grid was selected to be the most difficult magnetic region with SLO. The large, high amplitude anomaly is the response of an underground bunker. There are other compact anomalies interfering with the targets of interest as well as a north striking magnetic tare in the western region of the data.

While the data in Figure 6.13 (previous chapter for enhancing UXO response in magnetic environments) clearly amplifies the majority of metal targets at the site, the clustering algorithm here specific to our detection methodology undesirably reduces the number of metal targets identified at the east end of the SLO sub-grid – where there is an increase in metal clutter. This is a component of the developed methodology that must be adjusted based on site information, and would largely improve with the experience that remediation teams naturally acquire over time. As with the Camp Sibert site, the remaining targets identified at SLO based on structural index are likely metallic sources that behave as magnetic dipoles, but were not placed on the original dig list based on amplitude cutoff within the EM response. Fine-tuning the amplitude threshold for magnetic detection with extended Euler deconvolution could likewise be adjusted based on knowledge of the site combined with predicted ordnance size and maximum depth. Such background information was not utilized for our detection results at SLO.

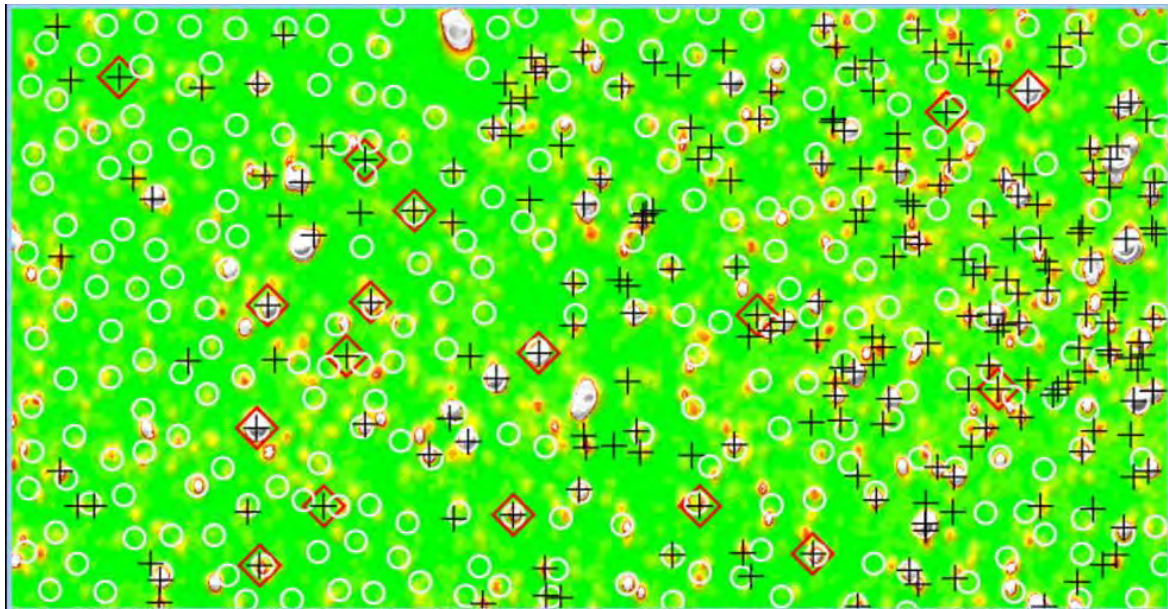


Figure 7.5: San Luis Obispo (SLO), CA. Detection results overlying total-gradient data that has first undergone separation of background interference. The white circles were selected as potential targets for subsequent analysis based on structural index. The red squares are known UXO from the site's dig list. The black plus-marks are metal identified from the dig list. Based on structural index, extended Euler deconvolution identified most of the metal targets, with the remaining picks likely the response of metal targets that were not on the dig list due to small amplitude EM response.

7.4. Summary

In this chapter we demonstrated the application of structural index (SI) based detection of potential UXO targets using magnetic data in remediation efforts. The targets selected by the approach are assumed the response of compact metal sources, such as UXO and scrap, which behave primarily as magnetic dipoles with SI of 3. Incorporated into the detection algorithm is a series of post-processing algorithms that first cluster the skewed solutions from numerical spray, and second, that eliminate many false targets (such as acquisition noise) based on amplitude analysis.

The method has performed well on two very difficult magnetic data sets, one from Camp Sibert and the other from San Luis Obispo (SLO). Due to strong site-specific magnetic interference (such as from geology), the approach requires at these sites that the data first be ‘cleaned’ by separating the interfering background and enhancing the responses of potential UXO. Extended Euler deconvolution successfully identifies all dipole sources within the grids, including UXO and scrap. However, it is apparent from our results that the biggest weakness of the approach, as with any detection technique, is the subjective components of picking amplitude thresholds, as well as clustering style and radii. These components are essential to significantly winnow the number of false targets. But these parameters are also site specific information, and they are best estimated by an experienced remediation team that routinely applies the technique from site to site. This is not an issue that is unique to the SI based detection method developed through MR-1638, but it is common to all detection methodologies developed for both magnetics and EM in UXO remediation.

8. Recovery of multipole magnetic moments for discrimination

8.1. Background

SERDP Project MR-1638 had three overall research focus areas: (1) separation of interfering background and enhancing UXO response in difficult magnetic environments; (2) detection of potential UXO with extended Euler deconvolution based on structural index; and (3) recovering higher-order magnetic moments as a means of measuring target asymmetry for discrimination using magnetic data. In the previous chapters of this report, we provided details and field examples for the components related to items one and two above. In this chapter, we present results over the life of the project towards discrimination with multipole magnetic moments.

8.2. Introduction

It is well known that meaningful information on a target's asymmetric distribution of magnetization is not contained in the magnetic dipole moment. This shape information is only contained in the higher order moments, the quadrupole and octupole. Currently, however, the dipole moment, which dominates the response of isolated metallic sources is the only moment utilized during remediation efforts in an attempt to discriminate between UXO and scrap. For magnetics to advance beyond detection into a meaningful tool for discrimination, recovery of the higher order moments would be necessity.

The primary goal of the remaining focus area for SERDP Project MR-1638 was to advance discrimination between UXO and scrap in magnetics based on asymmetry information contained within the higher-order magnetic moments. The first and most significant component was therefore recovery of the multipole moments through inversion. In this chapter we present our results on recovering these moments through various inversion algorithms, as well as one's likelihood of recovering true discrimination parameters based on shape from magnetic data.

8.3. Multipole magnetic moments

Magnetic dipoles and spheroids have been the fundamental models for UXO discrimination using magnetometry (McFee, 1989; Altshuler, 1996; Butler *et al.*, 1998; Billings *et al.*, 2002). Applicability of dipole methods has been largely justified by the magnetic response of a buried metallic object being dominated by a dipolar field. The dipole moment summarizes the total intensity of magnetization within an object but carries no direct shape information. This lack of information about size, orientation, and asymmetry of the body, has hampered a more successful discrimination effort. As a result, current dipole-based discrimination methods (Billings, 2004) rely upon the direction of magnetization that might be altered by physical processes such as shock demagnetization and remanent magnetization. So far, there has been little work in the literature that makes direct use of the geometry of buried metallic objects. Part of the reason for this state of affairs is the belief that only the dipole moment can be recovered from field data, whereas the discrimination based on shape requires higher-order moments. Part of this reason is also related to the current paradigm of looking only for UXO to dig up among all anomalies.

The variability and asymmetry of magnetization increase dramatically within irregularly shaped fragments. As a result, these items tend to possess significant high-order moments. Although the presence of stronger higher-order moments in irregular bodies is well recognized in classical physics, little work that quantifies the strengths and contributions of these moments is available in the UXO literature. Furthermore, there has been little effort in making use of these higher moments as a means for discrimination. This is partly due to limitations imposed by the noise level in the total-field magnetic anomalies acquired in UXO clearance. As we see advances in magnetic systems with increasing signal-to-noise-ratio (SNR), these data could potentially make it feasible to recover higher-order moments, and raise the possibility of their use in UXO discrimination. Furthermore, an alternative paradigm for UXO discrimination is to specifically recognize scrap metals that should be left in the ground. Recovering higher-

order moments to discriminate irregularly shaped fragments has the theoretical potential to offer an effective tool to the new paradigm.

The differences between dipole and higher-order moments are highlighted by their respective relationships with the magnetization distribution within a magnetized object,

$$\text{Dipole: } m_i^{(1)} = \iiint_V M_i dv \quad (8.1)$$

$$\text{Quadrupole: } m_{ij}^{(2)} = \iiint_V (M_i x_j + M_j x_i) dv \quad (8.2)$$

$$\text{Octupole: } m_{ijk}^{(3)} = \iiint_V (M_i x_j x_k + M_j x_i x_k + M_k x_i x_j) dv \quad (8.3)$$

where i , j , and k represent respectively one of the three axis directions. It is clear that the dipole depends only on the total volume of the object, irrespective of the shape of the body, whereas the quadrupole and octupole moments contain information about the asymmetry of magnetization since they are a function of distance-weighted moments of magnetization.

We have carried out significant research on understanding the magnitude of multipoles in various UXO and non-UXO objects and demonstrated that there is enough information to recover higher-order moments using high-quality total-field magnetic data and magnetic gradient tensor data. Sinex *et al.* (2005) and Sinex (2006) have shown that, even with current production data, there may be usable information remaining in the residual after a dipole fitting. Furthermore, Sanchez *et al.* (2006) have shown in the work carried out within MM-1328 that buried non-UXO with irregular shapes have consistently higher ratios of the quadrupole and octupole fields to dipole field compared to UXO with regular shapes. In addition, this ratio is significantly higher than the expected SNR of tensor data and some total-field data.

Thus, high-quality total-field magnetic data and tensor gradient magnetic data that have become available might enable us to recover higher magnetic moments. These higher moments encode direct information about the shape of buried metallic objects (Jackson,

1999; Altshuler, 1996; and Billings, 2004) and therefore provide an alternative, and perhaps more direct, criterion for discrimination. Thus, this component of MM-1638 was created to explore this avenue, focusing on extraction of magnetic higher-order moments as a new means of UXO/scrap discrimination.

8.4. Inversion for multipole moments

The basis for the recovery of meaningful source parameters is to be able to create a model that adequately predicts the measured field. We use multiple expansions as a means to concisely represent the magnetization distribution in buried targets. There are a number of expansions in different coordinate systems, and we consider here a Taylor series expansion in Cartesian coordinates (McFee and Das, 1990).

The Taylor series expansion has been used by Sanchez *et al.* (2006) extensively to model the magnetization distribution of three-dimensional objects. It has been found that, with current data quality, the octupole is the highest moment that may be theoretically recoverable. Hence, the multipole expansion is carried out only through the octupole. The magnetic potential is given by,

$$\varphi(\vec{r}) = \frac{\mu_o}{4\pi} \left[m_i^{(1)} \frac{\partial}{\partial x_i} - m_{ij}^{(2)} \frac{\partial^2}{\partial x_i \partial x_j} + m_{ijk}^{(3)} \frac{\partial^3}{\partial x_i \partial x_j \partial x_k} \right] \left(\frac{1}{r} \right) \quad (8.4)$$

where $m_i^{(1)}$, $m_{ij}^{(2)}$, and $m_{ijk}^{(3)}$ are respectively the dipole, quadrupole, and octupole moment. The magnetic flux intensity is given by the negative gradient of the potential (Blakeley, 1996). There is redundancy in the higher order moments and only a subset of the components in the moment tensors is independent. The quadrupole moment, for instance, has only five independent components. Similarly, octupole has only seven independent components out of the 27.

We have expended significant effort over the life of the project in developing robust algorithms that will recover the location, dipole, and quadrupole moments of a source

from either total-field data or gradient data. We have developed the component for modeling both total-field and gradient anomaly using multipole moments. A large amount of simulations have been carried out to understand the coupling among the position and the magnetic moments. In this section, we briefly describe solution strategies developed for recovering the magnetic moments through inversion. In the sections following, we present inversion results and recovered asymmetry parameters for UXO and scrap based on simulations (Section 8.5.) and real target (Section 8.6).

8.4.1. Model parameters

In this section, we present two realistic targets of UXO and scrap for discrimination testing based their higher-order moments and asymmetry parameter. Inversion results for these are presented in section (8.5). The models are presented here in Figure 8.1.

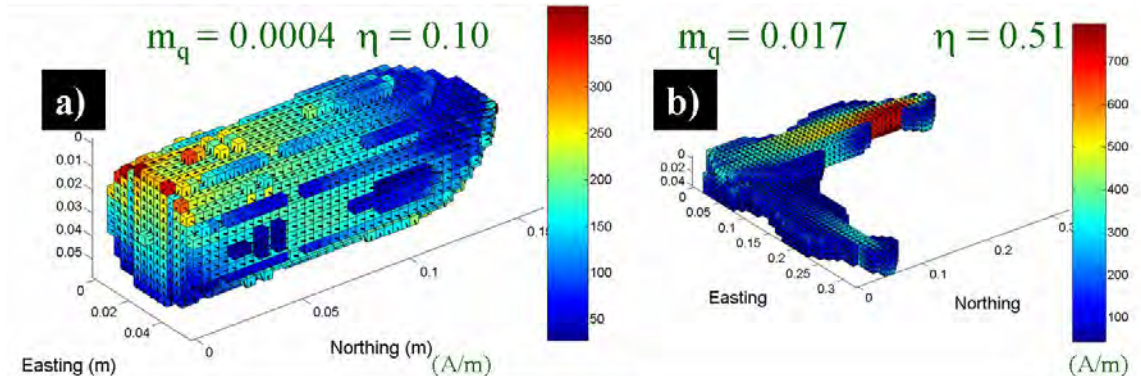


Figure 8.1: Simulated UXO and scrap for testing discrimination algorithms. a) is an image of magnetization distribution for a 57mm UXO, and b) is asymmetric scrap metal. The quadrupole moment (m_q) is an order of magnitude higher for scrap as expected for asymmetric targets. Similarly, the asymmetry parameter (η from Eq. 8.5) is approximately five times larger for the scrap target than the UXO.

From these targets, data are generated to contain both dipole and quadrupole moments. A sample dataset, Figure 8.2, is illustrated for the scrap target and it represents the data to be inverted for recovering position (3 parameters), dipole moment (3 parameters), and quadrupole moment (5 independent parameters).

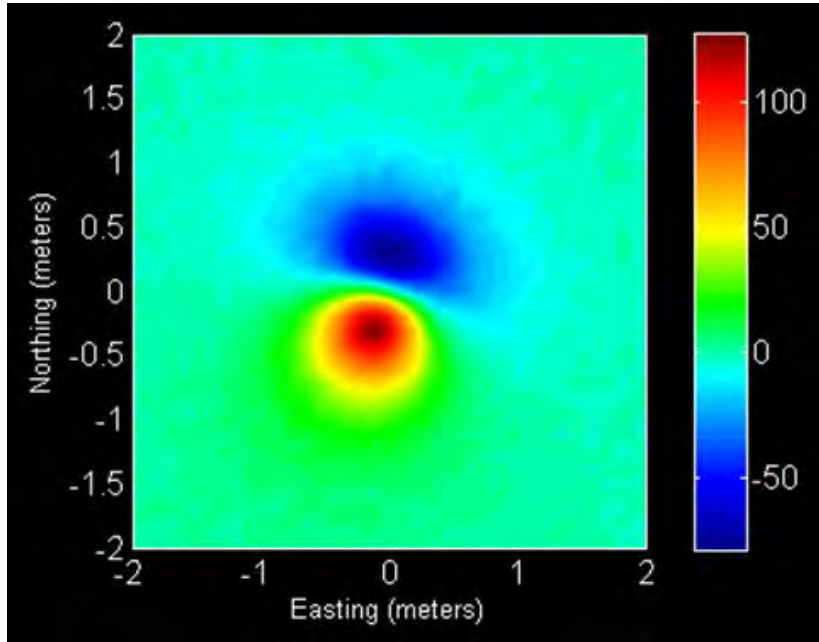


Figure 8.2: Data for simulated scrap illustrated in Figure 8.1(b). The data contain both the dipole and quadrupole responses. Inversion results for this dataset are presented in section 8.5.

While the multipole moments contain a measure of target symmetry, this valuable information must be extracted in some useful form from the inversion results for use as a discrimination tool. One approach is to calculate, from the recovered moments, a measure of target shape known as its ‘asymmetry parameter’:

$$\eta = \frac{(V_y - V_z)}{V_x}. \quad (8.5)$$

In equation (8.5), the asymmetry parameter, η , is borrowed from nuclear magnetism (Abragam, 1961). It is a parameter that describes a measure of the asymmetry between the two minor principal component vectors of the traceless quadrupole tensor, or the

fraction of the largest that their difference makes up. In equation (8.5), the principal component vectors have the convention:

$$V_x \geq V_y \geq V_z . \quad (8.6)$$

As provided in Figure 8.1, the asymmetry parameter for our simulated 57mm UXO is 0.10, and that of scrap is 0.51. The parameter is approximately five times larger for the scrap, which is predicted for asymmetric targets with a resulting increase in magnetic quadrupole moment. This asymmetry parameter is a useful measure of target symmetry and therefore provides a direct means of discrimination between UXO and scrap with magnetic data.

In the following section (8.4.2), we briefly describe the optimization algorithms developed for recovering the position and multipole moments of UXO and scrap targets. We then present in section (8.5) results from inversion for multipole moments and calculation of the associated asymmetry parameters for discrimination purposes.

8.4.2. Developed inversion algorithms

Early inversion results indicated that there is a strong tradeoff between the recovered position, the dipole moments, and quadrupole moments for the parametric inverse problem we face here. As a result, the data misfit function is likely characterized by a long flat valley with potential local minima, which can represent different classes of solution. Understanding the nature of this solution space (numbers, widths, and depths of these local minima) is therefore essential for reliably recovering the higher order magnetic moments as foundation for discrimination. The standard Gauss-Newton minimization technique developed and implemented as our first pass inversion approach for multipole-moments did not perform well in this case. The performance of Gauss-Newton, in essence, is related to use of a guided downhill (local) search algorithm; however, the complexity of the solution space requires a more global perspective.

To overcome this difficulty, we investigated the feasibility of using various additional optimization techniques, such as Genetic Algorithm (GA) and Simulated Annealing (SA), as alternative approaches for robust parametric inversion for higher-order moments. In total, we have developed and tested four separate optimization algorithms over the project life to identify an optimization algorithm, or algorithms, appropriate to the shape of the solution space here. These include:

1. Gauss-Newton local search guided by derivative information
2. Recursive Quenched Simulated Annealing (QSA) local search by controlled random perturbation
3. Genetic Algorithm (GA) global search based on biological evolution
4. Memetic algorithm for fast global search by hybridizing GA and QSA to create evolutionary leaps in a genetic population

GA is a minimization method that mimics the natural evolution of a biologic system and finds the best fitting model from an evolving population. It allows us to both invert for a single model of the parameter set as well as to explore a range of similar models. The latter can potentially provide statistical information about the target and aid in discrimination. Recursive QSA, similar to GA, starts with a large population of random solutions within an initial parameter set. The solutions are then perturbed randomly, yet independently (unlike GA), within parameter bounds to trap each of the final solutions within their separate neighborhood minima – whether they are local or the global. The solution spread provides direct information on the complexity of the data-misfit function, as well as identification of the global minima that we seek. Finally, the memetic algorithm is a hybrid optimization technique that blends the GA population for global search with downhill search by QSA. The result is an evolving population of solutions with efficiency significantly improved over stand-alone GA.

The algorithms described above each have different strengths and weaknesses for mapping the structure of the solution space and they were each investigated for this

problem. While there are many solutions that can be presented for each of the optimization techniques developed over the past year, for brevity we limit our results here to a single method that most reliably recovers the eleven parameters necessary for discrimination between scrap and UXO. We have identified that the recursive QSA approach has provided significant insight into the complexity of the objective function at hand, while finding a global-minimum that appropriately represents the ‘best’ solution. We present next (section 8.5.) the results of inversion for position, dipole, quadrupole moments and subsequent calculation of asymmetry parameter for the simulated UXO and scrap targets in Figure 8.1. In section 8.6 we present results for real targets.

8.5. Results for Simulated UXO / Scrap

We present in here the results of inversion for position, dipole- and quadrupole-moments for the simulated UXO and scrap items illustrated in Figure 8.1. In addition, we calculate the associated asymmetry parameters (8.5) as these are a representation of target shape and therefore a natural tool for discrimination.

Using recursive QSA discussed in the previous section, we perform six-thousand uncorrelated inversions for each of the two items (57 mm UXO and scrap) in Figure 8.1. The large number of inversions is not required, nor desired, in practice. However, to understand the complexity of the inverse problem we face here, it is appropriate for early development. The approach has successfully identified the complex nature of the solution space as well as the global minimum that we seek for our problem. This is illustrated in Figure 8.3 with a summary of the multiple inversions performed for the asymmetric scrap target.

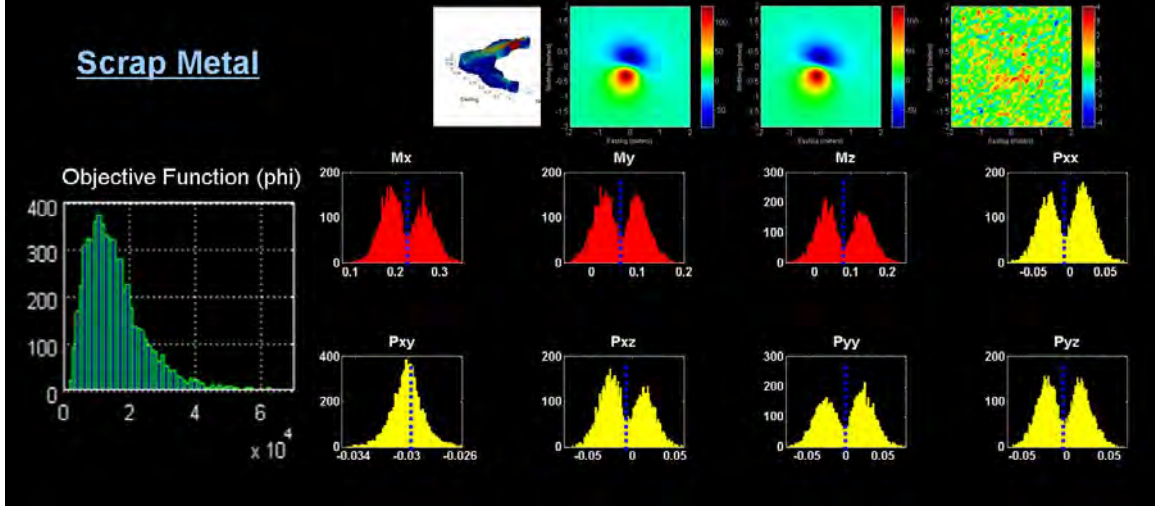


Figure 8.3: Summary of 6000 random inversions using QSA for magnetic data generated from the scrap model. The true values for the magnetic moments are identified with blue dashed lines. The global minimum would likely be unrealized by traditional inversion approaches, but the recursive QSA methodology performs well for this inverse problem. Results highlight the difficulty of finding the desired solution, and approximately 10% of the solutions achieve the global minimum in this instance.

A summary of inversion results for the simulated scrap and 57-mm UXO are presented in Table 8.1. For the symmetric UXO, the magnitude of the true asymmetry parameter is small, 0.1018. The recovered parameter is a good approximation for this target at 0.085. Next, with the less symmetric scrap item, the true asymmetry parameter, 0.514, is approximately 5 times larger than that of the UXO target. The recovered measure of asymmetry for scrap, 0.345, is consistently 4-to-5 times larger than that recovered for the UXO target.

Table 8.1: Inversion results for dipole and quadrupole parameters for UXO and scrap.

57 mm	Asym .Par	x (m)	y (m)	z (m)	Mx	My	Mz	Pxx	Pxy	Pxz	Pyy	Pyz
True	0.1018	0.0	0.0	0.3	0.0439	0.0057	0.0292	-5.9e-4	-6.5e-5	-3.3e-4	-7e-9	3.3e-9
Rec	0.0853	-0.02	0.003	0.31	0.0405	0.0069	0.0299	1.9e-3	2.5e-5	-1.0e-3	9.98e-7	-9.97e-7
Scrap	Asym .Par	x (m)	y (m)	z (m)	Mx	My	Mz	Pxx	Pxy	Pxz	Pyy	Pyz
True	0.514	0.0	0.0	0.6	0.225	0.063	0.081	-0.0076	-2.9e-2	-5.5e-3	-3.3e-3	-4.1e-3
Rec	0.345	0.0	0.0	0.6	0.227	0.062	0.087	-0.0108	-3.0e-2	-6.9e-3	-5.8e-3	-4.1e-3

The algorithm has recovered higher-order moments well-enough to identify sharp differences in the targets' asymmetry parameters, and therefore has provided us with a basic tool for discriminating UXO from scrap using magnetic data for the most realistic synthetic UXO/scrap models to date. As the higher order moments (beyond the dipole moment) are the only component within magnetic data known to contain information on source asymmetry, recovering the moments and identifying asymmetry parameters consistent with scrap and UXO is a major accomplishment for this component of MR-1638. We have demonstrated that it is theoretically possible to recover higher-order magnetic moments for discrimination in UXO application. In the next section, we focus our attention to moving beyond synthetic modeling, and examining the likelihood of recovering these same diagnostic parameters from field data for practical UXO application.

8.6. Results for Real UXO / Scrap

MR-1638 is a collaborative project between Colorado School of Mines (CSM) and Sky Research, Inc. To validate the approach of recovering higher-order moments from magnetic data in UXO application, Sky designed and built test-stand experiments for recovering high-quality magnetic data with minimal noise and tight data-spacing over various UXO and scrap targets. In addition, Sky likewise performed high-quality dynamic data collections for follow-up analysis under more field-like conditions with a moving platform. The goals for these experiments are two-fold. First, we need to identify whether the methods developed in the previous sections for synthetic targets will translate to a working discrimination technology for high-quality real data. If the technique can be successfully applied to the high-quality densely-spaced test-stand data, then the second goal is to identify whether it can be likewise applied to moving platform data, as implemented for practical remediation projects. In this section, we briefly describe the high-quality platform and dynamic data experiments, data processing, and the likelihood of recovering diagnostic UXO/scrap parameters from magnetic data in practice.

8.6.1. Data Collection Platforms

There were two types of measurements collected for this component of MR-1638:

- (1) Static (test stand) style measurements where we collect the data statically at a number of different locations. For this, we use a boom with 8 magnetometers placed on two parallel beams. The beams are notched with cuts every 5 and 10 cm intervals so the boom can be precisely positioned. Figure 8.4 illustrates design of the teststand, and Figure 8.5 contains photos of the system during construction. Data are collected by stacking measurements for 10 seconds at each location as the boom is moved 10 cm at a time. Ideally, the system would contain a two-dimensional array of sensors for simultaneous collection, similar to next-generation TEM platforms, only with magnetic sensors. The design here is still the closest magnetics equivalent to the cued interrogation platforms for TEM analysis of UXO/scrap targets. This experiment has provided the highest quality magnetic data (position and sensor accuracy) of the two measurement systems we implement here, and possibly the highest quality magnetic data over UXO/scrap for algorithmic development and testing in general.
- (2) Dynamic measurements where 8 magnetometers are positioned on a cart, which is precisely positioned using the Novatel SPAN. Data are collected over the same items as the test-stand. The data here are less accurate than the static measurements in the first experiment due to motion, but are significantly better than field data collected during remediation surveys. Figure 8.6 is a photo of the dynamic system during development.

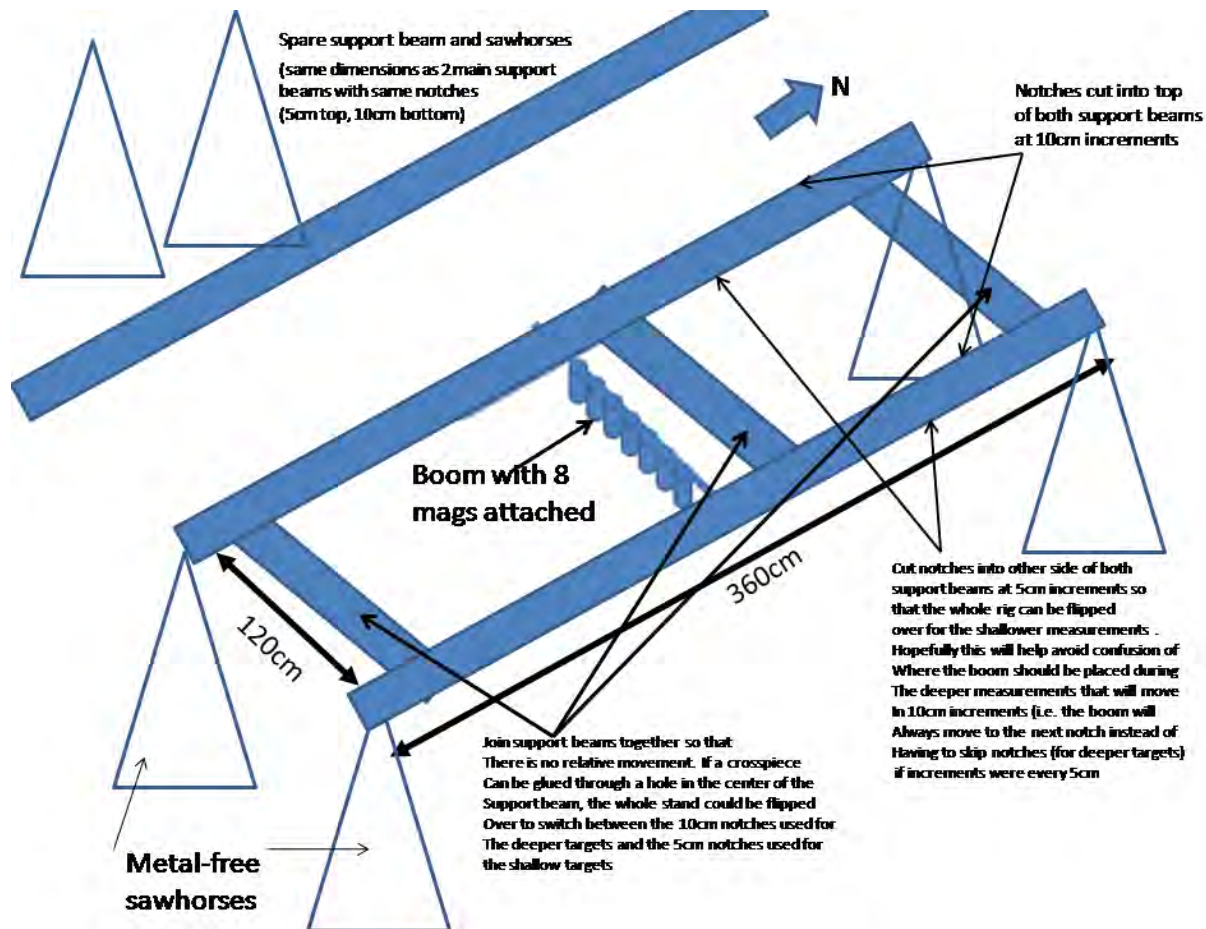


Figure 8.4: Design of the magnetic test stand for collecting high quality data to recover multipole moments from UXO and scrap items.



Figure 8.5: Test stand under construction to accommodate eight sensors with close separation that can be moved either 5cm or 10cm using a notched platform for the sliding sensor boom.



Figure 8.6: Moving magnetic platform for dynamic measurements. There are eight closely spaced magnetometers, and the IMU and Novatel SPAN to get position accuracies on the order of 1 cm and orientations to better than 0.25 degrees.

Additional Considerations:

-For both surveys we used a 9th stationary magnetometer positioned in an area free of magnetic noise to measure any diurnal changes in the Earth's magnetic field.

-For the items, one each of a 37 mm, 60 mm, 81 mm, 105 mm and 155 mm sized ordnance and roughly the same number of scrap items, we collected data in three orientations (vertical, horizontal, 45 degree) at 2 stand-off distances (two times length and four times length of the object away).

-It is important that the relative positions do not change from day to day of test stand surveying. Notches cut into the support beams ensured that a consistent 10cm sampling was achieved. During setup of each survey day, a plumb bob was used to ensure that the support beams were placed such that when the boom was in the middle survey notch on both support beams, it was directly over the target location.

-For teststand measurements, data were collected at the start and end of each day with no target present. The same height was used for start and end of day tests for all survey days.

8.6.2. Static Measurements

The base station is configured so that it records all the information needed to make atmospheric corrections during the survey. On the rover, we store the raw GPS and IMU data, not just the estimated positions as we would when running in real-time mode. The test stand is oriented to align with magnetic north. Measurements are made at three orientations for each target:

1. Aligned with the Earth's field (66 degrees dip downward pointing to the north)
2. Perpendicular to the Earth's field (24 degrees dip upwards pointing to the north)
3. 45 degrees to Earth's field (21 degrees dip downwards pointing to the north)

Magnetometer sensors are attached to the boom with a 15cm sensor separation. The boom moves across parallel support beams in increments of 10cm along the support beams. At each boom position, 10-seconds of data are collected. We have designed a wood mount to hold targets vertical, horizontal and at 45 degrees the experiments. See Table 8.2 for a summary of targets and measurements.

Table 8.2: UXO and scrap orientations and depths for static platform data measurements. The first measure, static_1, provides the background response to be removed.

XYZ File	target	depth	dip (down +ve)
static_1	empty cell	NA	NA
static_2	155mm	45	66
static_3	155mm	45	21
static_4	155mm	50	-24
static_5	105mm	45	66
static_6	105mm	42	21
static_7	105mm	42	-24
static_8	81mm	42	66
static_9	81mm	42	21
static_10	81mm	42	-24
static_11	Frag5	32	66
static_12	Frag5	35	21
static_13	Frag5	35	-24
static_14	Frag4	35	66
static_15	Frag4	35	21
static_16	Frag4	33	-24
static_17	Frag4	57	66
static_18	Frag4	58	21
static_19	Frag4	55	-24
static_20	81mm	70	66
static_21	81mm	75	21
static_22	81mm	75	-24
static_23	105mm	60	66
static_24	105mm	75	21
static_25	105mm	70	-24
static_26	155mm	75	66

static_27	155mm	75	21
static_28	155mm	70	-24
static_29	60mm	40	66
static_30	60mm	35	21
static_31	60mm	40	-24
static_32	37mm	40	66
static_33	37mm	35	21
static_34	37mm	35	-24
static_35	Frag3	35	66
static_36	Frag3	40	21
static_37	Frag3	35	-24
static_38	Frag2	40	66
static_39	Frag2	40	21
static_40	Frag2	42	-24
static_41	Frag1	40	66
static_42	Frag1	40	21
static_44	Frag1	20	66
static_45	Frag1	20	21
static_46	Frag1	20	-24
static_47	Frag2	20	66
static_48	Frag2	20	21
static_49	Frag2	20	-24
static_50	Frag3	23	66
static_51	Frag3	23	21
static_52	Frag3	23	-24
static_53	37mm	23	66

8.5.3. Dynamic Measurements

The base station is configured so that it records all the information needed to make atmospheric corrections during the survey. On the rover, we store the raw GPS and IMU data, not just the estimated positions as we would when running in real-time mode. We use the Novatel SPAN to get position accuracies on the order of 1 cm and orientations to better than 0.25 degrees. We use post-processing to get the best accuracy. See Table 8.3 for a summary of targets and measurements.

Table 8.3: UXO and scrap orientations and depths for dynamic platform data measurements. The first measure, dynamic_1, provides the background response to be removed.

XYZ file	target	depth	dip (down +ve)
dynamic_1	37mm	0	66
dynamic_2	37mm	0	-24
dynamic_3	37mm	0	21
dynamic_4	frag1	0	21
dynamic_5	frag1	0	66
dynamic_6	frag1	0	-24
dynamic_7	frag2	0	-24
dynamic_8	frag2	0	66
dynamic_9	frag2	0	21
dynamic_10	frag3	0	21
dynamic_11	frag3	0	66
dynamic_12	frag3	0	-24
dynamic_13	60mm	0	-24
dynamic_14	60mm	0	66
dynamic_15	60mm	0	21
dynamic_16	37 mm	10	66
dynamic_17	37 mm	13	21
dynamic_18	60 mm	10	66
dynamic_19	60 mm	10	21
dynamic_20	Frag 1	13	66
dynamic_21	Frag 1	13	21
dynamic_23	Frag 2	13	66
dynamic_24	Frag 2	13	21
dynamic_25	Frag 3	13	66
dynamic_26	Frag 3	13	21
dynamic_27	81 mm	35	66
dynamic_28	81 mm	35	21
dynamic_29	Frag 4	35	66
dynamic_30	Frag 4	35	21
dynamic_32	Frag 5	35	66
dynamic_33	Frag 5	35	21
dynamic_35	Frag 1	13	-24
dynamic_36	Frag 2	13	-24
dynamic_37	Frag 3	13	-24
dynamic_38	Frag 4	33	-24
dynamic_39	Frag 5	33	-24
dynamic_40	37 mm	13	-24

dynamic_41	60 mm	13	-24
dynamic_42	81 mm	17	-24
dynamic_43	155 mm	55	66
dynamic_44	155 mm	60	21
dynamic_45	155 mm	60	-24
dynamic_46	155 mm	40	66
dynamic_47	155 mm	40	21
dynamic_48	155 mm	40	-24
dynamic_49	105 mm	25	66
dynamic_52	105 mm	50	66
dynamic_53	105 mm	45	21
dynamic_54	105 mm	50	-24
dynamic_55	81 mm	45	66
dynamic_56	81 mm	45	21
dynamic_57	81 mm	45	-24

8.6.4. Inversion/Discrimination Results from Real Magnetic Data

We turn our attention here to demonstrating the inversion/discrimination algorithms developed and successfully applied for synthetic UXO/scrap models, to the first case of real data from the static experiments (sections 8.6.1. and 8.6.2.). These are the higher quality data of the two experiments. We seek to recover the position, dipole and quadrupole moments, as well as the resulting asymmetry parameters (eq. 8.5.) calculated from the higher-order moments for discrimination based on knowledge of shape from magnetics. For brevity, we limit the inversion results to two of the data sets for the static case, one over UXO and one over scrap.

The first target and data are presented in Figure 8.7. The 60mm UXO source is presented in panel (a), the original test-stand data are illustrated in panel (b), the background response removed prior to inversion is illustrated in panel (c), and the final data for inversion analysis is illustrated in panel (d). We invert the data in panel (d) using Quenched Simulated Annealing to recover the position, higher-order moments and asymmetry parameter (eq. 8.5.). The predicted data are provided in Figure 8.7 panel (e), and the data-difference in panel (f).

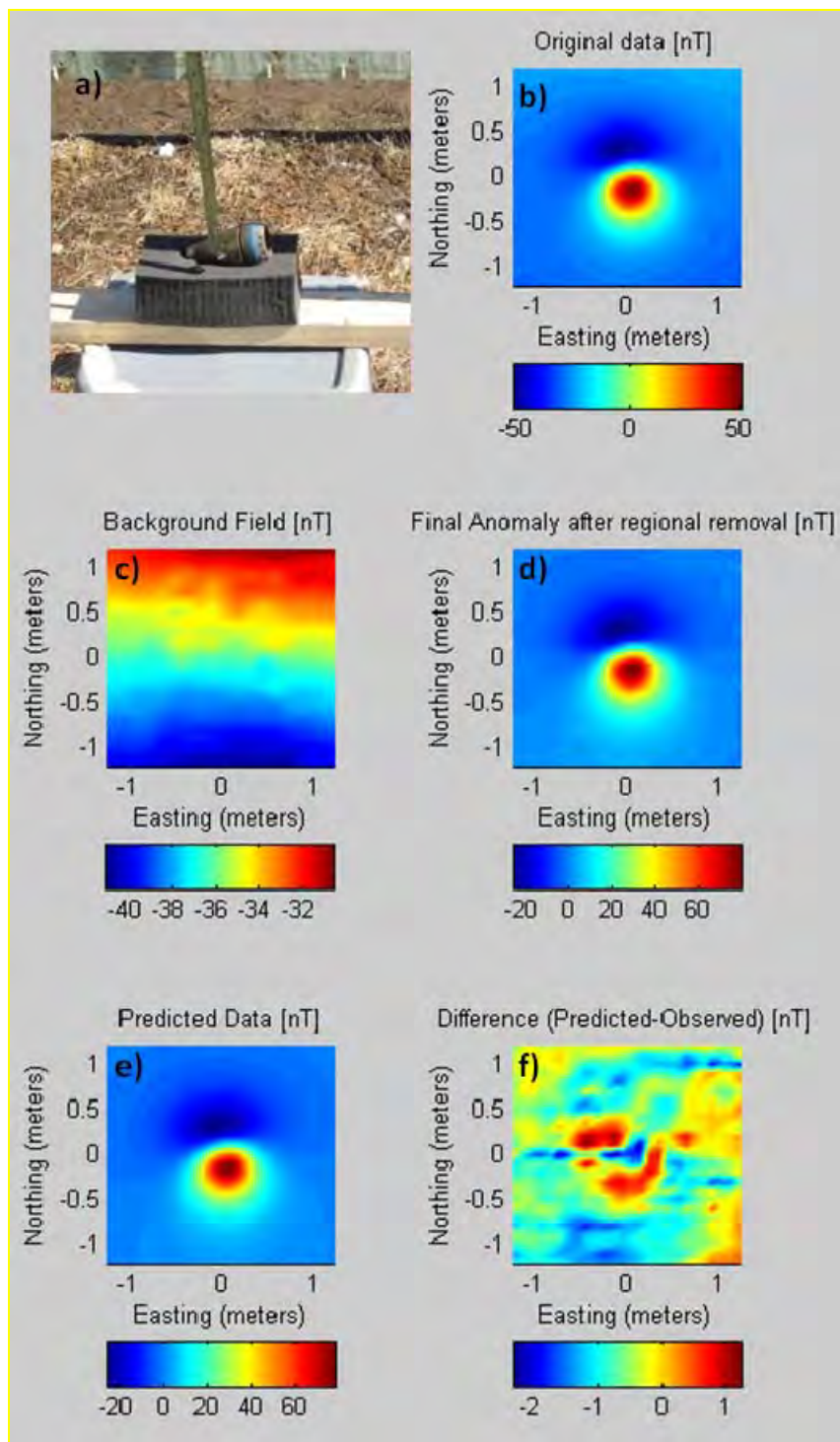


Figure 8.7: Static experiment, Target ‘Static_29’ from Table 8.2 representing 60mm UXO. (a) photo of the target; (b) original magnetic response from static experiment; (c) regional field beneath target for removal; (d) final magnetic anomaly for inversion to recover multipole moments; (e) predicted data from inversion model; (f) data difference.

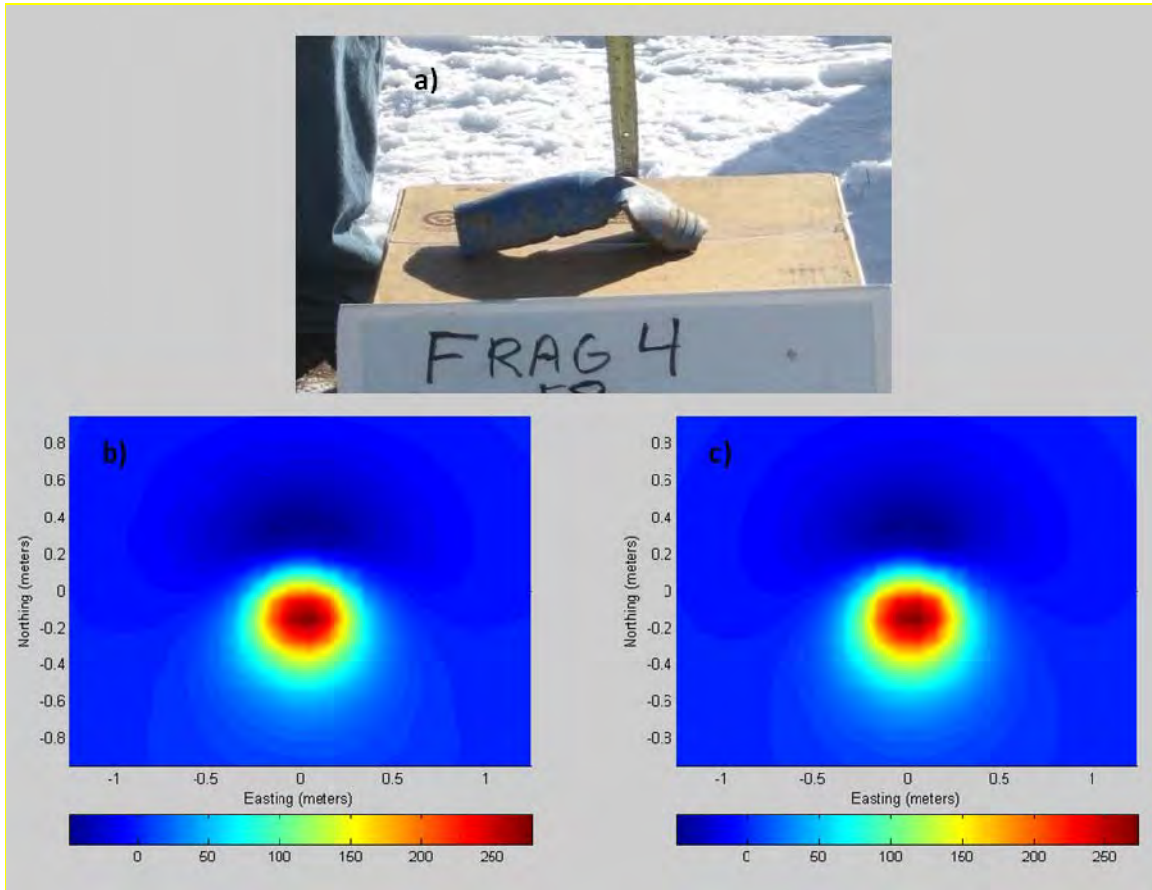


Figure 8.8: Static experiment, Target ‘Static_14’ from Table 8.2 representing Fragment 4. (a) photo of the target; (b) magnetic anomaly for inversion to recover multipole moments (background response removed); (e) predicted data from inversion model.

The second target and associated data are presented in Figure 8.8. The metal scrap source is presented in panel (a), the final data for inversion analysis is illustrated in panel (b). We again invert the data for the scrap target in panel (b) using Quenched Simulated Annealing to recover the position, higher-order moments and asymmetry parameter. The predicted data are provided in panel (c) and we have a good comparison with the true response, visually and statistically.

Table 8.4: Inversion results & asymmetry parameters recovered for the two UXO and scrap items from static test-stand data (Static_29 and Static_14, respectively).

60 mm	Asym .Par	x (m)	y (m)	z (m)	Mx	My	Mz	Pxx	Pxy	Pxz	Pyy	Pyz
Rec	0.7	-0.003	0.02	0.00 3	0.0168	0.003	0.05	-0.002	0.0001	0.0015	-0.0043	-7e-4
Scrap	Asym .Par	x (m)	y (m)	z (m)	Mx	My	Mz	Pxx	Pyy	Pxz	Pyy	Pyz
Rec	0.72	0.0318	0.034	0.07	0.04	0.003	0.12	-0.005	-0.004	-0.019	-0.0014	-0.0073

Table 8.4 provides a summary of the total recovered parameters through inversion by QSA for the real 60mm and fragment targets in Figures 8.7 and 8.8. We note in Figure 8.7(f) that the data difference is dominated by alternating horizontal bands of highs and lows on the order of 1-2 nT. These low amplitude coherent features are subtle ‘heading errors’ contained within the data from sensor paths, generally present in most magnetic data, whether observed or not by the eye. The inversion has appropriately ignored these features and the resulting data fit indicates successful parameter recovery.

The results from inversion and associated asymmetry parameters for the remaining UXO and scrap targets, listed in Table 8.2, are consistent and we therefore summarize here with these two examples. The asymmetry parameter for the various real UXO and scrap targets, with varying orientations and depth, are calculated with minimal variation for the static platform experiments, regardless of the items’ true level of symmetry. This indicates that the higher-order magnetic moments are not adequately captured within the test stand data, and the measured response is therefore dominated by the magnetic dipole. As a result, we are not able to effectively extract meaningful shape information based on multipole moments.

Inversion results for the test-stand data indicate that, while the method of recovering higher-order moments is theoretically sound for discrimination based on magnetic data – as demonstrated with synthetic modeling, it is not practical for real UXO discrimination application. Quenched Simulated Annealing inversion successfully recovered position,

dipole and quadrupole moment parameters from the test-stand data within expected data-fit. However, based on the similarity of the resulting asymmetry parameters between UXO and scrap, it is apparent that even high-quality test-stand magnetic data do not contain enough information within the higher-order moments to extract diagnostic information for discrimination based on shape/symmetry.

Given that it is not possible to recover shape information from the static test-stand data, the higher-quality of the two experiments, it is not meaningful to move forward to data from the dynamic platform for the same goal. The conclusion will remain the same: higher-order magnetic moments can not be recovered from total-field data, in practice, to the extent that we may discrimination between UXO and scrap based on shape/symmetry.

8.7. Summary

It is well known that meaningful information on a target's asymmetric distribution of magnetization is not contained in the magnetic dipole moment. This shape information is only contained in the higher-order moments. Currently, however, the dipole moment, which dominates the response of isolated metallic sources is the only moment utilized in attempts to discriminate between UXO and scrap in remediation efforts. To advance magnetics beyond detection and into a meaningful tool for discrimination based on shape/symmetry, recovery of the higher order moments would be necessary.

One of greatest challenges of recovering the moments, as observed over this project, is in navigating through the complex structure of the objective function for the associated inverse problem. We have implemented four separate optimization algorithms for this problem, which range from guided local search, to random local search, to global optimization approaches, and into the hybrid optimization algorithms. We have identified that a recursive Quenched Simulated Annealing (QSA) produces reliable information on the complex nature of the solution space, as well as recovers, at the least, a near optimal solution associated with global minimum and a good representation of target parameters. The method has performed well for realistic synthetic models created

to simulated various UXO and scrap models. Therefore, we developed a robust methodology for recovering a direct measure of target asymmetry as a foundation for advancing magnetics into discrimination based on shape information in the higher-order moments.

In contrast to synthetic modeling, we identified in the last year of MR-1638, the same level of positive result is not observable in practice. We have developed and applied one of the most robust inversion algorithms to the highest quality magnetic data acquired for UXO/scrap analysis. The requisite shape information contained within the higher-order moments, as calculated from the asymmetry parameter (eq. 8.5.), may not be extracted in practice from total-field magnetic data, as it can be from simulation.

9. Discussion

The research for this project progressed as planned over the life of MR-1638, and we have accomplished the major goals outline in the project plan.

9.1. Automated Anomaly Detection by Extended Euler Deconvolution

The first major accomplishment was further development and understanding of the automatic anomaly detection algorithm based on extended Euler deconvolution, which consisted of the basic algorithm, pre-processing methods, expansion to gradient data, and post-processing amplitude analysis for reducing false targets. With the detection algorithm in place, we spent significant time understanding the effects of pre-processing procedures on structural index of UXOs. We have also applied the detection algorithm to a series of large field datasets, including Camp Sibert and San Luis Obispo. Results have demonstrated the approach is a viable alternative for automatic detection of potential UXO using magnetic data.

9.2. Separation of Interfering Geology, Enhancing UXO Response

A second major success of the project, although not predicted to be such a large component of MR-1638 originally, was the advancements made towards significantly improving data quality in difficult magnetic data sets. The project was initially developed to address the needs for magnetic detection and discrimination in strongly interfering magnetic environments. The work on separating the response of strong background interference and enhancing those of UXO and scrap had required designing, assembling or modifying many robust algorithms developed, in part, through this project (such as linear feature analysis and F-K Filter), also through past SERDP projects (ex: MM-1414: wavelet filter, iterative Wiener filter), as well as with advances in the larger exploration communities, such as in the mining and petroleum industries. MR-1638 research and application has successfully demonstrated that even the most difficult magnetic datasets can be significantly enhanced at the early stages of processing, prior to

subsequent detection and discrimination analysis should be attempted. We have shown that the compact, high-amplitude magnetic lineaments generating many of the false positives in Camp Sibert magnetics, for example, can be separated while preserving the response of UXO and scrap. We have likewise shown that the most difficult magnetic regions for detection in the San Luis Obispo (SLO) data can also be greatly enhanced. The separated and enhanced dipole-anomalies of UXO and scrap at SLO can significantly improve the chances of detecting these sought targets, regardless of one's preference of detection algorithm.

9.3. Recovering higher-order moments for magnetic discrimination

Finally, we have developed a series of optimization algorithms for recovering the higher order magnetic moments from potential UXO targets. The multipole moments contain within them the necessary information on target shape to allow for successful discrimination based on magnetic method. The first difficulty was extraction of the higher-order moments, which are generally very small relative to the dominant dipole response observed in magnetic UXO data. The many optimization algorithms developed over this project were designed to specifically address the complexity of the inverse solution space for this problem. We identified that the problem contains a multi-modal objective function, and that the traditional down-hill search algorithms guided by derivative information may not prove valuable as originally predicted. In response, we developed a total of four search algorithms including Gauss-Newton, Genetic Algorithm (GA), recursive Quenched Simulated Annealing (QSA), and a Memetic Algorithm (MA). Over the last research year, QSA was identified as our tool of choice and it clearly identified the multi-modal nature of the solution space as well as clearly identified the global minimum. As a result, we successfully recovered the multipole moments for realistic UXO and scrap targets, and through the associated Asymmetry Parameter, we proved it was theoretically possible to discriminate between UXO and scrap with high-quality data and a robust optimization algorithm. The methods were successfully applied to realistic 3D models of both UXO and scrap.

In contrast, we identified in the last year of MR-1638 that the same level of positive result is not observable in practice. We have developed and applied one of the most robust inversion algorithms to the highest quality magnetic data acquired for UXO/scrap analysis. The requisite shape information contained within the higher-order moments may not be extracted in practice from total-field magnetic data, as it can be from simulation.

10. Acknowledgements

We would like to thank SERDP for the funding support, and Anne Andrews, Herbert Nelson, Jay Bennett, Katherine Kaye, Peter Knowles, Badrieh Sheibeh and Daniel Ruedy for their consistent support throughout the project. We thank Don Yule for his conversations and support related to UXO detection. We also thank Len Pasion and Todd Meglich for helpful discussions on the Camp Sibert data set. Finally, we thank Kris Davis from Colorado School of Mines for his valuable additions to extended Euler deconvolution.

11. References

- Abragam, A., 1961, The principles of nuclear magnetism. Oxford University Press, London. Pg. 232.
- Altshuler, T., 1996, Shape and orientation effects on magnetic signature prediction for unexploded ordnance: Proc. UXO Forum, 282-291.
- Billings, S.D., 2004, Discrimination and classification of buried unexploded ordinance using magnetometry: IEEE Transactions of Geoscience and Remote Sensing, **42**, 1241-1251
- Billings, S. D., and F. Herrmann, 2003, Automatic detection of position and depth of potential UXO using a continuous wavelet transform: Conference proceedings, 1012–1022, SPIE.
- Billings, S. D., L. R. Pasion, and D. W. Oldenburg, 2002, UXO discrimination and identification using magnetometry: Presented at the Symposium of Applied Geophysics to Engineering and Environmental Problems (SAGEEP), Las Vegas, NV.
- Blakely, R.J., 1996, Potential theory in gravity & magnetic applications: Cambridge University Press.
- Bracken, Robert E., Brown, Philip J., 2005, Reducing tensor magnetic gradiometer data for unexploded ordnance detection. U.S. Geological Survey Scientific Investigations Report SIR 2005-5046.
- Butler, D. K., Cespedes, E. R., Cox, C. B., Wolfe, P. J., 1998, Multisensor methods for buried unexploded ordnance detection, discrimination and identification. Technical Report 98-10, SERDP, September 1998.
- Davis, K., Li, Y., and M. Nabighian, 2005, Automatic detection of UXO magnetic anomalies using extended Euler deconvolution: SEG Extended Abstracts, **24**, 1133-1136.
- Gradshteyn, I.S., and I.W. Ryzhik, 1965, Table of integrals series and products: Academic Press.

- Hansen, R., and E. deRidder, 2006, Linear feature analysis for aeromagnetic data: *Geophysics*: **71**, L61-L67.
- Hood, P., 1965, Gradient measurements in aeromagnetic surveying: *Geophysics*, 30, 891–902.
- Jackson, J., 1999, Classical Electrodynamics, Third Edition: John Wiley and Sons.
- Krahenbuhl, R., Li, Y., Nabighian, M., and Billings, S., 2009, SERDP MM-1638 2009 Annual Report.
- Lanczos, C., 1988, Applied analysis: Courier Dover Publications.
- Li, Y., Krahenbuhl, R., Meglich, T., Pasion, L., Walker, S., Oldenburg, D., Billings, S., van Dam, R., and B. Harrison, 2007, SERDP MM-1414 2007 Annual Report.
- Lyrio, J., Tenorio, L., and Y. Li, 2004, Efficient automatic denoising of gravity gradiometry data: *Geophysics*, v. 69, p. 772-782
- McFee, J. E., 1989, Electromagnetic Remote Sensing: Low Frequency Electromagnetics. DRES Special Publication SSP 124. Defence Research Establishment Suffield Ralston, Alberta.
- McFee, J. E. and Das, Y., 1990, A multipole expansion model for compact ferrous object detection: Proceedings ANTEM Symposium on Antenna Technology and Applied Electromagnetics, Manitoba, Canada, 633-638.
- Mushayandebvu, M. F., P. van Driel, A. B. Reid, and J. D. Fairhead, 1999, Magnetic imaging using extended euler deconvolution: Expanded Abstracts, 400–403, Soc. Expl. Geophys. Intern. Mtg.
- Nabighian, M. N., 1972, The analytic signal of two dimensional magnetic bodies with polygonal cross-section: Its properties and use for automated anomaly interpretation: *Geophysics*, 37, 507–517.
- , 1984, Toward a three-dimensional automatic interpretation of potential field data via generalized hilbert transforms: Fundamental relations: *Geophysics*, 49, 780–786.

Nabighian, M. N., and R. O. Hansen, 2001, Unification of Euler and Werner deconvolution in three dimensions via the generalized Hilbert transform: *Geophysics*, 66, 1805–1810.

Nova Research Inc., 2007, Environmental Security Technology Certification Program (ESTCP) technology demonstration data report. ESTCP UXO Discrimination Study. MTADS demonstration at Camp Sibert magnetometer/ EM61 MkII/ GEM-3 arrays. ESTCP Project MM-0533.

Pedersen, L. B., 1978, Wavenumber domain expressions for potential fields from arbitrary 2-, 2 1/2, and 3-dimensional bodies: *Geophysics*, 43, 626–630.

Reid, A. B., J. M. Allsop, H. Granser, A. J. Millett, and I. W. Somerton, 1990, Magnetic interpretation in three dimensions using euler deconvolution: *Geophysics*, 55, 80–91.

Sanchez, V., Li, Y., Nabighian, M., and D. Wright, 2006, Relative importance of magnetic moments in UXO clearance applications: *SEG Expanded Abstracts*, 25, 1381.

Shearer, S., 2005, Three-dimensional inversion of magnetic data in the presence of remanent magnetization: Master's thesis, Colorado School of Mines.

Sinex, D., 2006, Advancing the state of the art of UXO discrimination for total-field magnetic data: M.S. Thesis, Colorado School of Mines.

Sinex, D., Y. Li, and D. Yule, 2005, Improving UXO discrimination using magnetic quadrupole moments: *Expanded Abstracts*, 680–683, Soc. Expl. Geophys. Intern. Mtg.

Wiener, N., 1949, Extrapolation, interpolation, and smoothing of stationary time series: Cambridge, MIT